

EXPLOITING DEVICE NONLINEARITY IN ANALOG CIRCUIT DESIGN

A Dissertation
Presented to

Dr. Paul Hasler
School of Electrical and Computer Engineering
Georgia Institute of Technology, Atlanta, GA 30332

By

Kofi Odame

In Partial Fulfillment
of the Requirements for the Degree
Doctor of Philosophy in Electrical Engineering

School of Electrical and Computer Engineering
Georgia Institute of Technology
August 2008

Copyright 2008 by Kofi Odame

EXPLOITING DEVICE NONLINEARITY IN ANALOG CIRCUIT DESIGN

Approved by:

Dr. Paul E. Hasler, Advisor
Assoc. Professor, School of ECE
Georgia Institute of Technology

Dr. Bradley A. Minch
Assoc. Professor of ECE
Franklin W. Olin College of Engineering

Dr. David V. Anderson
Assoc. Professor, School of ECE
Georgia Institute of Technology

Dr. David G. Taylor
Professor, School of ECE
Georgia Institute of Technology

Dr. Robert J. Butera
Assoc. Professor, School of ECE
Georgia Institute of Technology

Date Approved: July 6, 2008

DEDICATION

This work is dedicated to Yaa, who, along with Yaw, never fails to remind me of what is truly important in life.

ACKNOWLEDGMENTS

I am very grateful for the guidance given to me by my advisor, Prof. Hasler and by my de facto co-advisor Prof. Anderson. Prof. Minch has long been an inspiration, and I will always strive to achieve his level of excellence as a teacher and as an engineer. Sincere thanks to Profs. Butera and Taylor for serving on my dissertation committee and for their helpful comments and suggestions.

I would like to acknowledge the entire CADSP family for welcoming me into the Georgia Tech community and for their help and camaraderie in the past four years. Special thanks to Dr. Peng, aka Thomas, for his insightful nuggets of wisdom about circuits, engineering and life in general.

Lastly, I would like to thank my family (Papa, Mama, Angela, Kwasi, Kofi, Cordelia, Urvashi, Master Li, Naïm, the whole Kotoku clan as well as the entire Ama-Ofeibea *abusua*) for their limitless support and unshakeable belief in me.

6.2	Motivation for using OTA as an amplitude limiter	57
6.3	OTA-C oscillator synthesis	64
6.4	Characteristics of the van der Pol equation	70
6.5	OTA-C oscillator analysis and design considerations	72
6.6	An illustrative example	74
6.7	Low distortion sinusoidal oscillators	84
CHAPTER 7 A BANDPASS FILTER WITH INHERENT GAIN ADAP-		
TATION FOR HEARING APPLICATIONS		90
7.1	Implications for speech perception	91
7.2	Filter description and architecture	94
7.3	Amplifier implementations	107
7.4	Circuit analysis	112
7.5	Circuit implementation and experimental results	119
7.6	Discussion of results	125
CHAPTER 8 CONCLUSION		128
8.1	Main contributions	128
8.1.1	Nonlinear dynamics in integrated circuits	129
8.1.2	Design of OTA-C sinusoidal oscillators with OTA nonlinearity	130
8.1.3	Design of a bandpass filter for auditory signal processing . .	130
8.1.4	Studying integrated circuit dynamics on a reconfigurable plat-	
	form	131
REFERENCES		132

LIST OF TABLES

Table 1	Comparison of filter performance to other work	127
---------	--	-----

LIST OF FIGURES

Figure 1	Processing chain of a typical cochlear implant.	2
Figure 2	Field programmable analog array.	5
Figure 3	Simple current mirror	9
Figure 4	Vector field of the logistic equation	11
Figure 5	Simple peak detector	12
Figure 6	Circuit that is prone to supercritical pitchfork bifurcation.	16
Figure 7	Progression of supercritical pitchfork bifurcation.	17
Figure 8	Supercritical pitchfork bifurcation	18
Figure 9	Circuit that is prone to subcritical pitchfork bifurcation.	19
Figure 10	Progression of subcritical pitchfork bifurcation.	20
Figure 11	Subcritical pitchfork bifurcation	21
Figure 12	Second order section	24
Figure 13	Phase plane portrait	26
Figure 14	Sketch of the SOS phase plane for large signals	29
Figure 15	Experimental SOS's phase plane plots for various values of r	30
Figure 16	Experimental SOS's step responses for various values of r	31
Figure 17	General block diagram form of a first-order circuit.	35
Figure 18	Magnitude-frequency plots of the third harmonic.	39
Figure 19	Source follower amplifier	40
Figure 20	Magnitude-frequency response of source follower.	42
Figure 21	Unity gain buffer	43
Figure 22	Magnitude-frequency response of unity-gain buffer.	44
Figure 23	Second order section for singular perturbation analysis.	46
Figure 24	Generic OTA	55
Figure 25	Linear OTA transfer curve	58

Figure 26	Region of oscillation	59
Figure 27	OTA implementation of negative resistance.	60
Figure 28	Generic OTA-C SOS	65
Figure 29	Simple van der Pol derivation.	66
Figure 30	Inputs to the nonlinear OTA	74
Figure 31	Lyon/Mead SOS.	75
Figure 32	Oscillator derived from Lyon/Mead SOS	77
Figure 33	DeWeerth OTA.	78
Figure 34	Oscillator die micrograph	79
Figure 35	Oscillation frequency control.	80
Figure 36	Oscillation amplitude control.	81
Figure 37	THD dependence on G_h	82
Figure 38	Oscillator output	83
Figure 39	Phase plane portrait for the low distortion oscillator given by (203).	85
Figure 40	Amplitude control of low distortion oscillator.	87
Figure 41	Multichannel compression hearing aid	91
Figure 42	Simulation results for a single band of speech processing	93
Figure 43	Basilar membrane measurements	95
Figure 44	Desired frequency response and step response of nonlinear filter.	97
Figure 45	Phase plane portrait for potential cochlear model.	99
Figure 46	Step response for potential cochlear model, with pwl nonlinearity.	100
Figure 47	Step response for potential cochlear model, with continuously-differentiable nonlinearity.	101
Figure 48	Frequency response for potential cochlear model, with continuously-differentiable nonlinearity.	102
Figure 49	Phase portrait for step response of system of (233)	103
Figure 50	Supercritical Hopf bifurcation in nonlinear bandpass filter	105

Figure 51	Bandpass filter with adaptive quality factor.	108
Figure 52	Highly linear OTA	110
Figure 53	Nonlinear amplifier	111
Figure 54	Theoretical knee control	114
Figure 55	Schematic for analyzing noise in filter	115
Figure 56	Input dynamic range, power tradeoff	118
Figure 57	Die photograph of the bandpass filter	120
Figure 58	Center frequency control	121
Figure 59	Quality factor adaptation	122
Figure 60	Threshold knee point control	123
Figure 61	THD reduction with offset removal	124
Figure 62	Noise power spectrum	125
Figure 63	Filter response to input bursts	126

SUMMARY

This dissertation presents analog circuit analysis and design from a nonlinear dynamics perspective.

An introduction to fundamental concepts of nonlinear dynamical systems theory is given. The procedure of nondimensionalization is used in order to derive the state-space representation of circuits. Geometric tools are used to analyze nonlinear phenomena in circuits, and also to develop intuition about how to evoke certain desired behavior in the circuits. To predict and quantify non-ideal behavior, bifurcation analysis, stability analysis and perturbation methods are applied to the circuits. Experimental results from a reconfigurable analog integrated circuit chip are presented to illustrate the nonlinear dynamical systems theory concepts.

Tools from nonlinear dynamical systems theory are used to develop a systematic method for designing a particular class of integrated circuit sinusoidal oscillators. This class of sinusoidal oscillators is power- and area-efficient, as it uses the inherent nonlinearity of circuit components to limit the oscillators' output signal amplitude. The novel design method that is presented is based on nonlinear systems analysis, which results in high-spectral purity oscillators. This design methodology is useful for applications that require integrated sinusoidal oscillators that have oscillation frequencies in the mid- to high- MHz range.

A second circuit design example is presented, namely a bandpass filter for front-end auditory processing. The bandpass filter mimics the nonlinear gain compression that the healthy cochlea performs on input sounds. The cochlea's gain compression is analyzed from a nonlinear dynamics perspective and the theoretical characteristics of the dynamical system that would yield such behavior are identified. The appropriate circuit for achieving the desired nonlinear characteristics are designed, and it is incorporated into a bandpass filter. The resulting nonlinear bandpass filter performs

the gain compression as desired, while minimizing the amount of harmonic distortion. It is a practical component of an advanced auditory processor.

CHAPTER 1

INTRODUCTION

The vision of making ubiquitous small, battery- or self-powered electronic sensors is becoming more practical, thanks to advances in MEMS and integrated circuit technology, as well as to improvements in wireless communication [1]. MEMS and integrated circuit technology are yielding smaller and more sensitive sensors. Advanced wireless communication protocols are resulting in robust and self-healing communication links among sensors and between sensors and remote processing units. Two areas where the availability of small, reliable sensors are likely to make a strong impact are environmental monitoring and health care.

Environmental sensor networks track and analyze images, temperature and other environmental indicators. Other than augmenting geoscientific study, the purpose of these sensor networks is to monitor and predict natural hazards as well as to monitor climate change in otherwise inaccessible locations [2].

In the field of health care, implantable and wearable electronics perform health monitoring, treatment and neural prosthetic functions. As a result, health care can become decentralized yet affordable, thus giving patients a less-hindered lifestyle and greater personal freedom [3].

One technical challenge of sensor applications, be they implanted in the human body or deployed in a remote location, is that they must be energy efficient. Effective strategies for energy efficiency involve reducing the amount of irrelevant data that is converted, transmitted or processed.

Take for instance the sensor application depicted in Fig. 1. It is a block diagram of the sensing and processing chain of a typical cochlear implant. At the front end, a microphone senses over 90dB dynamic range of audio input. This analog signal is digitized by a 16-bit analog-to-digital converter (ADC). The digital data are then

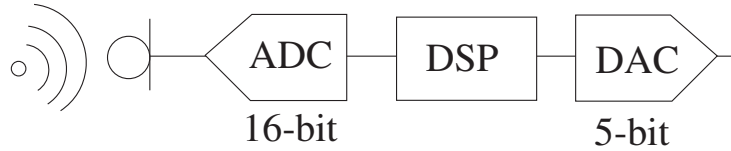


Figure 1. Processing chain of a typical cochlear implant. This audio signal is digitized by a 16-bit analog-to-digital converter (ADC). The digital data are then transmitted to a digital signal processor, which extracts and encodes pertinent information from the data. The encoded information is transmitted as 5-bit electrical pulses to the patient’s auditory nerve.

transmitted to a digital signal processor, which extracts and encodes pertinent information from the data. The encoded information is transmitted as electrical pulses to the patient’s auditory nerve, eliciting a “hearing” sensation.

With current designs, a cochlear implant would completely discharge a 100mAh battery in about 20 hours. To improve the energy efficiency of the signal processing, we must take a critical look at information flow in the cochlear implant. Notice that, even though 16 bits of sound data are captured, only 5 bits of information eventually make it to the patient’s auditory nerve. In general, every extra bit of resolution of an ADC corresponds to a four-fold increase in the ADC’s power consumption [4]. As such, significant power savings will occur if, instead of converting raw and largely redundant data from analog to digital, the ADC performed some feature extraction to preclude the need for 16-bit precision. Other benefits of conducting such information-refinement at the head of the processing chain are that irrelevant information is not transmitted, and that the bit precision and processing requirements of the digital signal processor can be relaxed. These benefits, too, lead to energy efficiency. The idea of performing some form of intelligent “analog-to-information” conversion at the front end is not applicable only to cochlear implants, but is beneficial in a wide variety of other sensor applications [5].

Almost all forms of feature extraction or information refinement require some sort

of nonlinear processing. Since we are interested in performing the feature extraction on real world — as opposed to digital — signals, the question arises of how to implement nonlinear signal processing in analog integrated circuitry.

There are two possible implementation strategies. In one approach, the nonlinear processing algorithm has a well-defined analytical representation. In this situation, the task is to find an appropriate circuit implementation of a set of mathematical equations. For instance, if the algorithm called for a log/anti-log operation, this could be achieved by considering the base-emitter voltage of a bipolar junction transistor (BJT) and its collector current. Such knowledge is widespread [6–8], and will not be the focus of this dissertation.

The other approach to analog nonlinear signal processing involves a processing function that needs to be implemented, but does not necessarily have a known analytical representation. This sort of problem is often encountered when we try to model or mimic signal processing functions that are found in nature. Instead of creating an empirically-based analytical representation that is then approximated by a circuit, consider the following alternative approach. We can characterize the processing function in nonlinear dynamical system terms. For example, does it have a limit cycle? Does it display hysteresis, or multiple steady state behavior? Once the essential dynamics have been identified, we can then create a circuit that also displays these properties. How do we know which circuits would be appropriate for exhibiting a particular kind of dynamics? The idea is to perceive and understand circuits as dynamical systems themselves. To this end, this dissertation aims to introduce fundamental concepts and tools of dynamical systems theory from an analog IC perspective. For example, what sort of circuit would undergo a Hopf bifurcation? What would be the implication of a Hopf bifurcation to the circuit's performance and behavior?

1.1 Reconfigurable analog integrated circuits

To develop a thorough and intuitive appreciation of the nonlinear dynamics of analog circuits, one has to study and experiment with a great number of them.

Computer tools for circuit simulation are one way to readily access a large variety of circuits. Unfortunately, these computer tools are prone to the problems of numerical integration, such as accumulation of round-off error and stiffness. Also, current circuit simulation tools are mostly optimized for engineering linear systems; they are unwieldy when the design involves deliberate use of system nonlinearities. Finally, the models of integrated circuit devices that are used for simulation do not always capture the full range of nonlinear behavior. For instance, the output impedance of a MOS transistor is often poorly modelled, for the sake of fast convergence of the simulation.

The shortcomings of computer simulation can be avoided by experimenting on actual, physical integrated circuit chips. The expense and time involved in fabricating an integrated circuit chip suggests that this approach would greatly limit the variety of circuits that one might have access to. Fortunately, we have available to us a reconfigurable analog chip that contains over 50,000 circuit elements that can be connected and rewired with each other to form a vast number of different circuits. This reconfigurable chip allows the designer to flexibly explore nonlinear circuit phenomena and to easily prototype systems with them. Much of the experimental data in this dissertation was measured from such a reconfigurable chip.

1.1.1 Architecture of reconfigurable analog integrated circuit

The reconfigurable chip that was used for experimental data is a field programmable analog array (FPAA) that is based on floating-gate technology [9]. It contains 32 configurable analog blocks (CABs), which are connected via a three-level routing network. The routing network is made from floating-gate transistors, which act as compact, analog computational memory elements. Together with the CABs, the floating gates

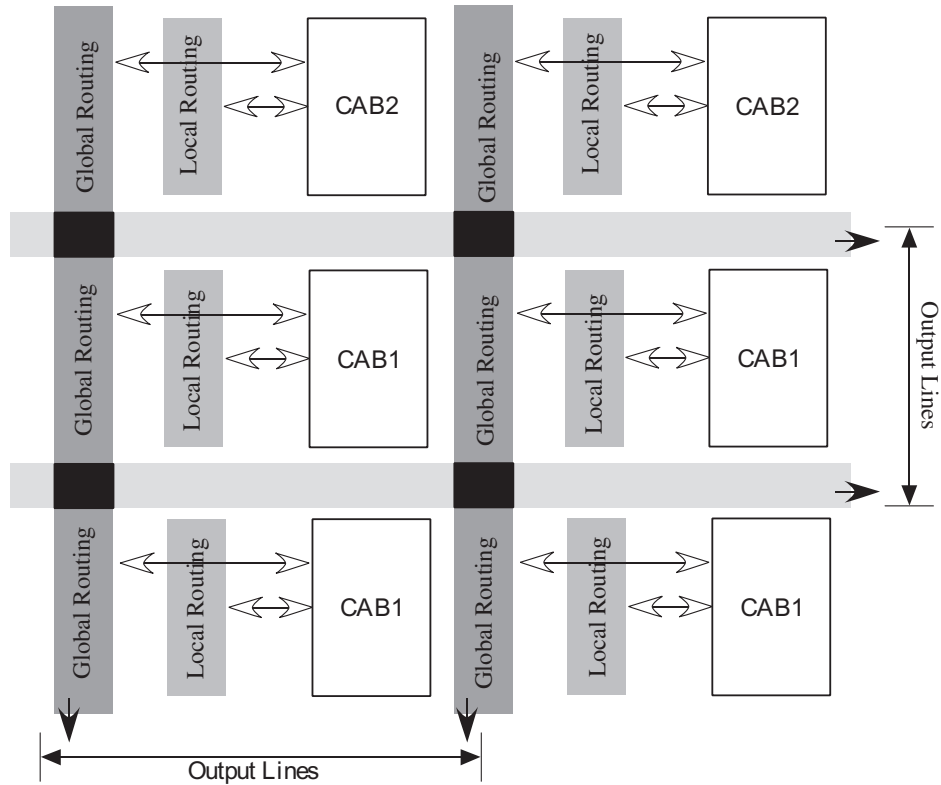


Figure 2. Field programmable analog array (FPAA). The FPAA consists of several configurable analog blocks (CABS), each of which contains a number of analog circuits, and a three-level routing network that allows the components of the CABs to be connected to each other.

in the routing network provide over 50,000 programmable analog elements.

The FPAA contains two types of CABs. The components in the first type of CAB include three operational transconductance amplifiers (OTAs), a voltage buffer, three floating 500 fF capacitors, and n- and p-type MOS transistor arrays with two common terminals for easily constructing source-follower or current-mirror topologies. Each OTA is electronically tunable, via a floating-gate bias current generator. There are two wide-linear-range, low-input-offset OTAs per CAB. The components in the second type of the CAB include two wide-linear-range folded Gilbert multipliers, a wide-linear-range OTA, and a programmable current mirror.

1.2 Teaching dynamics of integrated circuits

Based on the prevalent theory and design practice, most circuit design avoids nonlinearities as much as possible. The research presented in this dissertation challenges this view and seeks to understand circuit nonlinearities rigorously and intuitively enough to design with them. Thus, the results described in this dissertation were compiled into a syllabus and taught as a senior-level Special Topics Course titled “Nonlinear Circuit Dynamics” at the Georgia Institute of Technology in the Fall Semester of 2007.

1.3 Overview of dissertation

The organization of this dissertation is as follows. The work is separated into a first half of theory and analysis and a second half of design procedure.

In the first half of the dissertation, general theory and analysis of homogeneous and nonhomogeneous circuits will be discussed. For both types of systems, the discussion will begin with simple first-order circuits and progress to second-order circuits. These chapters will introduce canonical first-order circuits, as well as dynamical systems tools such as step response analysis, phase plane analysis, bifurcation and perturbation theory.

In the second half of the dissertation, two design projects will be described at length, using tools that were introduced in the first half of the dissertation.

The first design project discusses the use of inherent circuit nonlinearity to build integrated circuit low-distortion sinusoidal oscillators. The current literature that concerns this problem will be discussed and the shortcomings of the approaches described therein will be highlighted. I will then describe a systematic method for designing a class of sinusoidal oscillators that addresses these shortcomings. The dynamical systems tools that are featured in this design method are the Poincaré-Bendixon theorem, phase plane analysis, and singular perturbation theory. The main

nonlinearity that is exploited is the sigmoidal transfer function of an OTA.

The second design project discusses a low-power nonlinear bandpass filter for use in auditory prostheses. A brief description of the primary signal processing function of hearing aids will be presented. The technical challenges faced by current hearing aids will be mentioned as motivation for designing a novel bandpass filter. The design of this bandpass filter relies on step response analysis, phase plane analysis, stability analysis and perturbation theory. The main nonlinearity that is exploited is the sinh-like transfer function of an output buffer.

A concluding chapter will summarize the contributions of the work that has been presented in this dissertation.

CHAPTER 2

HOMOGENEOUS SYSTEMS I: FIRST-ORDER CIRCUITS

This chapter will introduce some simple tools for analyzing circuits as dynamical systems. We will consider one-dimensional systems of the form

$$\dot{x} = f(x), \tag{1}$$

where x represents some physical quantity like voltage or current, and $f(x)$ is a nonlinear function [10].

The circuits that will be described in this chapter constitute, in a sense, a set of canonical first-order circuits. In this set is represented circuits that exhibit odd-order nonlinearities and circuits that exhibit even-order nonlinearities. Odd-order nonlinearity refers to a function whose Taylor series expansion is such that its first nonlinear term is odd-ordered. For example, an operational transconductance amplifier-capacitor circuit contains a tanh nonlinearity, while an output buffer contains a sinh nonlinearity. The first non-zero, higher-order term in the Taylor series expansions of either the tanh or the sinh functions is the cubic term. As such, an operational transconductance amplifier-capacitor circuit and an output buffer exhibit odd-order nonlinearity. A function whose first nonlinear term in its Taylor series expansion is even-ordered is referred to as an even-order nonlinearity. The exponential — encountered in a source follower — and the quadratic — encountered in a current mirror — functions are examples of even-order nonlinearities.

Another dichotomy that is represented in the set of circuits that will be described is that of expansive versus compressive nonlinearities. We define an expansive nonlinearity as a function whose derivative increases in magnitude with an increase in magnitude of its argument. Examples of such a function are the exponential and the sinh functions. The tanh is an example of a compressive nonlinearity, which is

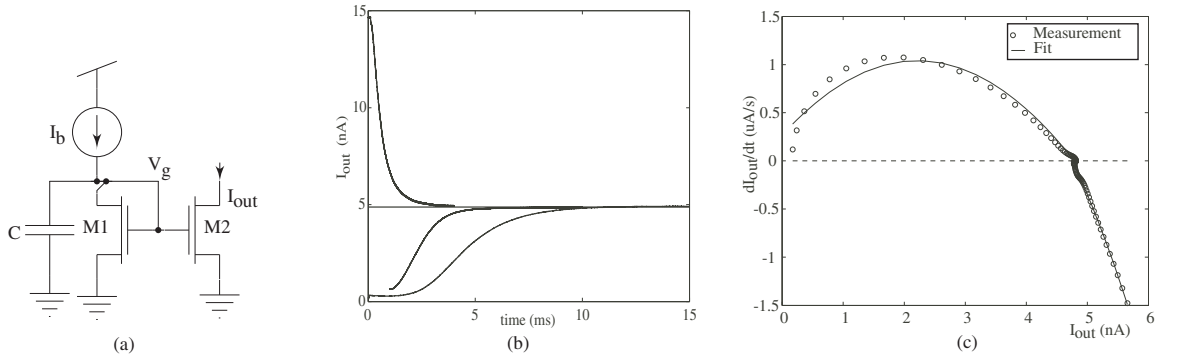


Figure 3. Simple current mirror. (a) Circuit that was compiled onto the FPAA. (b) Measured trajectories for different initial conditions. (c) Vector field derived from trajectory measurements. The origin is an unstable equilibrium point, while 5 is stable.

one whose derivative decreases in magnitude with an increase in magnitude of its argument. As we shall see, the physical constraints of the current mirror make its quadratic function fall into the category of compressive nonlinearity as well.

The discussions in this chapter, as well as that of Chapter 4, will include circuit analysis that explains how the various types of nonlinearities manifest in each of the circuits.

2.1 Geometric analysis

2.1.1 Simple current mirror

Consider the simple current mirror depicted in Fig. 3 (a). From Kirchhoff's Current Law (KCL), it obeys the following differential equation.

$$C \frac{dV_g}{dt} = I_b - f(V_g), \quad (2)$$

where $f(V_g)$ is the drain current of transistor M1. Assuming M1 and M2 are identical and are both saturated, we have $f(V_g) = I_{out}$, which gives

$$C \frac{dV_g}{dt} = I_b - I_{out}. \quad (3)$$

For subthreshold operation in saturation, the current through transistors M1 and M2 is [11]

$$f(V_g) = I_{out} = I_o e^{\frac{(\kappa V_g - V_S)}{U_T}}, \quad (4)$$

where I_o is a pre-exponential constant dependent on the transistor's size and on doping concentrations. Also, κ is the body-effect coefficient and U_T is the thermal voltage. V_S is the source voltage, which, for this case, is zero. Setting $V_S = 0$ and taking the derivative of (4) with respect to time, we get

$$\frac{dI_{\text{out}}}{dt} = \frac{\partial}{\partial V_g} \left(I_o e^{\frac{\kappa V_g}{U_T}} \right) \frac{dV_g}{dt}, \quad (5)$$

$$= \frac{\kappa}{U_T} I_{\text{out}} \frac{dV_g}{dt}, \quad (6)$$

which allows us to rewrite (3) as

$$\begin{aligned} \frac{CU_T}{\kappa I_b} \frac{dI_{\text{out}}}{dt} &= I_{\text{out}} \left(1 - \frac{I_{\text{out}}}{I_b} \right) \\ \tau \frac{dI_{\text{out}}}{dt} &= I_{\text{out}} \left(1 - \frac{I_{\text{out}}}{I_b} \right). \end{aligned} \quad (7)$$

The time constant is identified as $\tau = (CU_T)/(\kappa I_b)$.

Equation (7) happens to be the *logistic equation*, a simple model of population dynamics. It can be solved exactly either by separation of variables followed by partial fractions, or by solving it as Bernoulli's equation. The solution is

$$I_{\text{out}}(t) = \frac{I_b e^{t/\tau}}{e^{t/\tau} - 1 + I_b/I_{\text{out}0}}, \quad (8)$$

where $I_{\text{out}0}$ is the initial value of I_{out} . We are lucky to have an exact solution to (7), given that it is a nonlinear differential equation. Even so, it is difficult to discern much useful information about I_{out} 's qualitative behavior from (8). For instance, it is not clear how the behavior of I_{out} might change with different initial conditions. To answer questions of this sort, it is helpful to do geometric analysis on the system's corresponding vector field.

Since the simple current mirror is a one-dimensional system, its vector field is represented as a flow on a line. The direction and speed of the flow are dictated by the right hand side (RHS) of (7). It is a quadratic, as shown in Fig. 4. The I_{out} -intercepts are 0 and I_b . There is a maximum at $I_{\text{out}} = I_b/2$. The vector field

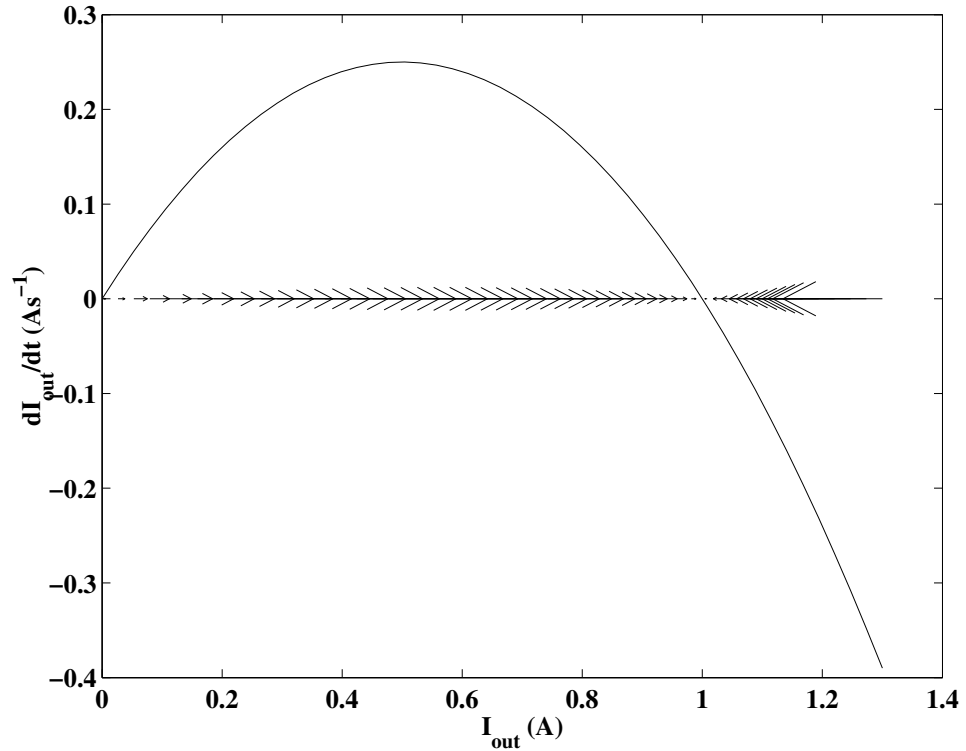


Figure 4. The vector field of the logistic equation is represented as a flow on the I_{out} axis. For positive values of dI_{out}/dt , I_{out} is increasing and the flow is to the right. For negative values of dI_{out}/dt , I_{out} is decreasing and the flow is to the left.

is depicted as the arrows on the I_{out} axis. For positive values of dI_{out}/dt , I_{out} is increasing, meaning the arrows point to the right. For negative values of dI_{out}/dt , I_{out} is decreasing, meaning the arrows point to the left. When $dI_{\text{out}}/dt = 0$, there is no change in I_{out} and the circuit is said to be at equilibrium.

The vector field provides clear, qualitative information about the behavior of I_{out} . There are two equilibrium points, namely $I_{\text{out}} = 0$ and $I_{\text{out}} = I_b$. Note that the vector field flows away from $I_{\text{out}} = 0$. This equilibrium point is unstable, since the system will not recover from slight disturbances away from it. The vector field flows towards $I_{\text{out}} = I_b$, implying that this is a stable equilibrium point. If the system is initially at $I_{\text{out}} = I_b$ and then experiences a small disturbance, it will tend back to the $I_{\text{out}} = I_b$ point.

The vector field in Fig. 4 also gives information about the acceleration of I_{out} as it

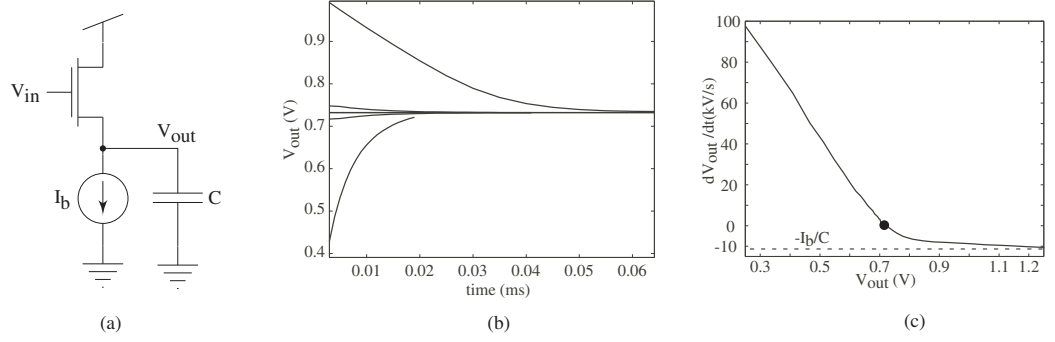


Figure 5. Source follower amplifier acting as a simple peak detector. (a) Circuit that was compiled onto the FPAA. (b) Measured trajectories for different initial conditions. (c) Vector field derived from trajectory measurements. The point 0.7 is a stable equilibrium point.

approaches the $I_{\text{out}} = I_b$ equilibrium point. For $0 < I_{\text{out}} < I_b/2$, the rate of change of I_{out} increases until it reaches a peak at $I_{\text{out}} = I_b/2$. Between $I_b/2$ and I_b , the system decelerates until the rate of change of I_{out} eventually becomes zero. For $I_{\text{out}} > I_b$, the rate of change of I_{out} steadily decreases until $I_{\text{out}} = I_b$. It is interesting to note that, for $I_{\text{out}} < I_b$, the rate of change of I_{out} is limited to a maximum of $I_b/(4\tau)$.

The geometric analysis predictions can be checked against experimental measurements of a current mirror that was compiled onto an FPAA. Figure 3 (b) depicts various trajectories, or solutions, of the system of (7) for different initial conditions. Notice that trajectories that start at values lower than $I_{\text{out}} = I_b/2$ have a sigmoidal shape, with the point of inflection corresponding to the maximum rate of change of current $dI_{\text{out}}/dt = I_b/(4\tau)$. The parabolic shape of dI_{out}/dt can be extracted from these trajectories, and it is shown in Fig. 3 (c).

2.1.2 Simple peak detector

Assuming subthreshold operation, the KCL equation for the source follower amplifier of Fig. 5 (a) is the following.

$$C \frac{dV_{\text{out}}}{dt} = I_0 e^{(\kappa V_{\text{in}} - V_{\text{out}})/U_T} - I_b. \quad (9)$$

Note that

$$\frac{d}{dt}e^{V_{\text{out}}/U_{\text{T}}} = \frac{e^{V_{\text{out}}/U_{\text{T}}}}{U_{\text{T}}} \frac{dV_{\text{out}}}{dt}, \quad (10)$$

in which case, the solution to (9) is

$$V_{\text{out}} = \kappa V_{\text{in}} + U_{\text{T}} \log \left(\frac{I_{\text{o}}}{I_{\text{b}}} - \left(\frac{I_{\text{o}}}{I_{\text{b}}} - e^{(V_{\text{out}_0} - \kappa V_{\text{in}})/U_{\text{T}}} \right) e^{-t/\tau} \right), \quad (11)$$

where $\tau = CU_{\text{T}}/I_{\text{b}}$ and V_{out_0} is the initial value of V_{out} .

The time that it takes for V_{out} to be within 10% of its final value is

$$t_{10} = \tau \log \left| \frac{I_{\text{o}}/I_{\text{b}} - e^{(V_{\text{out}_0} - \kappa V_{\text{in}})/U_{\text{T}}}}{I_{\text{o}}/I_{\text{b}} - e^{0.1\kappa V_{\text{in}}/U_{\text{T}}}} \right|. \quad (12)$$

For an initial condition of V_{out} that is much lower than the equilibrium point, $e^{(V_{\text{out}_0} - \kappa V_{\text{in}})} \approx 0$, and (12) is approximately

$$t_{10} = t_{10+} \approx \tau \log \left| \frac{I_{\text{o}}}{I_{\text{o}} - I_{\text{b}}e^{0.1\kappa V_{\text{in}}/U_{\text{T}}}} \right|. \quad (13)$$

For an initial condition of V_{out} that is much higher than the equilibrium point, $e^{(V_{\text{out}_0} - \kappa V_{\text{in}})} \gg I_{\text{o}}/I_{\text{b}}$, and (12) becomes

$$\begin{aligned} t_{10} = t_{10-} &\approx \tau \log \left| \frac{I_{\text{b}}e^{(V_{\text{out}_0} - \kappa V_{\text{in}})}}{I_{\text{o}} - I_{\text{b}}e^{0.1\kappa V_{\text{in}}/U_{\text{T}}}} \right| \\ &= t_{10+} + \tau \left(\frac{V_{\text{out}_0}}{U_{\text{T}}} - \kappa \frac{V_{\text{in}}}{U_{\text{T}}} \right) \log \left(\frac{I_{\text{b}}}{I_{\text{o}}} \right). \end{aligned} \quad (14)$$

Equations (13) and (14) indicate that the response of the peak detector is slower for a negative input step (which corresponds to an initial condition of V_{out} that is larger than the equilibrium point) than it is for a positive input step (which corresponds to an initial condition of V_{out} that is smaller than the equilibrium point). We surmise that if the system were not homogeneous, and if the input, indicated by V_{in} in Fig. 5 (a) were continuously varying at a rate faster than $1/(t_{10-})$, then the output would be a reasonable representation of the input's peak values. Explaining the peak detector's behavior with (13) and (14) is rigorous, but depends on having to manipulate the expression of (11).

An alternative approach to analyzing the peak detector is to employ intuitive descriptions of the charging action of the active device (*i.e.* the transistor) versus the discharging action of the current source [12]. A more rigorous approach is to apply nonlinear geometric analysis to the problem. Consider the plot of dV_{out}/dt versus V_{out} shown in Fig. 5 (c). It was constructed from a number of trajectory measurements for different initial conditions that were taken after compiling the source-follower amplifier onto the FPAA. For an initial condition of V_{out} that is much higher than the equilibrium point, the rate of growth of V_{out} is bounded by I_b/C . For an initial condition of V_{out} that is much lower than the equilibrium point, the maximum rate at which V_{out} approaches V_{in} can be much greater than I_b/C . The maximum rate of approach in this case is limited only by the initial value, V_{out_0} . As such, there is an asymmetry in the speed of the circuit's response to up-going versus down-going movements on the input. The effect of this asymmetry is that if V_{in} were time-varying, then V_{out} would track increasing V_{in} , and not decreasing V_{in} , which is the behavior of a peak detector.

2.2 Bifurcation

Bifurcation refers to the sudden change in a system's qualitative behavior as a parameter is smoothly varied. We have seen that, in first-order systems, the behavior is largely driven by the nature of the equilibrium points. As such, bifurcation in first-order systems involves either the creation, destruction or change in stability of equilibrium points.

2.2.1 Transcritical bifurcation

The transcritical bifurcation affects first-order systems of the form

$$\dot{x} = rx - x^2, \tag{15}$$

where r is some parameter.

There are two possible equilibrium points for the system of (15), namely $x = 0$ and $x = r$. The stability of the $x = 0$ equilibrium point depends on the sign of r . The transcritical bifurcation occurs at $r = 0$, when the $x = 0$ equilibrium point undergoes an *exchange of stabilities* with the $x = r$ equilibrium point.

While it is possible to construct an analog circuit that undergoes a transcritical bifurcation, it is unlikely to be encountered in normal circuit practice. If we assume that most circuits are nominally linear, then it would not typically be the case that the linear gain of the circuit (which corresponds to the r parameter) can assume both positive and negative values.

For instance, note that the current mirror described by (7) is of the same form as (15). For the current mirror to undergo a transcritical bifurcation, we would require that the current I_b changed directions, which is impossible, given that current must flow from a higher to a lower potential. (As Fig. 3 shows, I_b is flowing from the highest potential in the circuit, the power supply, towards ground.)

2.2.2 Saddle-node bifurcation

Systems that conform to the following description

$$\dot{x} = r - x^2, \tag{16}$$

where r is some parameter, are prone to saddle-node bifurcations.

Such systems can have two equilibrium points if $r > 0$, at $x = \pm\sqrt{r}$, or none at all, if $r < 0$. There is a single equilibrium for $r = 0$. This transition from two to zero equilibrium points is what constitutes the bifurcation. Like the transcritical bifurcation, it is possible to construct an analog circuit that undergoes a saddle-node bifurcation, but it is unlikely to be encountered in most circuit practice¹. This is because, again, of the nominally-linear assumption of circuits; Equation (16) has no linear component at all.

¹One notable exception to this assertion is the example of an root-mean-square to direct current converter [13].

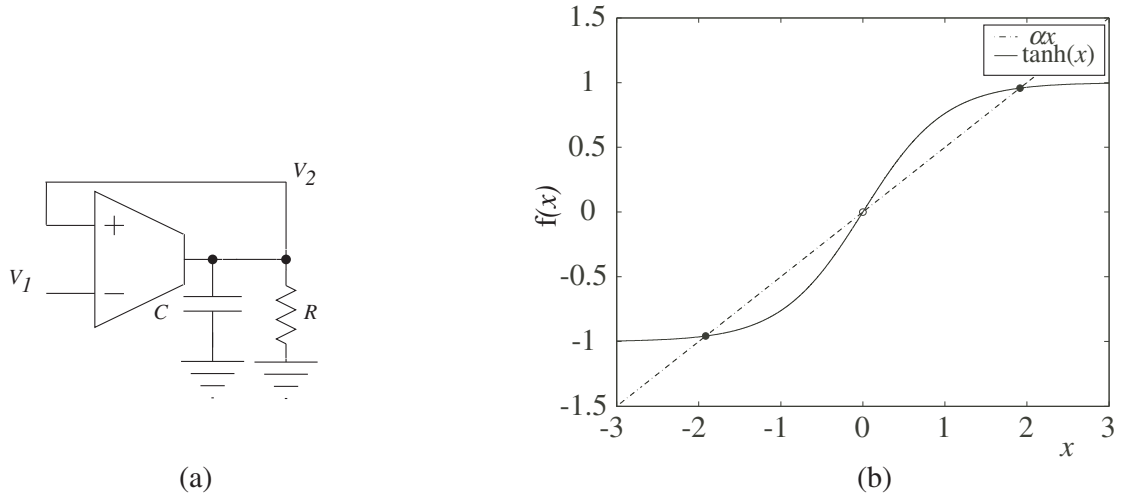


Figure 6. Circuit that is prone to supercritical pitchfork bifurcation. (a) Comparator circuit, created by placing an amplifier in positive feedback, (b) Load lines of (nondimensionalized) comparator circuit. The intersections of the load lines denote equilibrium operating points. As depicted, the origin is an unstable equilibrium and the other two equilibria are stable.

The next two bifurcations to be discussed are more naturally-occurring in circuit design.

2.2.3 Supercritical pitchfork bifurcation

The governing equation of the circuit depicted in Fig. 6 (a) is

$$C \frac{dV_2}{dt} = f(V_1, V_2) + \frac{V_1 - V_2}{R}, \quad (17)$$

where $f(\cdot)$ is the output current of the OTA.

If the OTA is operated in the subthreshold region, then its output current is given by the expression [14]

$$I_{\text{out}} = I_b \tanh \left(\frac{\kappa}{2U_T} (V_2 - V_1) \right), \quad (18)$$

where κ is the body-effect coefficient and U_T is the thermal voltage [11]. Also, I_b is

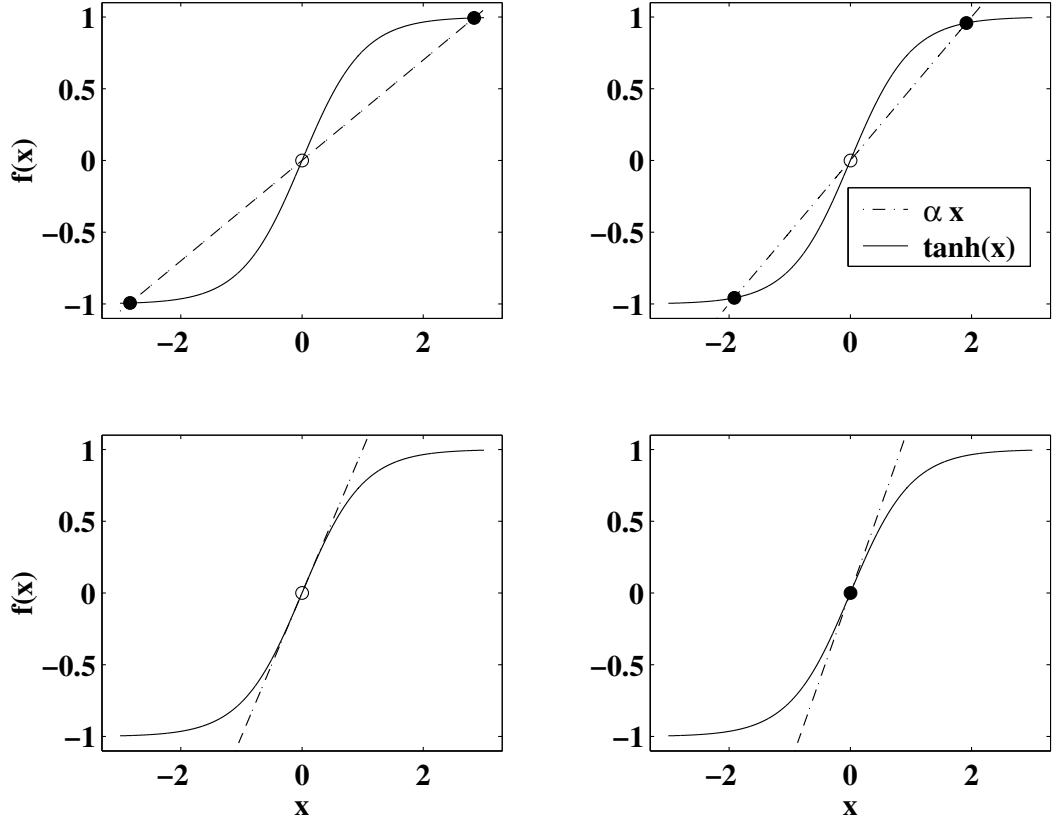


Figure 7. Progression of supercritical pitchfork bifurcation. From left to right and top to bottom, the values of α are (a) $\alpha = 0.35$, (b) $\alpha = 0.5$, (c) $\alpha = 1$, (d) $\alpha = 1.2$.

a tunable bias current. For ease of argument, assume $V_1 = 0$ and define

$$x = \frac{\kappa}{2U_T}(V_2), \quad (19)$$

$$\tau = \frac{CU_T}{I_b\kappa}, \quad (20)$$

$$\alpha = \frac{2U_T}{\kappa I_b R}. \quad (21)$$

The governing equation can then be written as

$$\tau \frac{dx}{dt} = \tanh(x) - \alpha x. \quad (22)$$

The equilibrium points of the circuit are at the intersection of the curves $\tanh(x)$ and αx .

As shown in Fig. 6 (b), there are three equilibrium points. The stability of these equilibrium points can be determined via linearization. We will defer the linearization

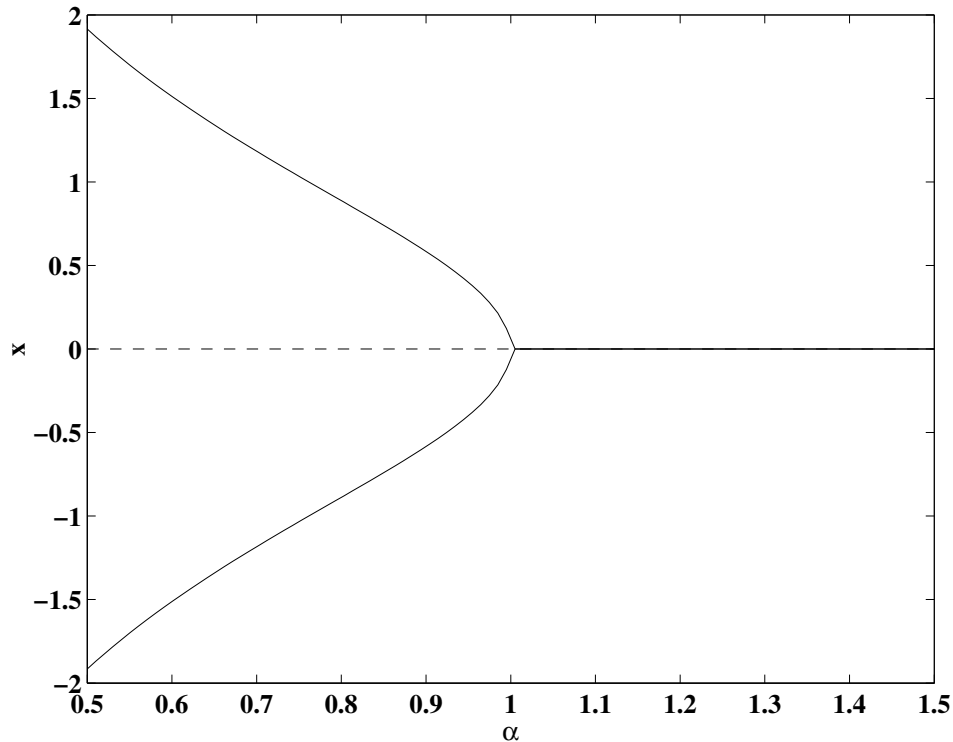


Figure 8. Supercritical pitchfork bifurcation. Solid curves represent stable equilibrium points and dashed curves represent unstable equilibrium point.

method to the section on second-order systems. For first-order systems, we can infer the stability of the equilibrium points by a simpler method.

Consider the region that surrounds the $x = 0$ point of the plot in Fig. 6 (b). For slightly positive values of x , we have $\alpha x < \tanh(x)$, which implies $\dot{x} > 0$. Also, for slightly negative values of x , we have $\alpha x > \tanh(x)$, which implies $\dot{x} < 0$. So, if x is perturbed slightly from the point $x = 0$, the system tends to amplify this perturbation. This means that $x = 0$ is an unstable equilibrium point. Using a similar argument, we conclude from inspection that the other two equilibrium points are stable.

The equilibrium points depicted in Fig. 6 (b) are incidental only to the particular value of α we chose. Figure 7 shows the different plots for four representative values of α . As the parameter α is increased towards a value of $\alpha = 1$, the two stable

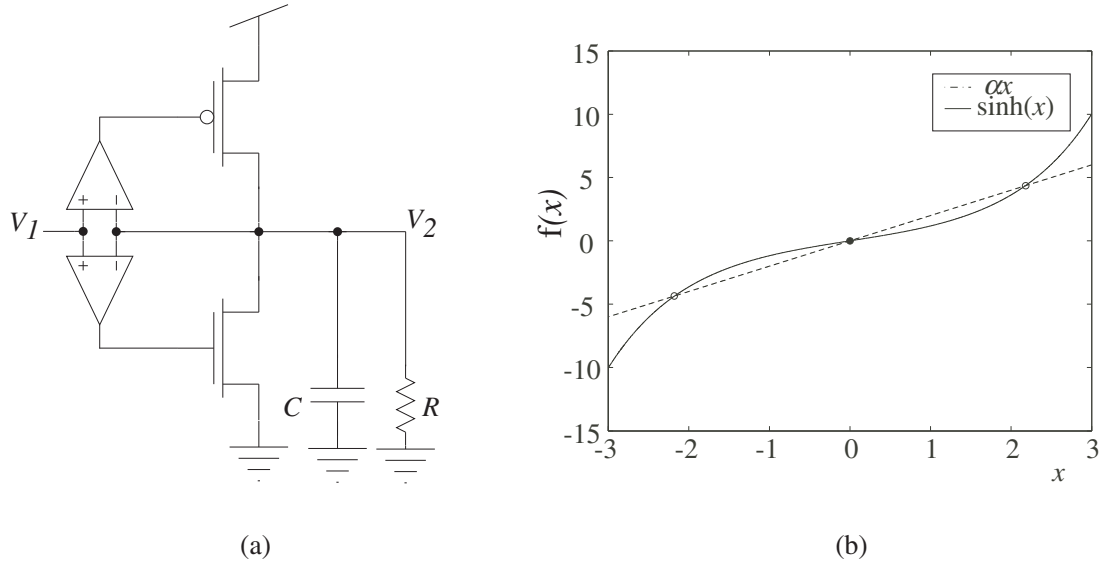


Figure 9. Circuit that is prone to subcritical pitchfork bifurcation. (a) Positive-feedback buffer circuit, (b) Load lines of (nondimensionalized) buffer circuit. The intersections of the load lines denote equilibrium operating points. As depicted, the origin is a stable equilibrium and the other two equilibria are unstable.

equilibrium points move closer towards the unstable origin. Eventually, all three equilibrium points coalesce at $\alpha = 1$. For $\alpha > 1$, the origin is the only remaining equilibrium point and it is now stable.

Figure 8 shows a plot of the positions of the equilibrium points as a function of α . A dashed curve denotes instability, while a solid curve denotes stability. The shape of the curves in Fig. 8 lends itself to the name of this phenomenon; it is a supercritical pitchfork bifurcation. The identifying characteristics of a pitchfork bifurcation are that

- (a) two stable equilibrium points coalesce with one unstable equilibrium point to create a single stable equilibrium point, and that
- (b) the canonical form is $\dot{x} = rx - x^3$.

Note that, close to the origin, the system $\dot{x} = \tanh(x) - \alpha x$ resembles $\dot{x} = rx - x^3$.

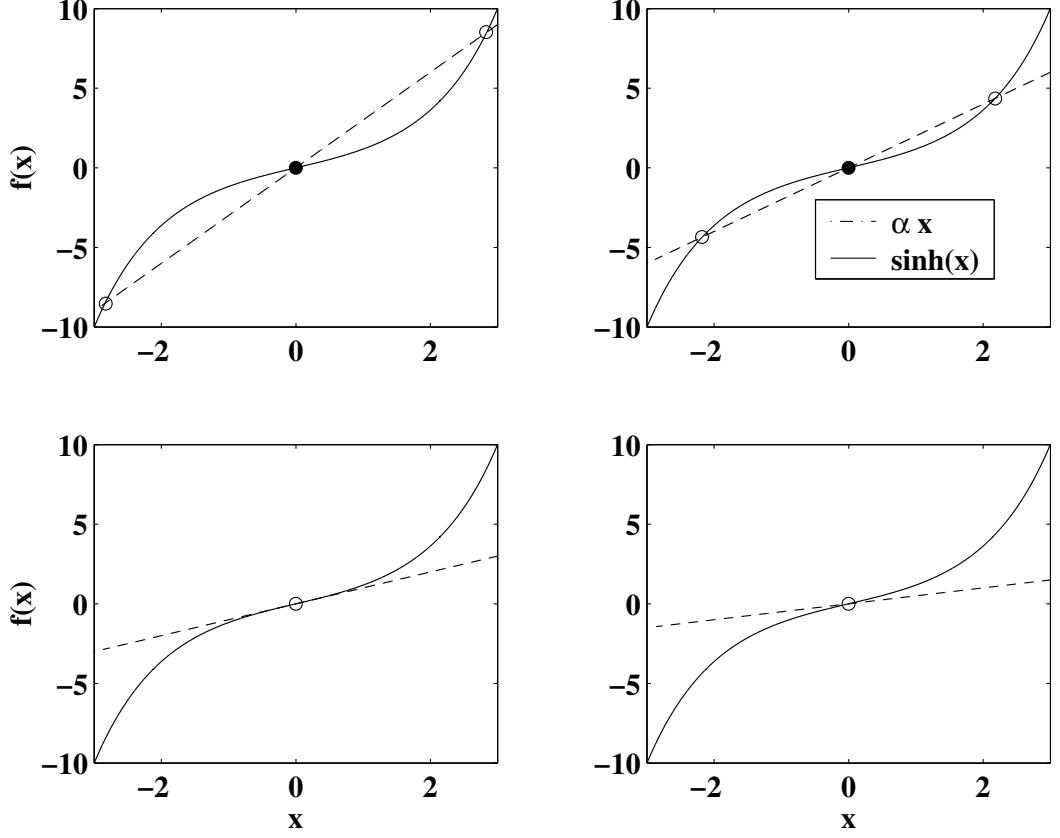


Figure 10. Progression of subcritical pitchfork bifurcation. From left to right and top to bottom, the values of α are (a) $\alpha = 3$, (b) $\alpha = 2$, (c) $\alpha = 1$, (d) $\alpha = 0.5$.

2.2.4 Subcritical pitchfork bifurcation

The governing equation of the circuit depicted in Fig. 9 (a) is

$$C \frac{dV_2}{dt} = I_p e^{-\frac{\kappa}{U_T} A(V_1 - V_2)} - I_n e^{\frac{\kappa}{U_T} A(V_1 - V_2)} - \frac{V_2}{R}, \quad (23)$$

where I_p and I_n are pre-exponential currents for the p-type and n-type transistors, respectively, assumed to be in subthreshold operation. Also, A is the gain of the amplifiers. If the transistors are sized correctly, then we have $I_p = I_n = I_o$. Take $V_1 = 0$ and define

$$x = \frac{\kappa A V_2}{U_T}, \quad (24)$$

$$\tau = \frac{C U_T}{I_o \kappa A}, \quad (25)$$

$$\alpha = \frac{U_T}{\kappa I_o A R}. \quad (26)$$

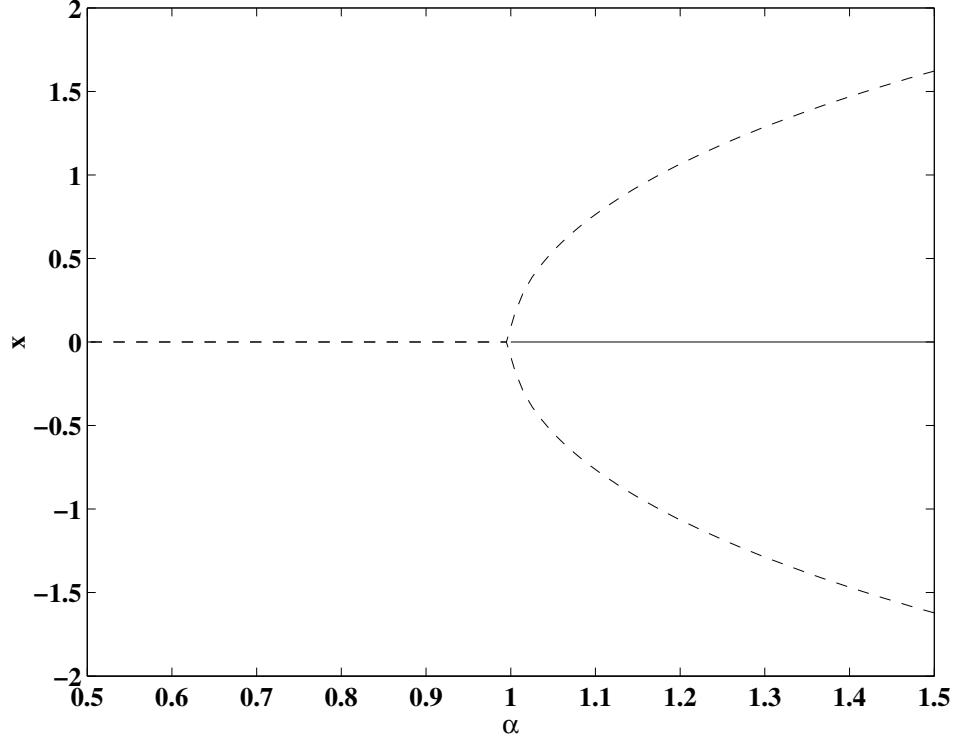


Figure 11. Subcritical pitchfork bifurcation. Solid curves represent stable equilibrium points and dashed curves represent unstable equilibrium point.

The governing equation can then be written as

$$\tau \frac{dx}{dt} = \sinh(x) - \alpha x. \quad (27)$$

The equilibrium points of the circuit are at the intersection of the curves $\sinh(x)$ and αx .

The plot in Fig. 9 (b), shows the equilibrium points for $\alpha = 2$. For this value of α , the origin is a stable equilibrium point, while the other two equilibrium points are unstable.

Figure 10 shows the different plots for four representative values of α . As the parameter α is decreased towards a value of $\alpha = 1$, the two unstable equilibrium points move closer towards the stable origin. Eventually, all three equilibrium points coalesce at $\alpha = 1$. For $\alpha < 1$, the origin is the only remaining equilibrium point and it is now unstable.

Figure 11 shows a plot of the positions of the equilibrium points as a function of α , depicting a subcritical pitchfork bifurcation. The identifying characteristics of a pitchfork bifurcation are that

- (a) two unstable equilibrium points coalesce with one stable equilibrium point to create a single unstable equilibrium point, and that
- (b) the canonical form is $\dot{x} = rx + x^3$.

Note that, around to the origin, the system $\dot{x} = \sinh(x) - \alpha x$ resembles $\dot{x} = rx + x^3$.

2.2.5 Occurrence of bifurcations in normal circuit design

The bifurcations that have been presented, as well as many of the others not discussed, tend to occur mostly in circuits that have some level of positive feedback. While positive feedback is generally avoided as a matter of good circuit practice, there are many situations where positive feedback is needed. In these situations, it is helpful to use bifurcation theory in order to assess the potential harm of various positive feedback options to the overall design. Take, for instance, a circuit that incorporates positive feedback, but that is designed to ideally have a unique stable point. A good example of this situation is a self-biased or bootstrapped current reference [15]. Imperfections in the IC fabrication process may cause a deviation from the ideal case of a unique stable point. In this situation, it would be more desirable that the circuit be chosen such that it undergoes a supercritical pitchfork bifurcation rather than a subcritical pitchfork bifurcation. This is because there is a more graceful degradation in performance after the supercritical bifurcation, whereas a subcritical bifurcation results in complete and sudden loss of stability.

CHAPTER 3

HOMOGENEOUS SYSTEMS II: SECOND-ORDER CIRCUITS

In this chapter, we will consider how the concepts of geometric analysis, equilibrium points and bifurcation extend to circuits with second-order dynamics of the form

$$\dot{\mathbf{x}} = f(\mathbf{x}), \quad (28)$$

where $\mathbf{x} = [x_1, x_2]^T$ represents two physical quantities.

The circuit in Fig. 12 is the quintessential example of a second-order circuit. It was first presented by Lyon *et al.* as a silicon model of the cochlea [14]. Assuming that the OTAs are based on subthreshold MOS transistor differential pairs, KCL provides the following governing equations for the circuit of Fig. 12

$$C_1 \frac{dV_1}{dt} = I_1 \tanh\left(\frac{\kappa(V_{\text{in}} - V_1)}{2U_T}\right) - I_3 \tanh\left(\frac{\kappa(V_2 - V_1)}{2U_T}\right) \quad (29)$$

$$C_1 \frac{dV_2}{dt} = \frac{I_2}{k} \tanh\left(\frac{\kappa(V_1 - V_2)}{2U_T}\right), \quad (30)$$

where $I_{1,2,3}$ are the bias currents of the OTAs. Also, k is the ratio of the C_2 to C_1 .

If we define

$$x_1 = \frac{\kappa(V_1 - V_{\text{in}})}{2U_T}, \quad x_2 = \frac{\kappa(V_2 - V_1)}{2U_T}, \quad (31)$$

then Equations (29) and (30) become

$$\begin{aligned} \frac{2U_T C_1}{\kappa} \frac{dx_1}{dt} &= -I_1 \tanh(x_1) - I_3 \tanh(x_2) \\ \frac{2U_T C_1}{\kappa} \frac{dx_2}{dt} &= I_1 \tanh(x_1) + \left(I_3 - \frac{I_2}{k}\right) \tanh(x_2). \end{aligned} \quad (32)$$

Assume for now that V_{in} is a fixed voltage.

Further defining

$$\begin{aligned} I_1 &= I_{\text{bias}}, & I_2 &= gkI_{\text{bias}} \\ I_3 &= 2rI_{\text{bias}}, & t &= \tau \cdot \frac{2U_T C_1}{\kappa I_{\text{bias}}}, \end{aligned}$$

where $g \geq 0$, we get the following dimensionless equation

$$\begin{aligned}\frac{dx_1}{d\tau} &= -\tanh(x_1) - 2r \tanh(x_2) \\ \frac{dx_2}{d\tau} &= \tanh(x_1) + (2r - g) \tanh(x_2).\end{aligned}\tag{33}$$

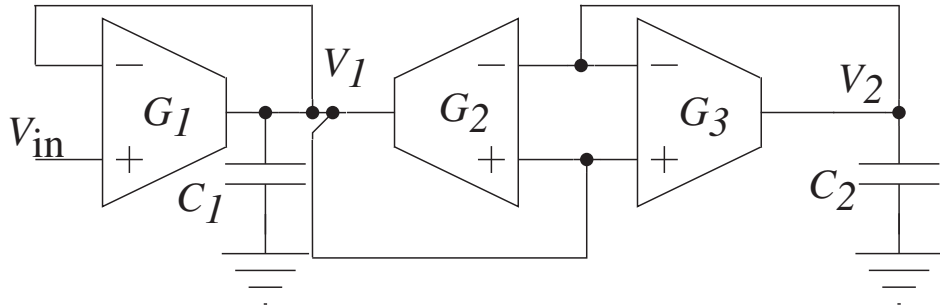


Figure 12. Second order section. Varying the bias currents of the various amplifiers leads to interesting dynamics.

3.1 Equilibrium points

We find the equilibrium points of the system by setting the RHS of (33) to zero and solving for x_1 and x_2 . For (33), the only equilibrium point is the origin. Let us denote the equilibrium point with asterisks. That is, $(x_1^*, x_2^*) = (0, 0)$.

We can predict the behavior of this equilibrium point by analyzing a linearized approximation of (33). First, replace the RHS of (33) with its Jacobian, which is the matrix formed by taking the partial derivatives of the nonlinear functions with respect to each state variable. For (33), the Jacobian is

$$\mathbb{J} = \begin{bmatrix} \tanh^2(x_1) - 1 & 2r \tanh^2(x_2) - 2r \\ 1 - \tanh^2(x_1) & (2r - g)(1 - \tanh^2(x_2)) \end{bmatrix}.\tag{34}$$

The linearized approximation of (33) is

$$\begin{bmatrix} \dot{x}_1 \\ \dot{x}_2 \end{bmatrix} \approx \begin{bmatrix} \tanh^2(x_1) - 1 & 2r \tanh^2(x_2) - 2r \\ 1 - \tanh^2(x_1) & (2r - g)(1 - \tanh^2(x_2)) \end{bmatrix} \begin{bmatrix} x_1 \\ x_2 \end{bmatrix}.\tag{35}$$

The characteristics of the equilibrium point depend on the eigenvalues of the Jacobian matrix when it is evaluated at that point. At the equilibrium point, we have

$$\mathbb{J}|_{(0,0)} = \begin{bmatrix} -1 & -2r \\ 1 & 2r - g \end{bmatrix}, \quad (36)$$

the eigenvalues of which are

$$\begin{aligned} \lambda_1 &= \frac{\tau + \sqrt{\tau^2 - 4\Delta}}{2} \\ \lambda_2 &= \frac{\tau - \sqrt{\tau^2 - 4\Delta}}{2}, \end{aligned} \quad (37)$$

where $\tau = 2r - g - 1$ and $\Delta = g$ are the trace and determinant of $\mathbb{J}|_{(0,0)}$, respectively.

Recall from the definition of g as a ratio of currents that $\Delta > 0$. Now, if $\tau^2 < 4\Delta$, then the eigenvalues are complex conjugates, implying an oscillatory, or spiraling, motion in the vicinity of the equilibrium point. This type of equilibrium point is a *spiral* and the behavior that it elicits is referred to in, classical circuit terms, as “ringing”. If $\tau^2 > 4\Delta$, then the eigenvalues are real-valued, and the behavior of x_1 and x_2 is exponential or nodal. This type of equilibrium point is a *node* and the behavior that it elicits is referred to in, classical circuit terms, as a “damped response”. For $\tau < 0$, the real part of the eigenvalues is negative and the equilibrium point is stable. For $\tau > 0$, the real part of the eigenvalues is positive and the equilibrium point is unstable. For completeness, note that if $\Delta < 0$, then the eigenvalues would have opposite signs, and the equilibrium point would be a saddle point.

In terms of the circuit parameters r and g , the origin is stable for

$$r < \frac{1+g}{2}, \quad (38)$$

and unstable otherwise. It is a spiral for

$$\frac{1+g}{2} - \sqrt{g} < r < \frac{1+g}{2} + \sqrt{g}, \quad (39)$$

and a node otherwise.

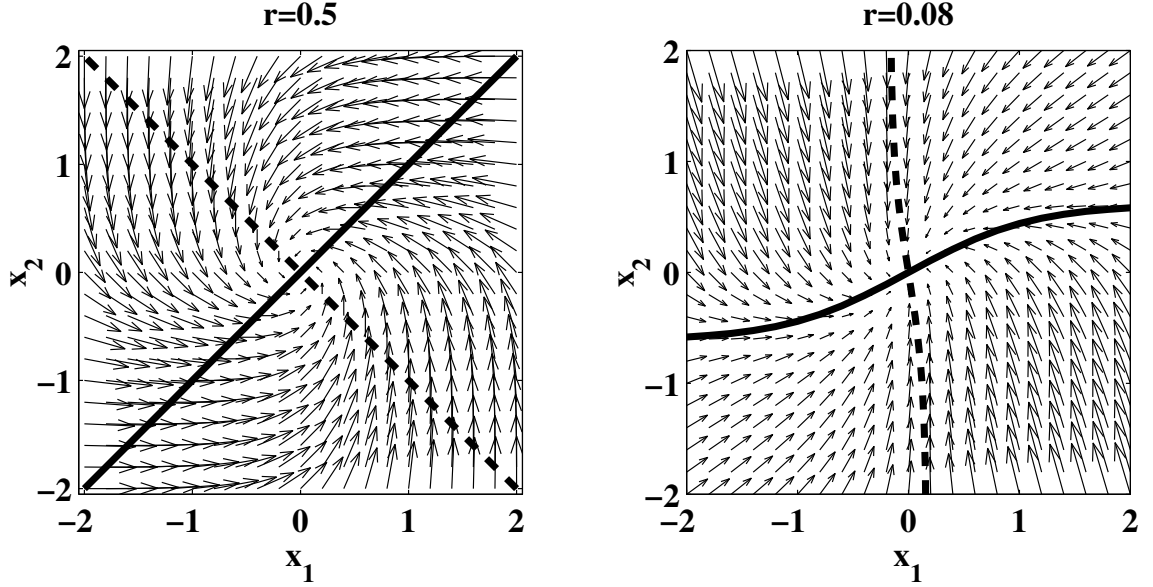


Figure 13. Phase plane portraits for the system of (33). The dashed curve is the $x_1 = 0$ nullcline and the solid curve is the $x_2 = 0$ nullcline. The plot on the left is for $r = 0.5$ and that on the right is for $r = 0.08$. For both cases, $g = 2$.

3.2 Phase plane portrait

For a two-dimensional system such as (33), the vector field is defined on the x_1, x_2 plane. Each point in the plane has a corresponding velocity vector, given by the RHS of (33). Figure 13 shows phase plane portraits of (33). Some pertinent features are the nullclines, which are the lines where $\dot{x}_1 = 0$ or $\dot{x}_2 = 0$, and the equilibrium point, which is the intersection of the nullclines.

The phase plane portraits shown in Fig. 13 are for $r < \frac{1+g}{2}$, when the equilibrium point is stable. Figure 13 (a) shows the portrait for $(1+g)/2 - \sqrt{g} < r < (1+g)/2 + \sqrt{g}$ and the equilibrium point is a spiral. In Fig. 13 (b), $r > (1+g)/2 + \sqrt{g}$ and the equilibrium point is a node.

3.3 Impulse and step response

The step and impulse responses are useful ways to evaluate certain characteristics of a system. For a linear system, the step response reveals what type of an equilibrium

point the origin is. For instance, the step response of a linear system with a stable spiral equilibrium point is a damped oscillation. This subsection introduces a method for analyzing input responses that is valid for both linear and nonlinear systems.

3.3.1 Impulse response

Defining $y = \kappa V_1 / (2U_T)$, and $u = \kappa V_{in} / (2U_T)$, (33) becomes

$$\begin{aligned}\frac{dy}{d\tau} &= -\tanh(y - u) - 2r \tanh(x_2) \\ \frac{dx_2}{d\tau} &= \tanh(y - u) + (2r - g) \tanh(x_2).\end{aligned}\quad (40)$$

The impulse response of the circuit is the solution to (40) with $u = A_{in}\delta(\tau)$, where A_{in} is the weight of the impulse. The solution can be found by considering the two time regions $0^- \leq \tau < 0^+$ and $\tau \geq 0^+$.

Region I: $0^- \leq \tau < 0^+$.

Multiplying both sides of (40) by $d\tau$ and integrating yields

$$\begin{aligned}\int_{0^-}^{0^+} dy &= -\int_{0^-}^{0^+} \tanh(y - u) + 2r \tanh(x_2) d\tau \\ \int_{0^-}^{0^+} dx_2 &= \int_{0^-}^{0^+} \tanh(y - u) + (2r - g) \tanh(x_2) d\tau.\end{aligned}\quad (41)$$

With $u = A_{in}\delta(\tau)$, this simplifies to

$$\begin{aligned}y(0^+) &= y(0^-) + \tanh(A_{in}) \\ &= y(0) + \tanh(A_{in}) \\ x_2(0^+) &= x_2(0^-) - \tanh(A_{in}) \\ &= x_2(0) - \tanh(A_{in}).\end{aligned}\quad (42)$$

Region II: $\tau \geq 0^+$.

In this region, $u = 0$ and (40) becomes

$$\begin{aligned}\frac{dy}{d\tau} &= -\tanh(y) - 2r \tanh(x_2) \\ \frac{dx_2}{d\tau} &= \tanh(y) + (2r - g) \tanh(x_2).\end{aligned}\quad (43)$$

The overall effect of an input impulse of weight A_{in} , then, is to shift the initial condition of the system from $(y(0), x_2(0))$ to $(y(0) + \tanh(A_{\text{in}}), x_2(0) - \tanh(A_{\text{in}}))$.

3.3.2 Step response

The step response too is derived by dividing the problem into two time regions, but with the input $u = A_{\text{in}}\theta(\tau)$, where $\theta(\tau)$ is the unit step function.

Region I: $0^- \leq \tau < 0^+$.

The input is $u = 0$ and nothing changes. That is, the initial conditions remain the same.

Region II: $\tau \geq 0^+$.

The input is $u = A_{\text{in}}$. Equation (40) becomes

$$\begin{aligned}\frac{dy}{d\tau} &= -\tanh(y - A_{\text{in}}) - 2r \tanh(x_2) \\ \frac{dx_2}{d\tau} &= \tanh(y - A_{\text{in}}) + (2r - g) \tanh(x_2).\end{aligned}\tag{44}$$

The overall effect of a step input of size A_{in} is to change the system from $\dot{\mathbf{x}} = f(\mathbf{x}, 0)$, to $\dot{\mathbf{x}} = f(\mathbf{x}, A_{\text{in}})$, where the second argument of $f(\cdot)$ is equivalent to a control parameter.

3.4 Bifurcation

The circuit of Fig. 12 contains an OTA that is connected in a positive feedback configuration. As discussed earlier, bifurcating behavior is often observed in circuits that contain a positive feedback path. In fact, we have already noted, via linearization and analysis of the Jacobian matrix, that the type and stability of the equilibrium point at the origin is dependent on the value of r .

In particular, as r passes through the critical point $r_c = (1 + g)/2$ from left to right, the equilibrium point changes from a stable spiral to an unstable spiral. The change in stability of a spiral is normally indicative of a Hopf bifurcation. In most physical systems, two kinds of Hopf bifurcation are possible. There is the supercritical

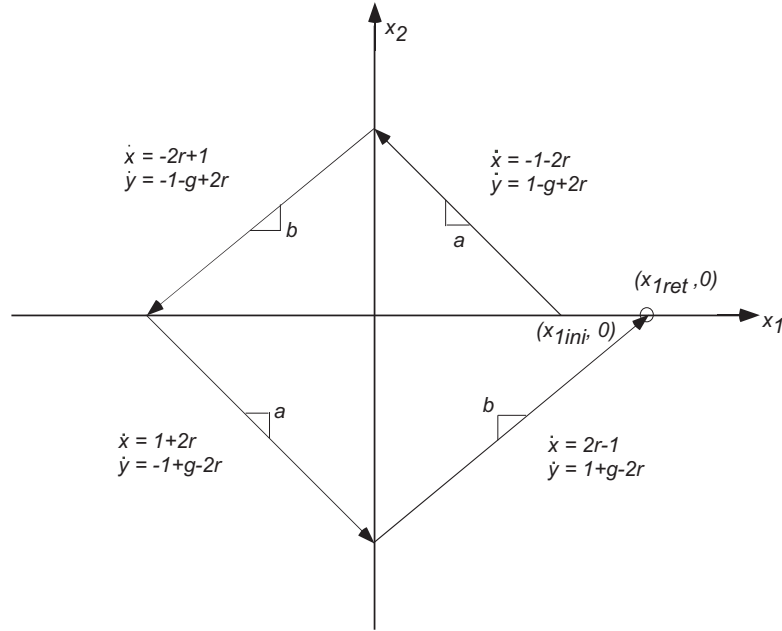


Figure 14. Sketch of the SOS phase plane for large signals. The solution curve traces out a rough quadrilateral. If the edges of the quadrilateral are not contained, then instability occurs. The point $(x_{1ret}, 0)$ shown in the plot is given by the expression in (46)

Hopf, which results in a small limit cycle surrounding the spiral equilibrium point immediately after it loses stability. There is also the subcritical Hopf bifurcation, where a stable spiral point becomes unstable after it is enclosed by a steadily-shrinking unstable limit cycle.

For the system of Fig. 12, we need to determine which type of Hopf bifurcation occurs at $r = (1 + g)/2$. An analytical approach is described in [16], but we will use a geometrical approach to determine whether the Hopf bifurcation is subcritical or supercritical. The idea is to detect the presence of any limit cycles surrounding the spiral equilibrium point, close to the point of bifurcation. We can determine the existence of a stable limit cycle via the Poincaré-Bendixon Theorem¹ [17], which states that if

¹It is worth noting here that the Poincaré-Bendixson theorem is only valid for two-dimensional systems. However, the stability and type of Hopf bifurcation can be determined for higher dimensional systems as long as the appropriate pair of eigenvalues is chosen. Also, numerical software tools do exist that can perform the required analysis on higher-order models

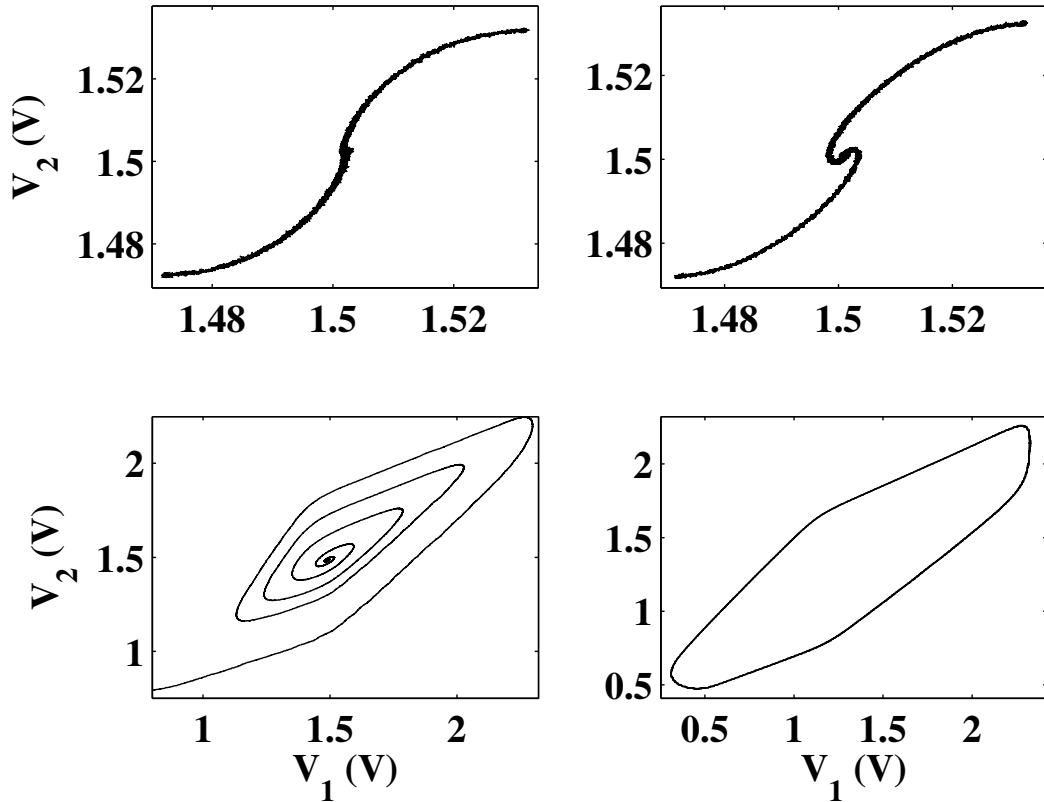


Figure 15. Experimental SOS's phase plane plots for various values of r , with g fixed. Just as predicted, there is a unique equilibrium point, which is initially stable, and gradually changes from a node to a spiral (top and bottom left panels). While linear analysis would predict these three responses as damped, slightly underdamped, and very underdamped, it fails to recognize the possibility of the fourth response, which is large-signal instability. In the fourth panel, r meets the criterion derived from nonlinear analysis, (45), and we observe oscillation.

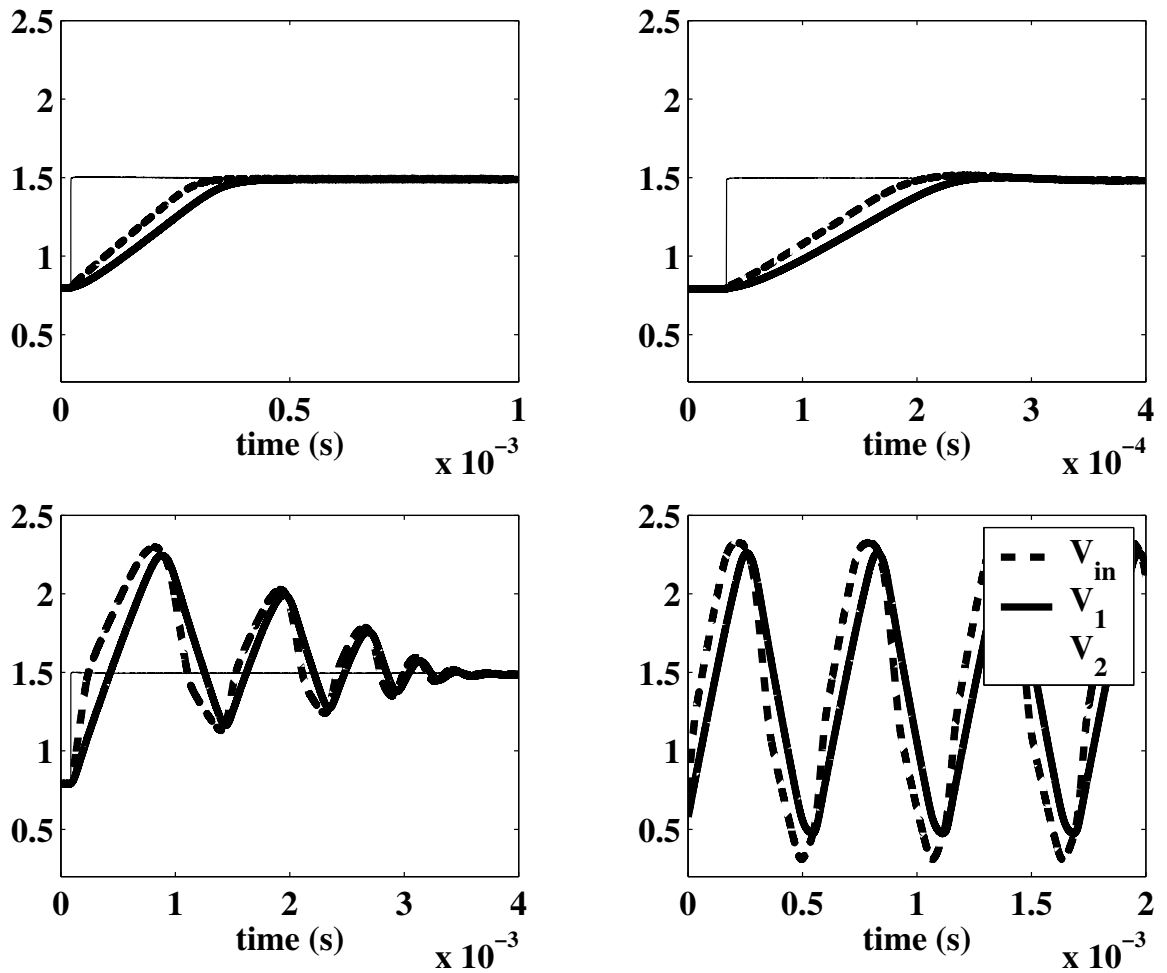


Figure 16. Experimental SOS's step responses for various values of r , with g fixed. The system is initially stable and over damped. The amount of ringing gradually increases until the system becomes large-signal unstable and displays a sustained oscillation. Linear analysis fails to recognize the possibility of this behavior, when r meets the criterion derived from nonlinear analysis, (45).

- (1) R is a closed, bounded subset of the plane;
 - (2) $\dot{\mathbf{x}} = f(\mathbf{x})$ is a continuously differentiable vector field on an open set containing R ;
 - (3) R does not contain any equilibrium points; and
 - (4) There exists a trajectory C that is confined in R ,
- then either C is a closed orbit, or it spirals toward a closed orbit as $t \rightarrow \infty$.

As a corollary to the Poincaré-Bendixon Theorem, if criteria listed (1)-(3) are satisfied, and criterion (4) is replaced by

- (4') No trajectories are admitted into R , in the sense that all trajectories that start outside R stay outside R for all future time,
- then there is an unstable closed orbit in R .

Let us examine the system (33) for r close to the bifurcation point and see if a “detrapping region” R can be defined that satisfies (4'). Assume $r < (1 + g)/2$; that is, the origin is a stable equilibrium point. Consider an annulus surrounding the origin. If the inner boundary of the annulus is a small enough circle around the origin, then all trajectories on this boundary will be pointing out of the annular region. This means that no trajectories can enter the annular region via the inner boundary. Assume the outer boundary is large enough that the annulus contains points far from the origin. At these points, the saturating behavior of the tanh function can be used to approximate (33) as

$$\begin{aligned}\frac{dx_1}{d\tau} &= -\text{sgn}(x_1) - 2r\text{sgn}(x_2) \\ \frac{dx_2}{d\tau} &= \text{sgn}(x_1) + (2r - g)\text{sgn}(x_2).\end{aligned}\tag{45}$$

A trajectory that starts at $(x_1, x_2) = (x_{1\text{ini}}, 0)$, where $x_{1\text{ini}} \gg 1$ will trace out the path depicted by Fig. 14. It will return to the x_1 axis at point

$$(x_1, x_2) = \left(x_{1\text{ini}} \cdot \left(\frac{2r - 1 + g}{1 + 2r} \right)^2 \left(\frac{1 - 2r}{2r - 1 - g} \right)^2, 0 \right).\tag{46}$$

If the point of return at the x_1 axis is larger than $x_{1\text{ini}}$, then it can be proven by induction that the trajectory will eventually leave the annular region. The condition that the point of return at the x_1 axis is larger than $x_{1\text{ini}}$ will be met if

$$\frac{2r - 1 + g}{1 + 2r} > \frac{2r - 1 - g}{1 - 2r}, \quad (47)$$

or, more succinctly, if

$$r > \frac{g + \sqrt{g^2 + 4}}{4}. \quad (48)$$

With the identification of a detrapping region for $(g + \sqrt{g^2 + 4})/4 < r < (1 + g)/2$, we know that the system has an unstable limit cycle. This limit cycle shrinks as r approaches $r_c = (1 + g)/2$, until it completely envelopes the origin, converting it to an unstable spiral equilibrium point. We therefore conclude that the circuit of Fig. 12 undergoes a subcritical Hopf bifurcation, as shown in Figs. 15 and 16. Interestingly, a slight adjustment of the circuit can elicit a supercritical Hopf bifurcation [18]. The resulting stable limit cycle will be discussed in detail in Chapter 6.

CHAPTER 4

NONHOMOGENEOUS SYSTEMS I: FIRST-ORDER CIRCUITS

Whenever designers want to get an analytical handle on the sources and causes of nonlinear distortion, the most commonly-used tool is Volterra series analysis. If a problem is tractable using Volterra series, then it can also be solved with perturbation theory, which will yield asymptotically-identical results [19].

There are certain problems for which Volterra series are ill-suited — multiple-time-scale behavior and multiple steady states, for instance [20]— that can be solved with perturbation theory. Despite the power of perturbation theory, it is still a relatively obscure concept in discussions about nonlinearity and distortion in analog circuits. It is therefore worthwhile to present a basic treatment of regular perturbation — the simplest perturbation method — as applied to distortion analysis of first-order analog circuits [21]. The treatment in this chapter will illustrate how well-known tenets of low-distortion design, such as feedback, are readily derived from the perturbation method.

4.1 Regular perturbation

Consider the initial value problem

$$\dot{x} = f(t, x, \epsilon); x(t_0) = x_0(\epsilon), \quad (49)$$

where ϵ is a small perturbation parameter such that $\epsilon = 0$ yields an analytically-soluble equation. If f is sufficiently smooth¹, then the problem has a unique solution $x(t, \epsilon)$. As the solution for $\epsilon \neq 0$ may not be analytical, it can be approximated as a

¹The specific smoothness requirements of f are discussed in [17]

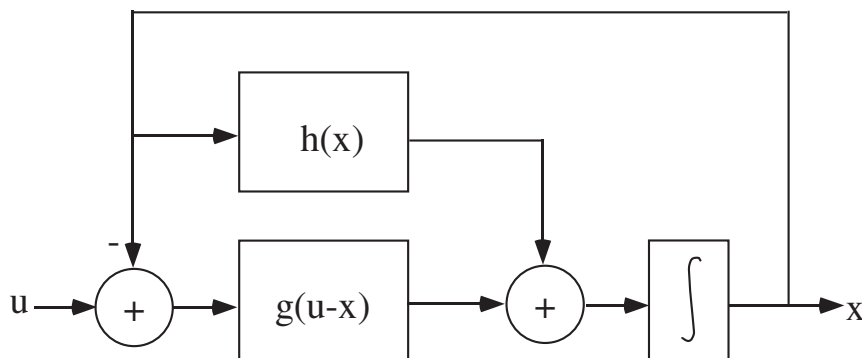


Figure 17. General block diagram form of a first-order circuit. The primary processing block is $g(\cdot)$, which is a nonlinear function of the input u and of x via feedback. The nonlinearity $h(x)$ models such nonidealities as finite output impedance.

power series in ϵ to an accuracy of $O(\epsilon^{n+1})$. That is, we can write the solution as

$$x(t, \epsilon) = \underbrace{\sum_{i=0}^n (x_i(t)\epsilon^i)}_{\hat{x}(t, \epsilon)} + O(\epsilon^{n+1}) \quad (50)$$

where $\hat{x}(t, \epsilon)$ is the approximate solution. To conduct regular perturbation, we apply the substitution $x(t, \epsilon) \approx \hat{x}(t, \epsilon)$ to (49). The resulting system is then solved by equating like powers of ϵ . The following sections will illustrate this idea.

4.2 The basic first-order circuit

Most common first-order analog circuits (simple amplifiers, buffers, switches, etc.) are of the form depicted in Fig. 17. The governing equation is

$$\dot{x} = g(u - x) + h(x), \quad (51)$$

where u is the a.c. input signal, x is the a.c. output signal and $g(\cdot)$ and $h(\cdot)$ are nonlinear functions. The dependence of the system on the output, other than through feedback to the input, is modeled by $h(x)$. In practice, $h(x)$ is typically some non-ideality such as finite output resistance.

In order to apply perturbation analysis to (51), we begin by assuming that the input signal has a small amplitude. This is expressed as $u = \epsilon v$, where ϵ is a small perturbation parameter and v is a suitably-scaled version of the input signal. Note that with the definition of u , (51) is solvable via separation of variables for the special case $\epsilon = 0$.

With the introduction of the perturbation parameter ϵ , we can approximate the solution to (51) with the power series

$$x(t) \approx \sum_{i=1}^n \epsilon^i x_i(t). \quad (52)$$

Note the ϵ^0 term of (52) is set to 0. This corresponds to analyzing a circuit about its d.c. bias point, where the d.c. bias point is shifted to the origin. For ease of notation, define $z = u - x$. The approximation of z is defined similarly to (52), with $z_1 = v - x_1$ and $z_i = -x_i, \forall i > 1$.

If ϵ is sufficiently small, then the functions $g(z)$ and $h(x)$ can be approximated by their truncated Taylor series as

$$\begin{aligned} g(z) &\approx g_1 z + g_{n-1} z^{n-1} + g_n z^n \\ h(x) &\approx h_1 x + h_{n-1} x^{n-1} + h_n x^n, \end{aligned} \quad (53)$$

Functions g and h are assumed to be dominantly $(n - 1)^{\text{th}}$ -order nonlinearities, with $g_i = g^{(i)}(0)/i!$ and $h_i = h^{(i)}(0)/i!$. Equation (53) assumes $g(0) = h(0) = 0$, which, again, corresponds to analyzing a circuit about its d.c. bias point.

Substituting (52) and (53) into (51) and collecting powers of ϵ , we get the following

set of first-order *linear* equations

$$\begin{aligned}
\dot{x}_1 + (g_1 - h_1)x_1 &= g_1v \\
&\vdots \\
\dot{x}_k + (g_1 - h_1)x_k &= 0 \quad \forall k < n - 1 \\
&\vdots \\
\dot{x}_{n-1} + (g_1 - h_1)x_{n-1} &= g_{n-1}z_1^{n-1} + h_{n-1}x_1^{n-1} \\
\dot{x}_n + (g_1 - h_1)x_n &= g_nz_1^n - ng_{n-1}z_1^{n-1}x_2 + \\
&\quad h_nx_1^n - nh_{n-1}x_1^{n-1}x_2.
\end{aligned} \tag{54}$$

The ϵ^1 equation is the linearized portion of (51) with input v . Taking the Laplace transform of this equation, we write

$$X_1(s) = g_1H(s)V(s), \tag{55}$$

where $H(s) = 1/(s + g_1 - h_1)$.

The ϵ^k equations ($k < (n - 1)$) are filters with 0 input. As such, the steady state solutions of these equations is 0.

4.3 Harmonic distortion terms

The inputs of the ϵ^{n-1} equation are terms of z_1^{n-1} and x_1^{n-1} . To understand the implications of these terms for harmonic distortion, assume a single-tone input, $v = \cos(\omega t)$. This elicits the signals

$$\begin{aligned}
x_1 &= g_1|H(j\omega)| \cos(\omega t + \phi(j\omega)) \\
z_1 &= |1 - g_1H(j\omega)| \cos(\omega t + \phi_{z_1}(j\omega)) \\
&= \underbrace{|(s - h_1)H(j\omega)|}_{H_{z_1}(j\omega)} \cos(\omega t + \phi_{z_1}(j\omega))
\end{aligned} \tag{56}$$

Here we have defined $H_{z_1}(s) = (1 - g_1H(s))$. The phases $\phi(s)$ and $\phi_{z_1}(s)$ are the arguments of $H(s)$ and $H_{z_1}(s)$, respectively. The signals x_1 and z_1 are single tones of

frequency ω as well, since they are merely linearly-filtered versions of v .

Raising z_1 and x_1 each to the $(n - 1)^{\text{th}}$ power produces harmonics as follows. If $(n - 1)$ is odd(even), then odd(even) harmonics up to the $(n - 1)^{\text{th}}$ harmonic are generated. The amplitude of the $m\omega$ frequency term in x_1^{n-1} is

$$\frac{(n-1)!g_1}{\frac{n+m-1}{2}!\frac{n-m-1}{2}!2^{n-2}}|H(j\omega)|, \quad (57)$$

while that of the $m\omega$ frequency term in z_1^{n-1} is

$$\frac{(n-1)!}{\frac{n+m-1}{2}!\frac{n-m-1}{2}!2^{n-2}}|H_{z_1}(j\omega)|. \quad (58)$$

After filtering in the ϵ^{n-1} equation, the amplitudes of these terms will be, respectively,

$$\frac{(n-1)!h_{n-1}g_1}{\frac{n+m-1}{2}!\frac{n-m-1}{2}!2^{n-2}}|H(j\omega)||H(jm\omega)|, \quad (59)$$

and

$$\frac{(n-1)!g_{n-1}}{\frac{n+m-1}{2}!\frac{n-m-1}{2}!2^{n-2}}|H_{z_1}(j\omega)||H(jm\omega)|. \quad (60)$$

Analogous to that of the ϵ^{n-1} equation, the input to the ϵ^n equation has terms in z_1^n and x_1^n . In general, the x_2 terms are identically zero, except for the special case $n = 3$.

4.4 Feedback and distortion

We now make some observations about the harmonic distortion results that were discussed in the previous section.

In the ϵ^{n-1} equation, the amplitude of the m^{th} harmonic that the z_1^{n-1} term contributes is given by (60). A plot of this amplitude expression, along with that of (59), is shown as a function of frequency in Fig. 18 for the third-order harmonic generated by a dominantly-third order nonlinearity. That is, $n = 4$ and $m = 3$. The other parameter values are $h_1 = 1$, $h_3 = 1/3$, $g_1 = G$, $g_3 = G/3$, where G was varied from 10 to 1000.

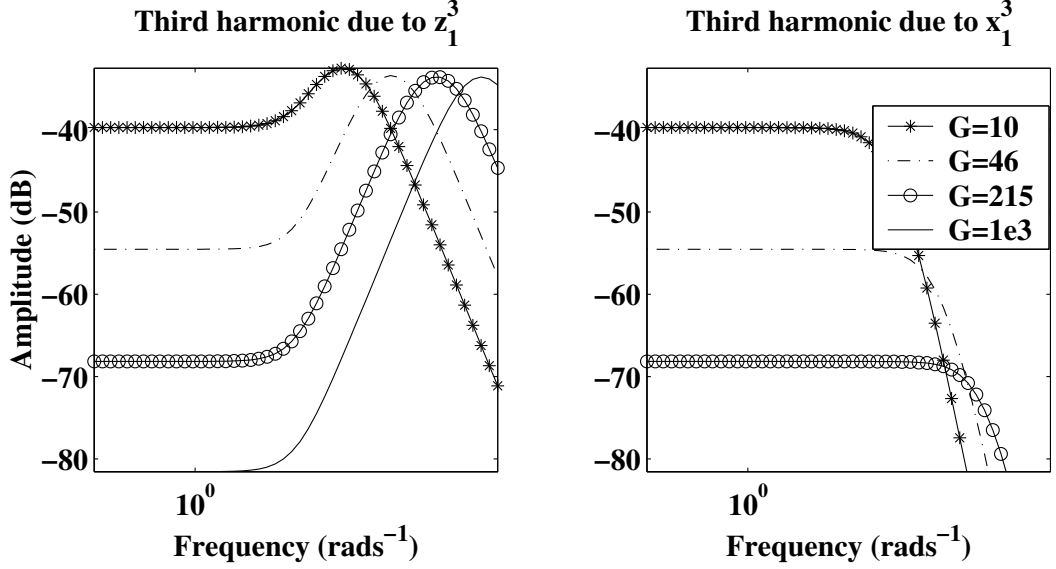


Figure 18. Magnitude-frequency plots of the third harmonic. The ‘gain’, G of the $g(z)$ function is varied from 10 to 1000. This causes the band-pass shape of the z_1^3 -contributed harmonic to shift to the right, while that contributed by x_1^3 falls in magnitude.

Notice from the figure that if $g_1 \gg h_1$, then, for a given frequency, the amplitude of the z_1^{n-1} -contributed harmonic is greatly reduced. In fact, if we ensure $g_i \gg h_i \forall i$, then the harmonic contribution of the x_1^{n-1} terms is negligible. This would mean that the distortion is effectively due only to z_1 , whose associated harmonics are band-pass filtered. This in turn means that the distortion can be kept small if the circuit is operated well below the corner frequency.

These two notions — that frequency and feedback gain can be sacrificed for higher linearity — conform with the traditional rules-of-thumb for low-distortion design.

4.5 Illustrative examples

4.5.1 Source follower amplifier

According to KCL, the circuit equation of the source follower amplifier in Fig. 19 (a) is

$$C \frac{dV_{\text{out}}(t)}{dt} = F(V_{\text{in}}, V_{\text{out}}) - I_{\text{bias}}, \quad (61)$$

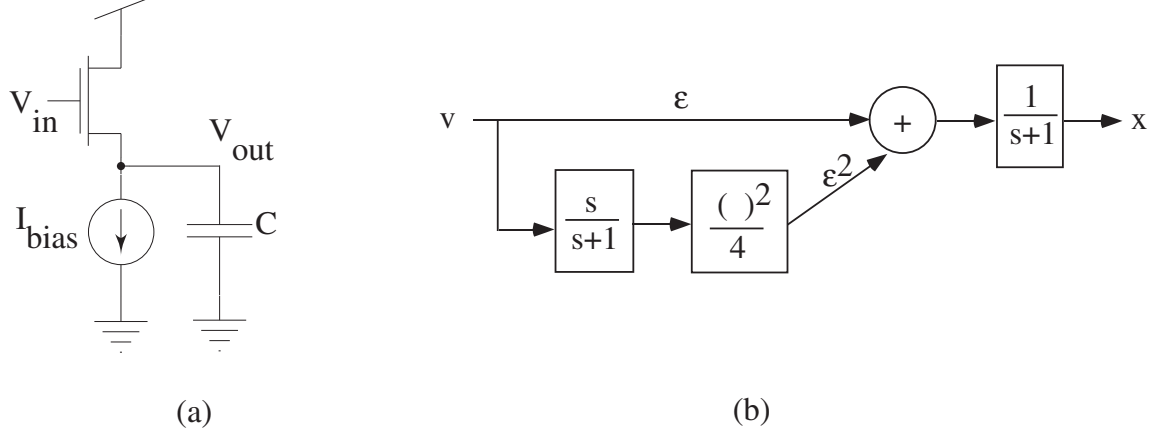


Figure 19. Source follower amplifier. (a) Circuit schematic. (b) Block diagram representation of source follower output. The fundamental harmonic is a low-pass filtered version of the input. The second order terms are generated by high-pass filtering the input, squaring and then low pass filtering. The total output is a power series of ϵ terms.

where the function F is defined as

$$F(V_{\text{in}}, V_{\text{out}}) = \frac{K}{2} (\kappa V_{\text{in}}(t) - V_{\text{out}}(t) - V_{\text{th}})^2, \quad (62)$$

if M_1 is in above-threshold saturation, and

$$F(V_{\text{in}}, V_{\text{out}}) = I_o e^{(\kappa V_{\text{in}}(t) - V_{\text{out}}(t))/U_T}, \quad (63)$$

if it is in subthreshold saturation. The parameter K depends on transistor dimensions and doping and V_{th} is the threshold voltage. Also, I_o is a pre-exponential current that depends on device dimensions and κ , and U_T have their usual meanings from the EKV MOSFET model [11].

Note that $I_{\text{bias}} = F(V_g, V_S)$, where V_g and V_S are the d.c. bias-points of the gate and source of M_1 , respectively. Let us define a *characteristic voltage*, V_c , as

$$V_c = \begin{cases} (\kappa V_g - V_S - V_{\text{th}})/2, & \text{above threshold} \\ U_T, & \text{subthreshold.} \end{cases} \quad (64)$$

Now, (61) can be non-dimensionalized [17] by making the substitutions

$$\tau = I_{\text{bias}}/(CV_c) \cdot t; \quad u = \kappa \nu_{\text{in}}/V_c; \quad x = \nu_{\text{out}}/V_c, \quad (65)$$

where ν_{in} and ν_{out} are the a.c. portions of V_{in} and V_{out} . This gives the state-space equation of the source follower as

$$\frac{dx}{d\tau} = u - x + (u - x)^2/4, \quad (66)$$

for above threshold, and

$$\frac{dx}{d\tau} = u - x + (u - x)^2/2, \quad (67)$$

for the truncated Taylor expansion in subthreshold. The point is that, regardless of region of operation of M_1 , the nonlinear equation that describes the source follower has the same functional form. Relating the source follower equations to (51), we have $g(z) \sim z + z^2$ and $h(x) = 0$. As such, we expect the harmonic distortion terms to have a band-pass-like dependence on frequency. To show this, we can apply regular perturbation to (66).

First, define $u = \epsilon v$, where the small parameter ϵ is a scaled version of the input amplitude. That is, $\epsilon = A_{\text{in}}/V_c$. Also, taking $x = \epsilon x_1 + \epsilon^2 x_2$ and $z = u - x$ and equating like powers of ϵ up to ϵ^2 , we have

$$\epsilon^1 : \dot{x}_1 = v - x_1 \quad (68)$$

$$\epsilon^2 : \dot{x}_2 = z_1^2/4 - x_2 \quad (69)$$

Assume a pure-tone input, $v = \cos(\omega t)$. Equation (68) is the linear portion of the amplifier. Equation (69) is a linear filter with input $z_1^2/4$. The squaring produces a second-harmonic term as well as a d.c. offset. In addition, since $z_1 = v - x_1$, the second-harmonic generated by the squaring is high-pass filtered. The overall effect is that x_2 is a band-pass filtered version of a second harmonic of v . Figure 20 is a plot of experimental data that corroborates the analysis.

4.5.2 Unity-gain buffer

Consider the unity-gain buffer depicted in Fig. 21 (a). It is formed by placing an operational transconductance amplifier (OTA) in negative feedback. If we operate

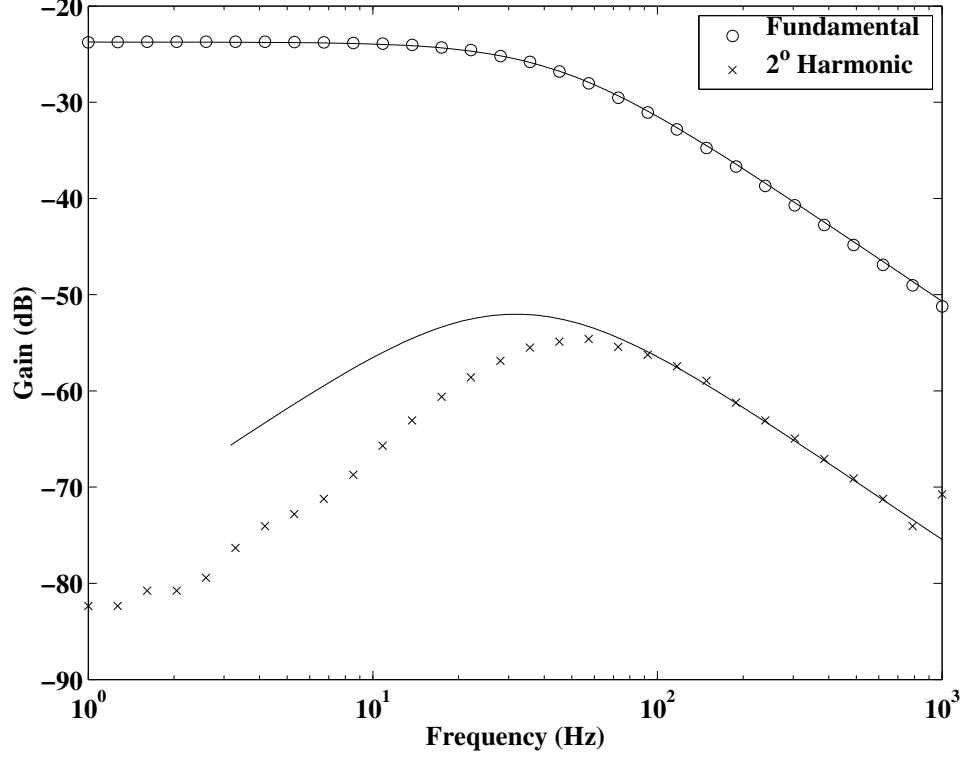


Figure 20. Magnitude-frequency response of source follower. Analytical prediction is in bold, and experimental data is plotted as ‘x’s and ‘o’s. The fundamental harmonic is a low-pass filtered version of the input. The second harmonic has a bandpass shape, as predicted by perturbation analysis.

the OTA above threshold, the describing equation is

$$C \frac{dV_{\text{out}}}{dt} = \sqrt{\kappa \beta I_{\text{bias}}} V_{\text{in}} \sqrt{1 - \frac{\kappa \beta V_{\text{in}}^2}{4I_{\text{bias}}}}, \quad (70)$$

while it is

$$C \frac{dV_{\text{out}}}{dt} = I_{\text{bias}} \tanh\left(\frac{\kappa V_{\text{in}}}{2U_{\text{T}}}\right), \quad (71)$$

for subthreshold operation. Notice that we have ignored the output conductance term, which is considered very small for OTAs.

We can define a characteristic voltage, V_c , as

$$V_c = \begin{cases} \frac{2U_{\text{T}}}{\kappa}, & \text{subthreshold} \\ \sqrt{\frac{I_{\text{bias}}}{\kappa \beta}}, & \text{above threshold.} \end{cases} \quad (72)$$

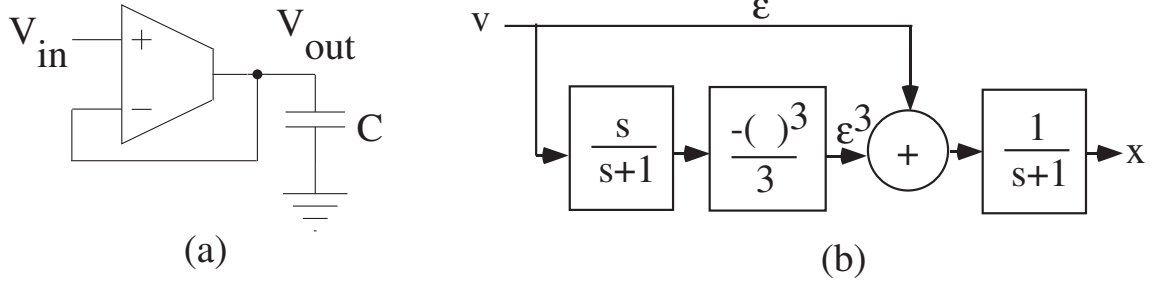


Figure 21. Unity gain buffer. (a) Circuit schematic. (b) Block diagram representation of output. The fundamental harmonic is a low-pass filtered version of the input. The third-order terms are generated by high-pass filtering the input, cubing and then low pass filtering. The total output is a power series of ϵ terms.

Then, with the following definitions

$$\tau = I_{\text{bias}}/(CV_c) \cdot t; \quad u = v_{\text{in}}/V_c; \quad x = v_{\text{out}}/V_c, \quad (73)$$

the nondimensional form of the unity-gain buffer's describing equations (taken to the first few Taylor series terms) is

$$\frac{dx}{d\tau} = \begin{cases} (u - x) - (u - x)^3/4, & \text{above threshold} \\ (u - x) - (u - x)^3/3, & \text{subthreshold.} \end{cases} \quad (74)$$

Again, the functional form of the equations is identical, regardless of region of operation.

To calculate distortion terms, assume $u = \epsilon v$ is a pure-tone signal and proceed as usual. For subthreshold, the separated equations of ϵ are

$$\epsilon^1 : \dot{x}_1 = v - x_1 \quad (75)$$

$$\epsilon^2 : \dot{x}_2 = 0 - x_2 \quad (76)$$

$$\epsilon^3 : \dot{x}_3 = z_1^3/3 - x_3. \quad (77)$$

Equation (75) is the linear portion of the amplifier. Equation (76) is a linear filter with 0 input; it contributes no harmonics at steady state. Equation (77) is a linear filter

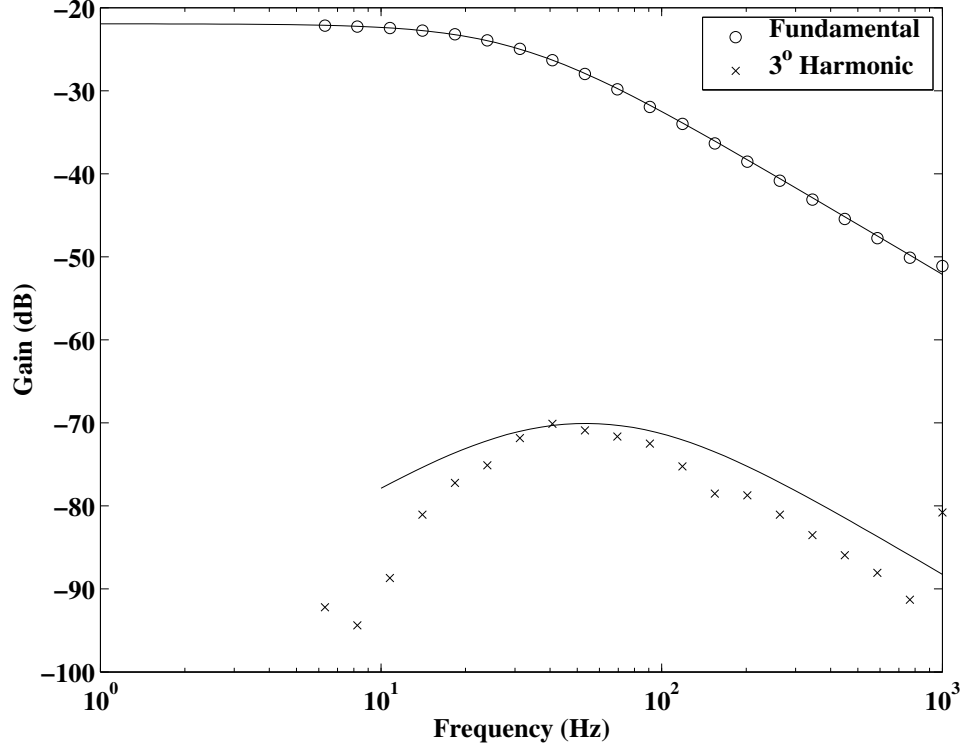


Figure 22. Magnitude-frequency response of unity-gain buffer. Analytical prediction is in bold, and experimental data is plotted as ‘x’s and ‘o’s. The fundamental harmonic is a low-pass filtered version of the input. The third harmonic has a bandpass shape, as predicted by perturbation analysis.

with input $z_1^3/3$. The cubing produces a third-harmonic term as well as a fundamental-frequency term (this fundamental-frequency term will cause gain compression, which is not discussed in this chapter). Since $z_1 = v - x_1$, the overall effect is that x_3 is a band-pass filtered version of a third harmonic of v , as shown in Fig. 22.

4.5.3 Note on above-threshold versus subthreshold operation

The harmonic behavior of a circuit is similar for above- and subthreshold operation. In absolute numbers, however, above threshold operation yields less distortion. This is because the parameter $\epsilon = A_{in}/V_c$ is much smaller for above threshold than for subthreshold. Since the harmonics are multiplied by ϵ^i , the smaller ϵ seen in above threshold operation translates to lower distortion.

CHAPTER 5

NONHOMOGENEOUS SYSTEMS II: SECOND-ORDER CIRCUITS

In this chapter, we consider second-order filters, which are nonhomogeneous two-dimensional systems. The methods of regular perturbation do not always extend to two dimensions and higher.

Consider for example the homogeneous system described by

$$\ddot{y} + y + 2\epsilon\dot{y} = 0, \quad (78)$$

with initial conditions $y(0) = 0$, $\dot{y}(0) = 1$, and where $\epsilon > 0$ is a small perturbation parameter.

Note that we can solve (78) as a linear ordinary differential equation to get

$$y(t) = \frac{e^{-\epsilon t}}{\sqrt{1 - \epsilon^2}} \sin\left(\sqrt{1 - \epsilon^2} t\right) \quad (79)$$

If we attempted to solve (78) via regular perturbation, we would apply the usual substitution

$$y(t) = y_0(t) + \epsilon y_1(t) + O(\epsilon^2). \quad (80)$$

Equating like powers of ϵ , (78) yields, to $O(\epsilon)$,

$$\epsilon^0 : \ddot{y}_0 + y_0 = 0 \quad (81)$$

$$y_0(0) = 0; \quad \dot{y}_0(0) = 1, \quad (82)$$

and

$$\epsilon : \ddot{y}_1 + y_1 = -2\dot{y}_0 \quad (83)$$

$$y_1(0) = 0; \quad \dot{y}_1(0) = 0. \quad (84)$$

The solution to (82) is $y_0(t) = \sin(t)$ and the solution to (84) is $y_1(t) = -t \sin(t)$, giving an approximate solution to (78) of

$$y(t) = (1 - \epsilon t) \sin(t). \quad (85)$$

Comparing (79) to (85), we see that the regular perturbation method predicts the wrong amount of damping and also the wrong frequency. The problem here is that there are two timescales at which the system is operating: that related to the resonant frequency and that of the transient decay.

The phenomenon of two timescales is also observed for filters with high quality-factor (Q). Regular perturbation fails to account for the two timescales and methods of singular perturbation instead are needed.

5.1 Two-timescale analysis

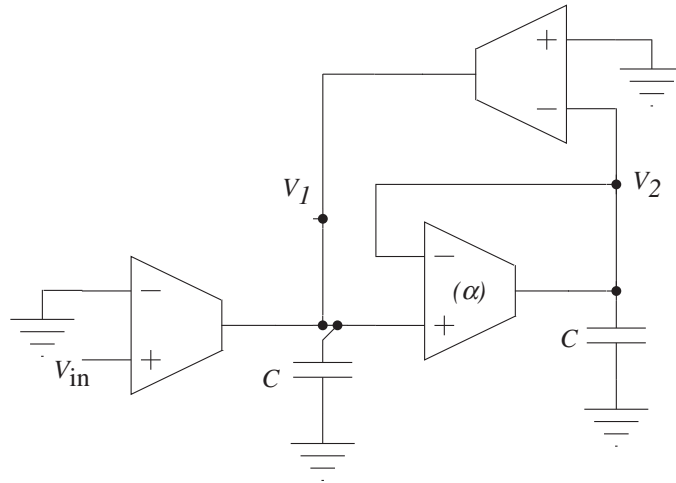


Figure 23. Second order section for singular perturbation analysis. The OTA labeled (α) is understood to be linearized. Assuming the nonlinear OTAs have tanh transconductance functions, this circuit implements the system of (87). The system is in effect a high quality factor filter, which necessitates the use of singular perturbation methods for its analysis.

The circuit in Fig. 23 is a second-order low-pass filter. According to KCL, the dynamics are as follows

$$\begin{aligned} C \frac{dV_2}{dt} &= f_1(V_1 - V_2) \\ C \frac{dV_1}{dt} &= f_2(V_{in}) - f_3(V_2), \end{aligned} \quad (86)$$

where $f_{1,2,3}$ are the transconductance functions of the OTAs. For subthreshold operation, these functions are nominally hyperbolic tangents. As we shall see in later

chapters on design, it is also possible to linearize the transconductance functions. Assuming that the OTA labelled (α) in Fig. 23 is linearized, and replacing $F_{1,2}$ with tanh functions, we can write

$$\begin{aligned} C \frac{dV_2}{dt} &= GV_1 - GV_2 \\ C \frac{dV_1}{dt} &= I_2 \tanh\left(\frac{\kappa V_{\text{in}}}{2U_T}\right) - I_3 \tanh\left(\frac{\kappa V_2}{2U_T}\right), \end{aligned} \quad (87)$$

where G is the linearized transconductance gain of O_1 and I_2 and I_3 are the bias currents of OTAs O_2 and O_3 , respectively.

Defining

$$\begin{aligned} y_1 &= \frac{\kappa V_1}{2U_T}, & y_2 &= \frac{\kappa V_2}{2U_T}, \\ v &= \frac{\kappa V_{\text{in}}}{2U_T}, & T &= \frac{t\kappa I_2}{2CU_T}, \end{aligned} \quad (88)$$

(87) becomes

$$\begin{aligned} \frac{dy_2}{dT} &= \frac{2GU_T}{\kappa I_2}(y_1 - y_2) \\ \frac{dy_1}{dT} &= \tanh(v) - \frac{I_3}{I_2} \tanh(y_2) \end{aligned} \quad (89)$$

As a single second-order equation, the filter is

$$\begin{aligned} \frac{d^2 y_2}{dT^2} + \frac{2GU_T}{\kappa I_2} \frac{dy_2}{dT} + \frac{2GU_T I_3}{\kappa I_2^2} \tanh(y_2) &= \frac{2GU_T}{\kappa I_2} \tanh(v) \\ \frac{2GU_T I_3}{\kappa I_2^2} \frac{d^2 y_2}{dT^2} + \frac{I_2}{I_3} \frac{dy_2}{dT} + \tanh(y_2) &= \frac{I_2}{I_3} \tanh(v) \\ \tau^2 \frac{d^2 y_2}{dT^2} + \epsilon \frac{dy_2}{dT} + \tanh(y_2) &= \epsilon \tanh(v), \end{aligned} \quad (90)$$

where we have defined $\tau^2 = 2GU_T I_3 / (\kappa I_2^2)$ and $\epsilon = I_2 / I_3$. For a high-Q filter, ϵ is a small parameter. Let us say that the input, and hence the output, are small in magnitude. We represent this by the substitutions $x\epsilon^{2/3}/3 = y_2$ and $v\epsilon^{2/3}/3 = u^1$ and expanding the tanh functions to the third term, which gives

$$\tau^2 \frac{d^2 x}{dT^2} + \epsilon \frac{dx}{dT} + x - \epsilon x^3 = \epsilon(u - \epsilon u^3). \quad (91)$$

¹Raising ϵ to the 2/3 power simplifies the subsequent math, but does not detract from the basic assumption that y_2 and u are both small-valued.

For ease of analysis, we normalize the center frequency via $\tau = 1$. Also, we will analyze the response to the pure tone input $u = F \cos(\omega T)$. The system simplifies to

$$\frac{d^2x}{dT^2} + \epsilon \frac{dx}{dT} + x - \epsilon x^3 = \epsilon(F \cos(\omega T) - \epsilon F^3 \cos^3(\omega T)). \quad (92)$$

We will represent the two timescales that are associated with this filter as

$$\begin{aligned} \xi &= \omega t, \\ \eta &= \epsilon t, \end{aligned} \quad (93)$$

where ξ is the fast timescale related to the center frequency and η is the timescale of the slow transient. If the solution, x , is regarded as a function of ξ and η , then we can write

$$\begin{aligned} \frac{dx}{dt} &= \frac{\partial x}{\partial \xi} \frac{d\xi}{dt} + \frac{\partial x}{\partial \eta} \frac{d\eta}{dt} \\ &= \omega \frac{\partial x}{\partial \xi} + \epsilon \frac{\partial x}{\partial \eta}. \end{aligned} \quad (94)$$

Substituting this into (92) gives

$$\omega^2 \frac{\partial^2 x}{\partial \xi^2} + 2\omega\epsilon \frac{\partial^2 x}{\partial \xi \partial \eta} + \epsilon^2 \frac{\partial^2 x}{\partial \eta^2} + \epsilon\omega \frac{\partial x}{\partial \xi} + \epsilon^2 \frac{\partial x}{\partial \eta} + x - \epsilon x^3 = \epsilon(F \cos(\xi) - \epsilon F^3 \cos^3(\xi)). \quad (95)$$

We expand x and ω as power series in ϵ

$$x(\xi, \eta) = x_0(\xi, \eta) + \epsilon x_1(\xi, \eta) + \epsilon^2 x_2(\xi, \eta) + \dots \quad (96)$$

$$\omega(\xi, \eta) = 1 + k_1\epsilon + k_2\epsilon^2 + \dots, \quad (97)$$

substitute into (95) and collect terms in ϵ to get

$$\epsilon^0 : \frac{d^2 x_0}{d\xi^2} + x_0 = 0 \quad (98)$$

$$\epsilon^1 : \frac{d^2 x_1}{d\xi^2} + x_1 = F \cos(\xi) + x_0^3 - \frac{dx_0}{d\xi} - 2k_1 \frac{d^2 x_0}{d\xi^2} - 2 \frac{d^2 x_0}{d\xi d\eta}, \quad (99)$$

where we have ignored terms in ϵ^2 and higher.

The solution to (98) is $x_0(\xi) = A_0(\eta) \cos(\xi) + B_0(\eta) \sin(\xi)$, where $A_0(\eta)$ and $B_0(\eta)$ are slowly-varying functions of time. Substituting the solution of (98) into (99) gives

$$\begin{aligned}
\frac{d^2 x_1}{d\xi^2} + x_1 &= F \cos(\xi) + 1/4 A_0(\eta)^3 \cos(3\xi) + 3/4 A_0(\eta)^3 \cos(\xi) \\
&+ 3/4 A_0(\eta)^2 B_0(\eta) \sin(3\xi) + 3/4 A_0(\eta)^2 B_0(\eta) \sin(\xi) \\
&+ 3/4 A_0(\eta) B_0(\eta)^2 \cos(\xi) - 3/4 A_0(\eta) B_0(\eta)^2 \cos(3\xi) \\
&- 1/4 B_0(\eta)^3 \sin(3\xi) + 3/4 B_0(\eta)^3 \sin(\xi) + A_0(\eta) \sin(\xi) \\
&- B_0(\eta) \cos(\xi) + 2k_1 A_0(\eta) \cos(\xi) + 2k_1 B_0(\eta) \sin(\xi) \\
&+ 2 \frac{dA_0(\eta)}{d\eta} \sin(\xi) - 2 \frac{dB_0(\eta)}{d\eta} \cos(\xi). \tag{100}
\end{aligned}$$

The RHS of (100) has terms in $\cos(\xi)$ and $\sin(\xi)$. In general, the presence of these *secular* terms would imply that the solution x_1 grows as a function of ξ . Since such a result is inconsistent with our expectations (the system is after all merely a perturbation of a stable linear filter), we equate all of the secular terms to zero, to get

$$\frac{dB_0(\eta)}{d\eta} = F/2 + 3/8 A_0(\eta)^3 + 3/8 A_0(\eta) B_0(\eta)^2 - B_0(\eta)/2 + k_1 A_0(\eta), \tag{101}$$

$$\frac{dA_0(\eta)}{d\eta} = -3/8 B_0(\eta)^3 - 3/8 A_0(\eta)^2 B_0(\eta) - A_0(\eta)/2 - k_1 B_0(\eta). \tag{102}$$

The equilibrium point of (101) and (102) represents the fixed amplitude of the sinusoid that x_0 will eventually tend to. Denoting the equilibrium point as (A_0^*, B_0^*) , we can write

$$0 = F/2 + 3/8 A_0^{*3} + 3/8 A_0^* B_0^{*2} - B_0^*/2 + k_1 A_0^*, \tag{103}$$

$$0 = -3/8 B_0^{*3} - 3/8 A_0^{*2} B_0^* - A_0^*/2 - k_1 B_0^*. \tag{104}$$

Next, we define the output amplitude as $R_0 = \sqrt{A_0^{*2} + B_0^{*2}}$ and solve (103) and (104) for k_1 to get

$$k_1 = \frac{-3R_0^{*3} \pm 4\sqrt{F^2 - R_0^{*2}}}{8R_0^*}. \tag{105}$$

To first order, the relation between input frequency, input amplitude and output amplitude, in the vicinity of the center frequency, is

$$\omega \approx 1 + \frac{3}{8}\epsilon R_0^{*2} \pm \frac{1}{2}\epsilon \sqrt{\frac{F^2}{R_0^{*2}} - 1}. \quad (106)$$

5.2 Averaging

The method of averaging presents an alternative way to analyze systems of the form

$$\ddot{x} + x = \epsilon h_1(\dot{x}, x, t) + \epsilon^2 h_2(\dot{x}, x, t) + \text{O}(\epsilon^3) \quad (107)$$

without having to explicitly account for different timescales. We can rearrange (92) in the form of (107) as

$$\frac{d^2x}{dT^2} + x = \epsilon \left(F \cos(\omega T) - \frac{dx}{dT} + x^3 \right) - \epsilon^2 F^3 \cos^3(\omega T). \quad (108)$$

Assume that the solution to (108) is

$$x(T) = R(T) \cos(T + \psi(T)). \quad (109)$$

The argument for picking such a form for the solution is that, if $\epsilon = 0$, then the solution to (108) is exactly (109), with $R(T)$ and $\psi(T)$ constant. If ϵ is small and non-zero, then we can expect $R(T)$ and $\psi(T)$ to be slowly-varying functions of time.

An effect of defining the solution as (109) is that there are now three variables, but only two equations. To constrain the problem, we can add a third equation of our choosing, such as

$$\frac{dx}{dT} = -R(T) \sin(T + \psi(T)). \quad (110)$$

Equating the derivative of (109) to (110), we find that

$$\frac{dR}{dT} \cos(T + \psi) = R \frac{d\psi}{dT} \sin(T + \psi), \quad (111)$$

must hold. Notice that (111) is a differential equation that is purely in terms of $R(T)$ and $\psi(T)$, and does not contain any terms in $x(T)$. We can find a second equation

in $R(T)$ and $\psi(T)$ by taking the derivative of (110),

$$\frac{d^2x}{dT^2} = -\frac{dR}{dT} \sin(T + \psi) + \left(1 + \frac{d\psi}{dT}\right) R \cos(T + \psi), \quad (112)$$

and substituting (109), (110) and (112) into (108). This gives

$$-\frac{dR}{dT} \sin(T + \psi) - \frac{d\psi}{dt} R \cos(T + \psi) = \epsilon (F \cos(T) + R^3 \cos(T + \psi))^3 + R \sin(T + \psi) - \epsilon^2 F^3 \cos(T)^3. \quad (113)$$

From (111) and (113), the differential equations that describe $R(T)$ and $\psi(T)$ are

$$\begin{aligned} \frac{dR}{dT} = & \epsilon (\sin(T + \psi))(-F \cos(T) + R^3 \cos(T + \psi) \sin(T + \psi)^2 + \\ & -R^3 \cos(T + \psi) - R \sin(T + \psi)) + O(\epsilon^2), \end{aligned} \quad (114)$$

$$\begin{aligned} \frac{d\psi}{dT} = & \frac{\epsilon}{R} (-R^3 \sin(T + \psi)^4 + 2R^3 \sin(T + \psi)^2 - R^3 + \\ & -\cos(T + \psi)F \cos(T) - \cos(T + \psi)R \sin(T + \psi)) + O(\epsilon^2). \end{aligned} \quad (115)$$

The conversion of the problem from (108) to (114) and (115) is exact and it is referred to as variation of parameters. To proceed with the solution, consider the following near-identity transformations, where R and ψ are written as power series in ϵ [20]

$$R = \bar{R} + \epsilon w_1(\bar{R}, \bar{\psi}, T) + \epsilon^2 v_1(\bar{R}, \bar{\psi}, T) + \dots, \quad (116)$$

$$\psi = \bar{\psi} + \epsilon w_2(\bar{R}, \bar{\psi}, T) + \epsilon^2 v_2(\bar{R}, \bar{\psi}, T) + \dots. \quad (117)$$

The functions w_i and v_i are called generating functions. They are chosen such that the transformed equations on \bar{R} and $\bar{\psi}$ (that is, the differential equations of \bar{R} and $\bar{\psi}$) are as simple as possible. Substituting (116) and (117) into (114) and (115),

the differential equations of \bar{R} and $\bar{\psi}$ are

$$\begin{aligned} \frac{d\bar{R}}{dT} = & \epsilon \left(\sin(T + \bar{\psi})(-F \cos(T) + \bar{R}^3 \cos(T + \bar{\psi}) \sin(T + \bar{\psi})^2 - \frac{\partial w_1}{\partial T} + \right. \\ & \left. - \frac{\partial w_1}{\partial \bar{R}} \frac{d\bar{R}}{dT} - \frac{\partial w_1}{\partial \bar{\psi}} \frac{d\bar{\psi}}{dT} - \bar{R}^3 \cos(T + \bar{\psi}) - \bar{R} \sin(T + \bar{\psi})) \right), \end{aligned} \quad (118)$$

$$\begin{aligned} \frac{d\bar{\psi}}{dT} = & \frac{\epsilon}{\bar{R}} \left(-\bar{R}^3 \sin(T + \bar{\psi})^4 + 2\bar{R}^3 \sin(T + \bar{\psi})^2 - \bar{R}^3 - \frac{\partial w_2}{\partial T} - \frac{\partial w_2}{\partial \bar{R}} \frac{d\bar{R}}{dT} + \right. \\ & \left. - \frac{\partial w_2}{\partial \bar{\psi}} \frac{d\bar{\psi}}{dT} - \cos(T + \bar{\psi})F \cos(T) - \cos(T + \bar{\psi})\bar{R} \sin(T + \bar{\psi}) \right), \end{aligned} \quad (119)$$

where $O(\epsilon^2)$ and higher terms have been ignored. The functions w_1 and w_2 can be chosen such that only the average values of the $O(\epsilon)$ terms of (118) and (119) remain.

That is, (118) and (119) become

$$\begin{aligned} \frac{d\bar{R}}{dT} = & \frac{\epsilon}{T_p} \int_0^{T_p} \sin(T + \bar{\psi})(-F \cos(T) + \bar{R}^3 \cos(T + \bar{\psi}) \sin(T + \bar{\psi})^2 + \\ & - \bar{R}^3 \cos(T + \bar{\psi}) - \bar{R} \sin(T + \bar{\psi}))dT, \end{aligned} \quad (120)$$

$$\begin{aligned} \frac{d\bar{\psi}}{dT} = & \frac{\epsilon}{T_p \bar{R}} \int_0^{T_p} -\bar{R}^3 \sin(T + \bar{\psi})^4 + 2\bar{R}^3 \sin(T + \bar{\psi})^2 - \bar{R}^3 + \\ & - \cos(T + \bar{\psi})F \cos(T) - \cos(T + \bar{\psi})\bar{R} \sin(T + \bar{\psi}))dT, \end{aligned} \quad (121)$$

where T_p is the length of one period of the input signal. The integrals on the RHS of (120) and (121) are *partial integrals*, in the sense that \bar{R} and $\bar{\psi}$ are held constant during the integration. Evaluating (120) and (121) for $T_p = 2\pi$ — that is, at the filter's resonant frequency — we get

$$\frac{d\bar{R}}{dT} = -\frac{F}{2} \sin(\bar{\psi}) - \frac{\bar{R}}{2} \quad (122)$$

$$\frac{d\bar{\psi}}{dT} = -\frac{F}{2\bar{R}} \cos(\bar{\psi}) - \frac{3}{8}\bar{R}^2, \quad (123)$$

which are called the slow flow equations. The solution of the slow flow equations would reveal how the amplitude and phase of $y(T)$ evolve over time. The equilibrium point of the slow flow equations represents the steady state of $y(T)$. The equilibrium

point is derived by setting the RHS of the slow flow equations to zero such that

$$\frac{F}{2} \sin(\bar{\psi}) = -\frac{\bar{R}}{2} \quad (124)$$

$$\frac{F}{2\bar{R}} \cos(\bar{\psi}) = -\frac{3}{8}\bar{R}^2. \quad (125)$$

Squaring (124) and adding it to the square of (125), we find, with the trigonometric identity $\cos(\bar{\psi})^2 + \sin(\bar{\psi})^2 = 1$, that the value of \bar{R} at the equilibrium point must satisfy

$$F^2 = \bar{R}^2 + \frac{9}{16}\bar{R}^6, \quad (126)$$

the solution to which is

$$\bar{R}^* = \frac{2\sqrt{2}}{3} \sqrt{\sqrt{1 + \frac{9}{4}F^2} - 1}. \quad (127)$$

Notice that this expression for the steady state amplitude is equivalent to what we would have derived by evaluating the two timescale solution at the filter's resonant frequency (that is, by setting $k_1 = 0$ in (105) and solving for \bar{R}_0^*).

CHAPTER 6

THEORY AND DESIGN OF OTA-C OSCILLATORS WITH NATIVE AMPLITUDE LIMITING

The sinusoidal oscillator is a basic analog circuit component in communication and instrumentation systems. High quality oscillators usually involve inductor-capacitor networks, and are used in RF systems. However, the inductance values required for low- and moderate frequency oscillators cannot practically be realized in integrated circuits. Ring-oscillators provide much better economy in terms of size, but they are limited to such uses as clock generation, due to their high harmonic content. Operational transconductance amplifier-capacitor (OTA-C) oscillators, on the other hand, operate at low- to moderate frequencies with fairly high spectral purity, and are compact enough for integration.

An OTA-C oscillator is typically designed as an unstable second-order system that is regulated by some nonlinear, amplitude-limiting circuitry. Buonomo *et al.* identified a set of conditions on the nonlinearity for the system to exhibit oscillation [22]. The most common implementations of an amplitude limiter are a piecewise-linear (pwl) resistor and an automatic gain control circuit [22–25]. A third possibility is to use the inherent nonlinear behavior of an OTA as an amplitude-limiter [26].

The success of using OTA nonlinearity, as reported in the literature, has been mixed. This approach is considered in [24], but the results are only poorly-controlled, distorted oscillations. The approach is also mentioned in [23], but is characterized as yielding only unpredictable oscillations. On the other hand, the results in [27–29] show success in designing sinusoidal oscillators based on OTA nonlinearity. However, none of these papers, nor, to my knowledge, any other sources in the literature, provide a systematic and analytical presentation of how exactly to exploit OTA nonlinearity in a general second-order oscillator structure. This is a relevant lack, as an oscillator that

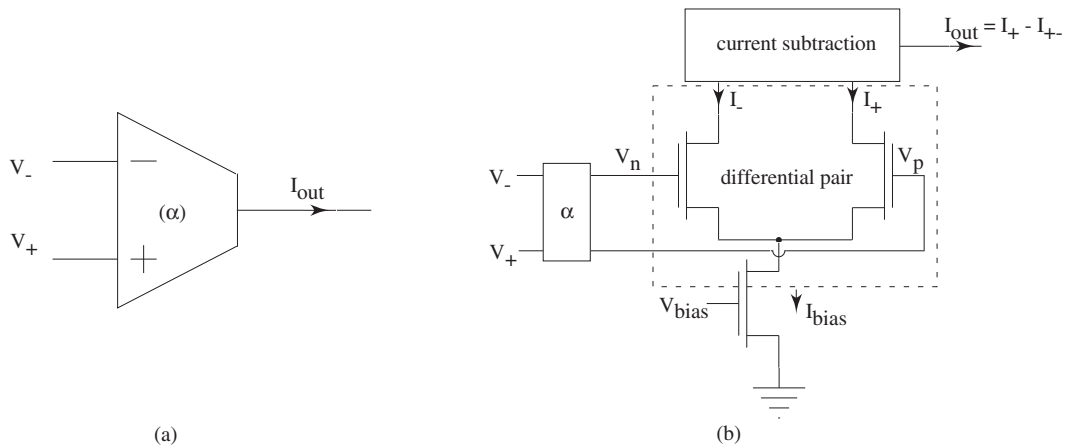


Figure 24. Generic OTA (a) circuit symbol and (b) circuit schematic. The OTA converts a differential voltage input into an output current. A differential pair of transistors is at the heart of the voltage-current conversion. An attenuating stage may exist between the voltage input and the differential pair. A current-subtraction network combines the drain currents of the differential pair transistors into a single output.

properly exploits OTA nonlinearity can easily confer power and area savings since no external amplitude limiting scheme is required. For instance, a slight redesign of the oscillator in [23] could have used one of the existing OTAs as an amplitude limiter, precluding the need for the extra pwl circuit that its authors describe.

This chapter provides a rigorous, generalized, method for exploiting OTA nonlinearity in oscillator design.

6.1 Operational transconductance amplifier basics

6.1.1 Output current

Figure 24 is a block diagram representation of an OTA. The differential input, $V_{in} = V_+ - V_-$, is applied to an attenuating stage. The output of the attenuating stage is fed into the gate voltages of a differential pair, which is normally in saturation. A current subtraction network generates the difference of the differential pair's drain currents, $I_{out} = I_+ - I_-$. The OTA thus provides a *transconductance* function from V_{in} to I_{out} . If the differential pair is biased in the subthreshold region, then the voltage-current

function is [14]

$$I_{\text{out}} = I_{\text{bias}} \tanh \left(\frac{\kappa \alpha V_{\text{in}}}{2U_{\text{T}}} \right), \quad (128)$$

where κ is the body-effect coefficient and U_{T} is the thermal voltage [11]. Also, I_{bias} is a tunable bias current, and α is the gain of the attenuating stage. If the differential pair is biased above threshold, then using the transistor model of [11], the OTA's voltage-current function can be found to be

$$I_{\text{out}} = \alpha \sqrt{\kappa \beta I_{\text{bias}}} V_{\text{in}} \sqrt{1 - \frac{\kappa \beta \alpha^2 V_{\text{in}}^2}{4I_{\text{bias}}}}, \quad (129)$$

where β is a physical constant that is related to the differential pair's geometry and to doping concentrations. Again, I_{bias} is a tunable bias current, and α is the gain of the attenuating stage.

If we define a characteristic voltage, V_{c} as

$$V_{\text{c}} = \begin{cases} \frac{2U_{\text{T}}}{\kappa}, & \text{subthreshold} \\ \sqrt{\frac{I_{\text{bias}}}{\kappa \beta}}, & \text{above threshold,} \end{cases} \quad (130)$$

and the transconductance gain as $G_{\text{m}} = \alpha I_{\text{bias}} / V_{\text{c}}$, then we can write (128) and (129) as

$$I_{\text{out}} = \frac{G_{\text{m}} V_{\text{c}}}{\alpha} \cdot H \left(\frac{\alpha V_{\text{in}}}{V_{\text{c}}} \right), \quad (131)$$

where $H(\cdot)$ is a sigmoidal function that depends on the region of operation. In general, it would also depend on the specific OTA topology. Equation (131) is generic enough to describe any OTA with a saturating transfer curve, regardless of specific topology or of region of operation. V_{c} can be chosen to be any appropriate voltage. We choose V_{c} such that the coefficient of the Taylor series linear term of $H(\cdot)$ is normalized to one.

6.1.2 Linear versus nonlinear OTAs

In this dissertation, we regard some OTAs as linear elements and others as nonlinear ones. This subsection clarifies what the distinction is. Consider the Maclaurin-series expansion of the OTA output current I_{out} .

$$I_{\text{out}} = \frac{G_m V_c}{\alpha} \underbrace{\left(\frac{\alpha V_{\text{in}}}{V_c} + \sum_{i=2}^{\infty} \frac{H^{(i)}(0)}{i!} \left(\frac{\alpha V_{\text{in}}}{V_c} \right)^i \right)}_{H(z)}. \quad (132)$$

The small-signal transconductance gain is the linear term coefficient, denoted G_m in the above equations. An OTA is considered linear if, for the region of operation of V_{in} , its output current can be reasonably modeled — as appropriate to the application in question — as $I_{\text{out}} = G_m V_{\text{in}}$. For the nonlinear terms to be negligible, their coefficients must be sufficiently small. This can be achieved by making α small enough.

For larger values of α , the nonlinear terms in (132) become comparatively significant to the linear term and the OTA is considered nonlinear. Assume that a nonlinear OTA has a value of $\alpha = 1$. Figure 25 compares the output current of a nonlinear OTA ($\alpha = 1$) to that of a linear one ($\alpha = 0.1$).

6.2 Motivation for using OTA as an amplitude limiter

Oscillator circuits are typically based on implementing Liénard's equation,

$$\ddot{z} + f(z)\dot{z} + \gamma(z) = 0. \quad (133)$$

If $f(z)$ and $\gamma(z)$ satisfy the Liénard's Theorem conditions, then the circuit will have a unique, stable oscillation [30]. Notice that the theorem does not guarantee an oscillation that is sinusoidal, or even near-sinusoidal. For (133) to be relevant to a discussion of sinusoidal oscillators, where phase noise is low, $\gamma(z)$ must be linear. The damping term, however, is nonlinear. In practice, it can be obtained by taking the derivative of a nonlinear negative resistor, whose transfer function is depicted in Fig. 26 (a).

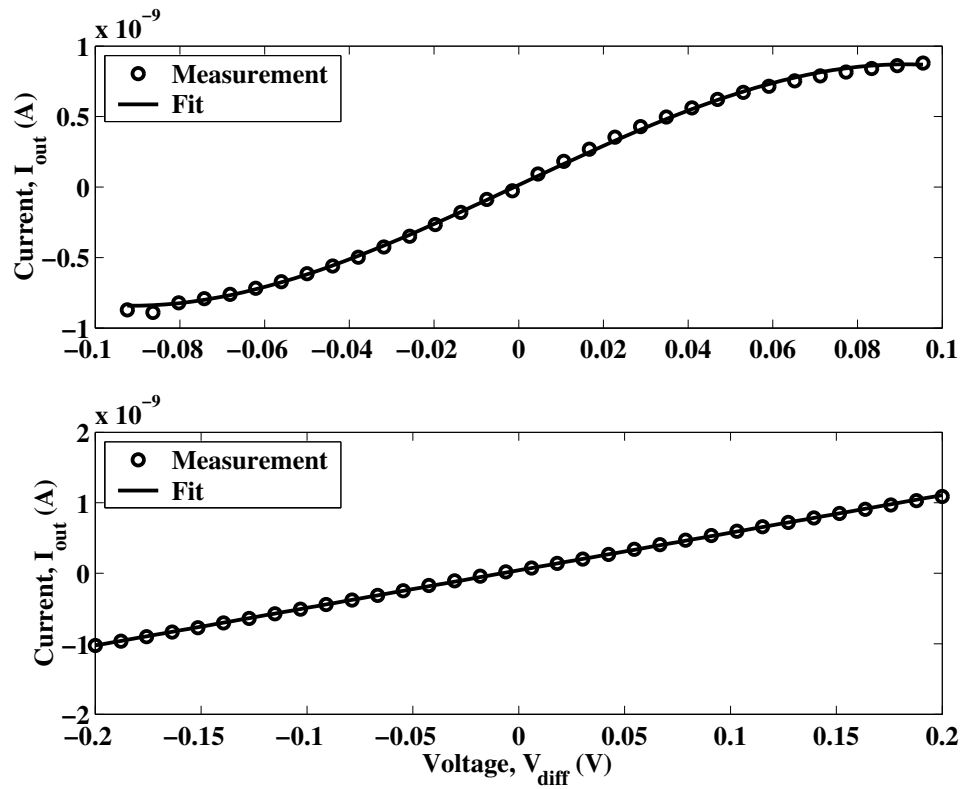


Figure 25. The upper panel shows experimental measurements from a nonlinear OTA. In the lower panel, the nonlinear terms are suppressed enough for a straight line to be an accurate approximation over a 400mV range.

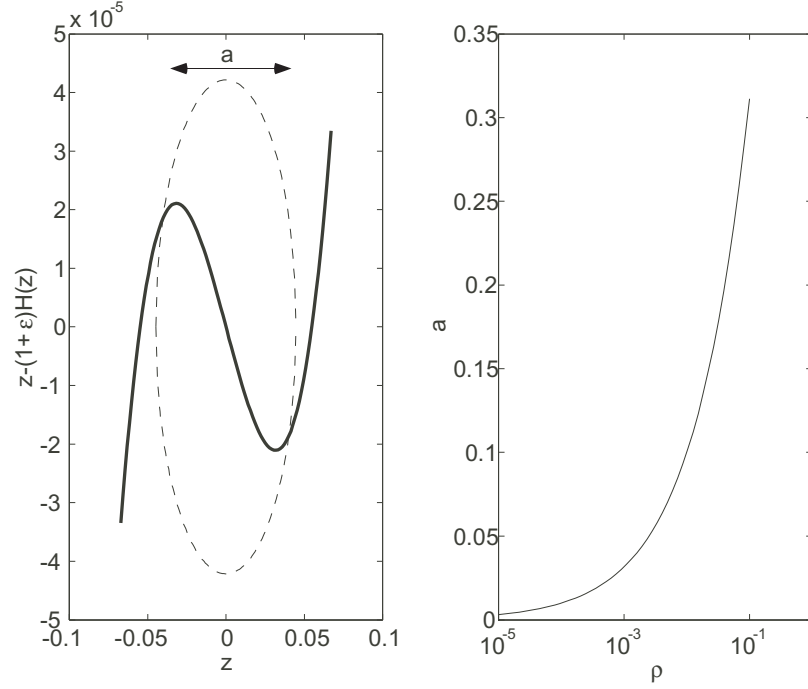


Figure 26. (a) Nonlinear function and region of oscillation and (b) region of oscillation dependence on ρ .

It is fairly straightforward to synthesize the nonlinear resistor with a pair of OTAs, one linear and the other nonlinear. Consider the OTAs in Fig. 27. Assuming that the amplifier that is in the positive-feedback configuration has an attenuation factor of 1 and that the one in the negative-feedback configuration has an attenuation factor of α , we can write the total output current as

$$I_{\text{out}} = \frac{G_{\text{mL}}V_{\text{cL}}}{\alpha} \cdot H\left(\frac{\alpha V_z}{V_{\text{cL}}}\right) - G_{\text{m}}V_{\text{c}} \cdot H\left(\frac{V_z}{V_{\text{c}}}\right), \quad (134)$$

If $\alpha \ll 1$, then the negative-feedback OTA is effectively linear, in which case I_{out} is approximately

$$I_{\text{out}} \approx G_{\text{mL}}V_z - G_{\text{m}}V_{\text{c}} \cdot H\left(\frac{V_z}{V_{\text{c}}}\right). \quad (135)$$

Now, imagine that the transconductance gain of the nonlinear OTA is slightly larger than that of the linear one. That is,

$$G_{\text{m}} = (1 + \rho)G_{\text{mL}}, \quad (136)$$

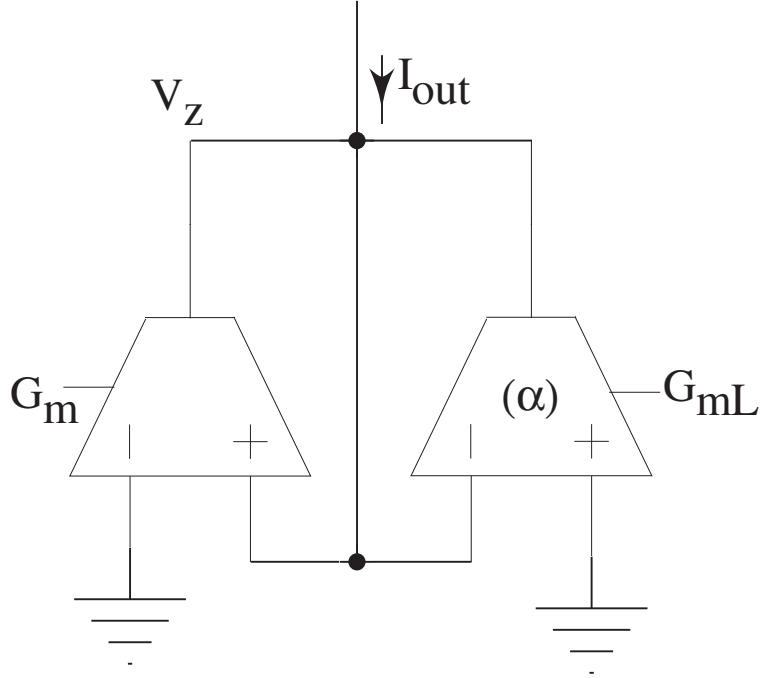


Figure 27. OTA implementation of negative resistance. The linear range of the negative-feedback OTA is much greater than that of the positive-feedback OTA. The bias current of the nonlinear OTA is slightly larger than I_b .

where ρ is a small, positive number. Then, the general shape of (135) is of that shown in Fig. 26 (a). The attraction of implementing the nonlinear resistor as such is that it merely depends on manipulation of OTA linear ranges and bias currents, rather than on the addition and design of other types of circuit elements.

If we implement the nonlinear resistor as described, then, after nondimensionalization of (135), (133) becomes

$$\ddot{z} + \underbrace{\frac{d}{dz}(z - (1 + \rho)H(z))}_{f(z)} \dot{z} + z = 0, \quad (137)$$

where we have set $\gamma(z) = z$.

We can glean some intuition about the system's oscillatory behavior by studying Fig. 26 (a). Close to the origin, the slope (*i.e.* $f(z)$) is negative, which implies negative damping. So, energy is pumped into the system of (133) when it is close to the origin,

ensuring a self-starting condition. Farther from the origin, damping is positive, which limits the amplitude of the signal.

Once steady state oscillation is achieved, the movement of the system's signal is confined to the dashed region of Fig. 26(a). The size of this region can be found by calculating the location of the extrema of $z - (1 + \rho)H(z)$. Figure 26(b) shows a plot of the region size versus ρ . Note that the oscillation region size is also dependent on $H(z)$.

Within the region of oscillation, $f(z)$ may be approximated by the following even-order function

$$f(z) \approx -\rho \left(1 - z^{2\nu}/m_\rho^{2\nu}\right), \quad (138)$$

where m_ρ is a function of ρ such that $f(m_\rho) = 0$. This approximation is derived from noting that $H(z)$ is an odd function, of order $2\nu + 1 \geq 3$, and then fitting a 2ν -order function to pass through the point $(0, f(0))$ and the roots of $f(z)$. Equation (137) is now approximately

$$\ddot{z} - \rho(1 - z^{2\nu}/m_\rho^{2\nu})\dot{z} + z = 0, \quad \rho > 0. \quad (139)$$

We identify a perturbation parameter, $\epsilon = \rho$ and define $y = z/m_\rho$ to write

$$\ddot{y} - \epsilon(1 - y^{2\nu})\dot{y} + y = 0, \quad \epsilon > 0. \quad (140)$$

From Liénard's Theorem, (140) exhibits a stable, unique oscillation. Further, since it is just a perturbation of a linear resonator, we can expect very-nearly sinusoidal oscillations for small enough ϵ . The behavior of this oscillator can be analyzed using multi-timescale perturbation or via the method of averaging [20].

To perform the averaging method, we write the solution to (140), as in Chapter 5, as

$$y = R(t) \cos(t + \psi(t)) \quad (141)$$

and require

$$\frac{dy}{dt} = -R(t) \sin(t + \psi(t)) \quad (142)$$

$$\frac{d^2y}{dt^2} = -\frac{R(t)}{dt} \sin(t + \psi(t)) - R(t) \cos(t + \psi(t)) \left(1 + \frac{d\psi(t)}{dt}\right), \quad (143)$$

to hold.

Equations (141) and (142) imply

$$\frac{dR}{dt} \cos(t + \psi) - R \sin(t + \psi) \frac{d\psi}{dt} = 0, \quad (144)$$

and (141), (142) and (143) substituted into (140) give

$$-\frac{dR}{dt} \sin(t + \psi) - R \cos(t + \psi) \frac{d\psi}{dt} = \epsilon(-1 + (R \cos(t + \psi))^{2\nu}) R \sin(t + \psi) \quad (145)$$

Applying the near-identity transformations to (144) and (145), we can derive the slow flow equations to be

$$\begin{aligned} \frac{d\bar{R}}{dt} &= \frac{\epsilon\bar{R}}{2\pi} \int_0^{2\pi} \sin(t + \bar{\psi})^2 (1 - (\bar{R} \cos(t + \bar{\psi}))^{2\nu}) dt \\ &= \frac{\epsilon\bar{R}}{2\pi} \int_0^{2\pi} \sin(\phi)^2 (1 - (\bar{R} \cos(\phi))^{2\nu}) d\phi \end{aligned} \quad (146)$$

$$\begin{aligned} \frac{d\bar{\psi}}{dt} &= \frac{\epsilon}{2\pi} \int_0^{2\pi} \cos(t + \bar{\psi}) \sin(t + \bar{\psi}) (1 - (\bar{R} \cos(t + \bar{\psi}))^{2\nu}) d\phi \\ &= \frac{\epsilon}{2\pi} \int_0^{2\pi} \cos(\phi) \sin(\phi) (1 - (\bar{R} \cos(\phi))^{2\nu}) dt, \end{aligned} \quad (147)$$

where $\phi = t + \bar{\psi}$.

Equations (146) and (147) can be simplified by recognizing that $\sin(a_1\phi)$ is orthogonal to $\sin(a_2\phi)$ for $a_1 \neq a_2$ and $a_{1,2} \in \mathbb{N}^+$. Also, $\sin(\phi)$ and $\cos(\phi)$ are orthogonal. Recalling the trigonometric identity

$$\sin(\phi)^2 = (1 - \cos(2\phi))/2, \quad (148)$$

it is evident that only the constant term and the $\cos(2\phi)$ term of the expression $1 - (\bar{R} \cos(\phi))^{2\nu}$ will have a non-zero contribution to the integral of (146). Further, the integral of (147) is identically zero.

By applying the Binomial theorem to the Euler expansion of $\cos(\phi)$, we can write

$$1 - (\bar{R} \cos(\phi))^{2\nu} = 1 - \frac{(2\nu)! \bar{R}^{2\nu}}{\nu! \nu! 2^{2\nu}} + \frac{\bar{R}^{2\nu}}{2^{2\nu-1}} \sum_{k=0}^{\nu} \left(\cos(\phi(2\nu - 2k)) \frac{(2\nu)!}{(2\nu - k)! k!} \right) \quad (149)$$

Using the identity of (148), and considering only the constant and $\cos(2\phi)$ terms of (149), (146) becomes

$$\frac{d\bar{R}}{dt} = \frac{\epsilon \bar{R}}{2\pi} \int_0^{2\pi} \frac{1 - \cos(2\phi)}{2} \left(1 - \frac{(2\nu)! \bar{R}^{2\nu}}{\nu! \nu! 2^{2\nu}} + \frac{(2\nu)! \bar{R}^{2\nu} \cos(2\phi)}{(\nu + 1)! (\nu - 1)! 2^{2\nu-1}} \right) d\phi$$

Over one cycle, the integral of $\cos(2\phi)$ is 0, while the integrals of 1 and $\cos^2(2\phi)$ are 2π and π , respectively. We can write

$$\begin{aligned} \frac{d\bar{R}}{dt} &= \frac{\epsilon \bar{R}}{2\pi} \int_0^{2\pi} \frac{1}{2} \left(1 - \frac{(2\nu)! \bar{R}^{2\nu}}{\nu! \nu! 2^{2\nu}} \right) + \frac{(2\nu)! \bar{R}^{2\nu} \cos^2(2\phi)}{(\nu + 1)! (\nu - 1)! 2^{2\nu}} d\phi \\ &= \frac{\epsilon \bar{R}}{2} \left(1 - \frac{(2\nu)! \bar{R}^{2\nu}}{\nu! \nu! 2^{2\nu}} + \frac{(2\nu)! \bar{R}^{2\nu}}{(\nu + 1)! (\nu - 1)! 2^{2\nu}} \right) \\ &= \frac{\epsilon \bar{R}}{2} \left(1 - \frac{(2\nu)! \bar{R}^{2\nu}}{2^{2\nu}} \frac{(\nu + 1)! (\nu - 1)! - \nu! \nu!}{\nu! \nu! (\nu + 1)! (\nu - 1)!} \right). \end{aligned}$$

At steady state, \bar{R} is equal to the equilibrium point of (150), which is determined by setting the RHS of (150) to 0 and solving for \bar{R} . This gives a steady state value of

$$\bar{R}^* = \sqrt[2\nu]{\frac{2^{2\nu} \nu! \nu! (\nu + 1)! (\nu - 1)!}{2\nu ((\nu + 1)! (\nu - 1)! - \nu! \nu!)}}. \quad (150)$$

To first order, the steady-state solution to (140) is then

$$y(t) = \sqrt[2\nu]{\frac{2^{2\nu} \nu! \nu! (\nu + 1)! (\nu - 1)!}{2\nu ((\nu + 1)! (\nu - 1)! - \nu! \nu!)}} \cos(t). \quad (151)$$

For most of this chapter, we will assume $\nu = 1$, meaning that (140) simplifies to

$$\ddot{y} - \epsilon(1 - y^2)\dot{y} + y = 0, \quad \epsilon > 0, \quad (152)$$

which is the van der Pol oscillator [31].

Note that Liénard's Theorem is valid only if the nonlinearity is continuously differentiable. Even though most physical circuits have continuously-differentiable transfer functions, there exists another analysis method, describing functions [24], that can handle the case of functions with discontinuous derivatives (*i.e.* piecewise linear functions).

6.3 OTA-C oscillator synthesis

An OTA-C implementation of the Liénard equation will involve a second-order section and some form of nonlinearity. The nonlinearity may be external to the second-order section [22–25] or may be an inherent part of it [27, 28]. We espouse the latter approach and present here a general method for synthesizing a sinusoidal oscillator this way.

6.3.1 Linear OTA-C second-order sections

Figure 28 depicts a general OTA-C second-order section (SOS) [32]. It has two dominant poles, each of which is produced by a low conductance/high capacitance node. We can derive the governing dynamics of an SOS by applying Kirchhoff’s Current Law (KCL) to each of its two nodes. The only way that current can flow onto a node is either through a capacitor, or through an OTA. Assuming no floating nodes, there are at most three effective capacitors in an SOS: the two grounded capacitors at either node, and the floating capacitor between both nodes. The inputs to any OTA can only be a linear combination of the node voltages. If all of the OTAs are operated linearly, then the sum of the OTA currents at a given node is simply a linear combination of the node voltages. With all of the above constraints, any OTA-C SOS is fully described by [32]

$$\begin{bmatrix} C_1 \dot{V}_1 \\ C_2 \dot{V}_2 \end{bmatrix} = \begin{bmatrix} G_{11} & G_{12} \\ G_{21} & G_{22} \end{bmatrix} \begin{bmatrix} V_1 \\ V_2 \end{bmatrix} + C_f \begin{bmatrix} \dot{V}_2 - \dot{V}_1 \\ \dot{V}_1 - \dot{V}_2 \end{bmatrix}, \quad (153)$$

where V_1 and V_2 are the node voltages. The quantities C_1 , C_2 and C_f are the capacitances of the two grounded capacitors and of the floating capacitor, respectively. Finally, each G_{ij} is the effective OTA small-signal transconductance gain of V_j seen by the i ’th node. We make the following definitions

$$\begin{aligned} \phi &= C_f/C_1; & k &= C_1/C_2; & \tau &= t \cdot G/C_1; \\ x_1 &= V_1/V_c; & x_2 &= V_2/V_c, \end{aligned} \quad (154)$$

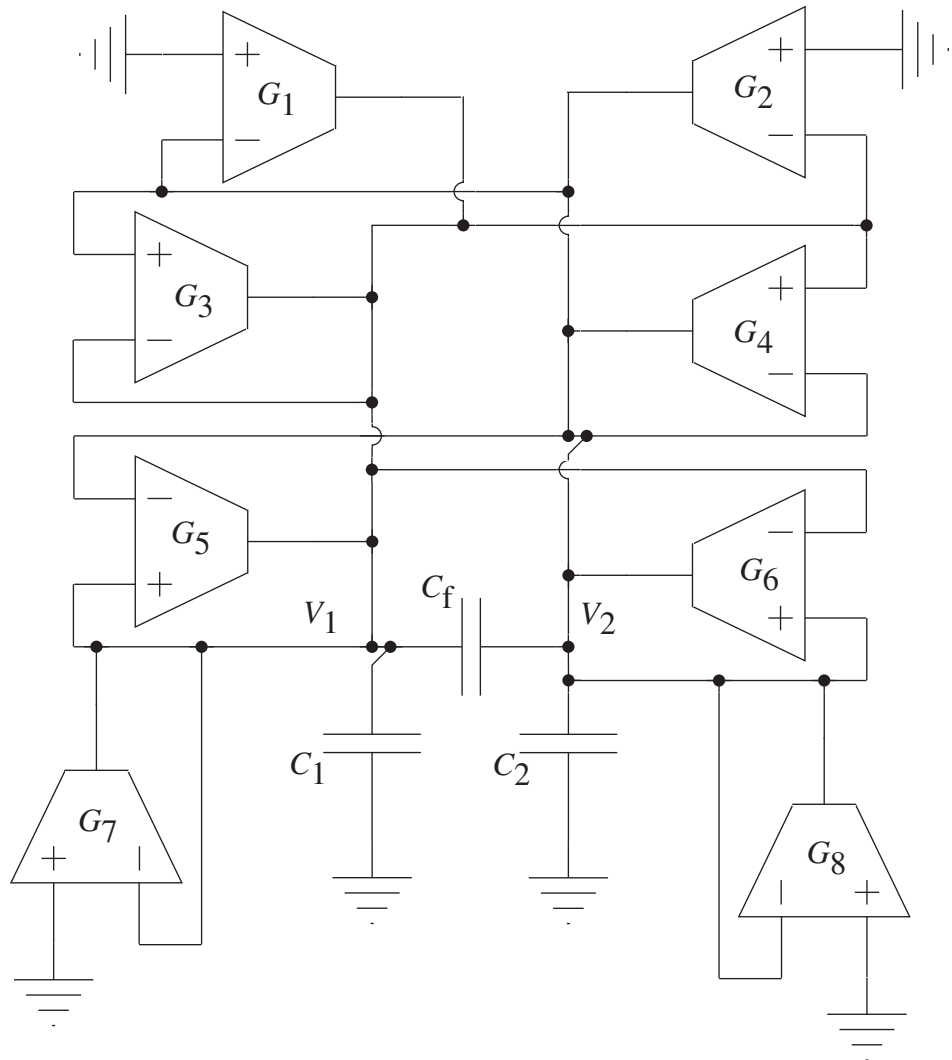


Figure 28. Generic OTA-C SOS. The depicted circuit contains all possible elements and connections, without redundancy, of an OTA-C second-order section. Any given OTA-C SOS is a subset of this generic circuit.

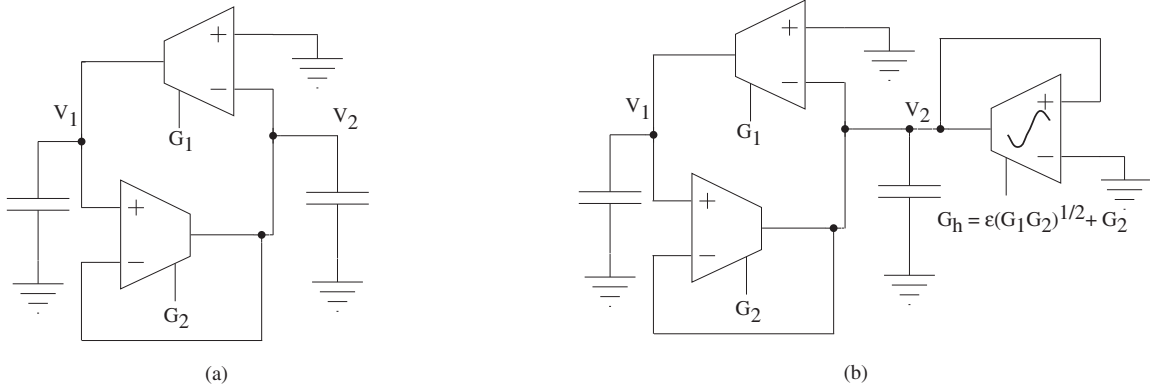


Figure 29. Simple van der Pol derivation. (a) Initial SOS circuit, with all linear OTAs. (b) A nonlinear OTA converts SOS into the van der Pol oscillator.

where G is some representative transconductance gain; for example $G = \max(G_{11-22})$. Once we introduce the nonlinear OTA, V_c will be defined in terms of the corresponding $H(y)$ nonlinearity. The quantities x_1 and x_2 are state variables that are scaled according to V_c . Applying the substitutions of (154), the dimensionless state-space form of (153) is

$$\begin{bmatrix} \dot{x}_1 \\ \dot{x}_2 \end{bmatrix} = \underbrace{\begin{bmatrix} a & b \\ c & d \end{bmatrix}}_A \begin{bmatrix} x_1 \\ x_2 \end{bmatrix} + \phi \begin{bmatrix} \dot{x}_2 - \dot{x}_1 \\ k\dot{x}_1 - k\dot{x}_2 \end{bmatrix}. \quad (155)$$

The state variables x_1, x_2 are differentiated with respect to the dimensionless independent variable, τ . We will mostly assume that there are no floating capacitors in the SOS. That is, $\phi = C_f = 0$.

6.3.2 Conversion from a linear SOS to an oscillator

The oscillator design is essentially a question of converting (155) to (137). The one constraint is that this conversion to Liénard's equation be physically realizable, using a nonlinear OTA. Note that the OTA's only possible inputs are the state variables, x_1, x_2 . Also, the OTA's output must be added directly to the dynamics of exactly one or the other state variable. So, converting (155) to the Liénard equation can only

involve adding a vector of the form

$$\begin{bmatrix} g_h \cdot H(px_1 + qx_2) \\ 0 \end{bmatrix} \text{ or } \begin{bmatrix} 0 \\ g_h \cdot H(px_1 + qx_2) \end{bmatrix}, \quad (156)$$

to the RHS of (155). Here, $H(\cdot)$ is the nonlinear OTA's sigmoidal function and its argument is a weighted sum of x_1 and x_2 . Also, g_h is a dimensionless representation of the nonlinear OTA's small-signal transconductance gain. Successful oscillator design depends on choosing the appropriate values of p , q and g_h .

6.3.2.1 Some special cases

I will introduce the synthesis procedure with the simple SOS depicted in Fig. 29(a), where the OTAs are linear, and G_1, G_2 are their respective transconductance gains. By applying KCL, we derive the following state space equation,

$$\begin{bmatrix} \dot{x}_1 \\ \dot{x}_2 \end{bmatrix} = \begin{bmatrix} 0 & b \\ c & d \end{bmatrix} \begin{bmatrix} x_1 \\ x_2 \end{bmatrix}, \quad (157)$$

where $b \propto G_1$, $c \propto G_2$ and $d \propto G_2$. Notice that \mathbf{A} is a lower skew-triangular matrix in this example. For \mathbf{A} of this type, we convert (155) into the Liénard equation by simply adding $(\mu - d)H(x_2)$ to the x_2 dynamics. We have picked $p = 0$, $q = 1$ and $g_h = (\mu - d)$, where μ is to be determined. Adding $(\mu - d)H(x_2)$ to the x_2 dynamics of (157) yields

$$\begin{bmatrix} \dot{x}_1 \\ \dot{x}_2 \end{bmatrix} = \begin{bmatrix} bx_2 \\ cx_1 + dx_2 - (d - \mu)H(x_2) \end{bmatrix}, \quad (158)$$

which, as a single differential equation, is

$$\ddot{x}_2 - (d - (d - \mu)H'(x_2))\dot{x}_2 - bcx_2 = 0. \quad (159)$$

As discussed earlier (see (139)), this can be approximated as

$$\ddot{x}_2 - \mu \left(1 - \frac{x_2^2}{m_\mu^2}\right) \dot{x}_2 - bcx_2 = 0, \quad (160)$$

where m_μ is a function of μ such that $H'(m_\mu) = d/(d - \mu)$.

If we define

$$\begin{aligned} y &= x_2/m_\mu, \\ \mu &= \epsilon\sqrt{-bc}, \end{aligned} \tag{161}$$

and rescale time as

$$T = \sqrt{-bc} \cdot \tau, \tag{162}$$

then (159) becomes

$$\frac{d^2y}{dT^2} - \epsilon(1 - y^2) \frac{dy}{dT} + y = 0, \tag{163}$$

the van der Pol equation. Note that, for the conversion to make sense, we must have $bc < 0$ and $d < 0$. From (158) and (161), we can infer the required placement of the nonlinear OTA. The positive input is x_2 , the negative input is (a.c.) ground, and the output current is sourced onto node x_2 . In addition, we must bias the nonlinear OTA such that its small-signal transconductance gain corresponds to $\epsilon\sqrt{-bc} - d$. Figure 29(b) depicts the augmented SOS circuit, now an oscillator.

If \mathbf{A} is an upper skew-triangular matrix, then we can obtain an oscillator by a series of similar steps as above. We place a nonlinear OTA whose output and positive input are connected to node x_1 . Also, its negative output must be at ground, and it must be biased to have a small-signal gain corresponding to $\epsilon\sqrt{-bc} - a$. Again, we require $bc < 0$, and also $a < 0$.

6.3.2.2 *The general case*

When \mathbf{A} is not skew-triangular, it is a little trickier to convert (155) into the Liénard system. With the general form of (155), improper placement of the nonlinearity can cause unwanted distortion. The issue is that the dynamics of one state variable will couple into those of the other. Assuming $\phi = 0$, we can reduce the interdependence of the states by changing the axes of the dynamical system.

Consider a new state vector, $\underline{v} = [v_1 \ v_2]^T$, defined as

$$\begin{bmatrix} v_1 \\ v_2 \end{bmatrix} = \begin{bmatrix} x_1 \\ cx_1 + dx_2 \end{bmatrix}. \quad (164)$$

Written in terms of \underline{v} , with $\phi = 0$, (155) becomes,

$$\begin{bmatrix} \dot{v}_1 \\ \dot{v}_2 \end{bmatrix} = \begin{bmatrix} a - \frac{bc}{d} & \frac{b}{d} \\ 0 & d \end{bmatrix} \begin{bmatrix} v_1 \\ v_2 \end{bmatrix} + \begin{bmatrix} 0 \\ cv_1 \end{bmatrix}. \quad (165)$$

We convert (165) into the Liénard equation by simply adding $g_h \cdot H(v_2)$ to the v_1 dynamics. Again, g_h refers to the small-signal gain of the nonlinear OTA. After adding the nonlinear OTA to (165), we arrive at the following second-order ODE

$$\ddot{v}_2 - (a + d + cg_h H'(v_2)) \dot{v}_2 + (ad - bc) v_2 = 0, \quad (166)$$

which is approximately

$$\ddot{v}_2 - (a + d + cg_h) \left(1 - \frac{v_2^2}{m_{gh}^2}\right) \dot{v}_2 + (ad - bc) v_2 = 0, \quad (167)$$

where m_{gh} is such that $H'(m_{gh}) = -(a + d)/(cg_h)$.

Next, we rescale time as $T = \sqrt{ad - bc} \cdot \tau$, and define

$$\epsilon = (a + d + cg_h)(ad - bc)^{-\frac{1}{2}}, \quad (168)$$

$$y = v_2/m_{gh}, \quad (169)$$

to get

$$\frac{d^2 y}{dT^2} - \epsilon (1 - y^2) \frac{dy}{dT} + y = 0, \quad (170)$$

as desired. Note from (169) that we require

$$ad - bc > 0 \quad (171)$$

$$a + d < 0, \quad (172)$$

which are the same conditions for \mathbf{A} to be Hurwitz. That is, the SOS must be stable¹. These inequalities are consistent with those for when \mathbf{A} is a skew-triangular matrix.

6.3.2.3 Summary

Any stable linear OTA-C SOS circuit can be converted into an oscillator via OTA nonlinearity. This is done by augmenting the linear SOS, (155), with a nonlinear OTA in the form of the first vector in (156), choosing

$$p = c; \quad q = d; \quad (173)$$

$$g_h = \left(\epsilon \sqrt{ad - bc} - (a + d) \right) / c. \quad (174)$$

Notice that we would have arrived at a very similar alternative solution, if we had defined \underline{v} as

$$\begin{bmatrix} v_1 \\ v_2 \end{bmatrix} = \begin{bmatrix} ax_1 + bx_2 \\ x_2 \end{bmatrix}. \quad (175)$$

6.4 Characteristics of the van der Pol equation

OTA nonlinearity is an appealing choice for amplitude limiting in oscillators, because it is power- and area-efficient. When the nonlinearity results in the van der Pol oscillator, we enjoy the additional benefit of having implemented a well-known and studied dynamical system. The choices of design parameters for the oscillator can then be informed by analytical results from the field of perturbation theory.

The van der Pol equation has no closed-form solution. However, for small enough ϵ , we can use first-order averaging to find an approximate solution [20]. Setting $\nu = 1$ in (150), we find the amplitude of $y(T)$ to be described by

$$\frac{dA_y}{dt} = \frac{\epsilon}{8} A_y (4 - A_y), \quad (176)$$

¹It is possible to convert an unstable SOS into an oscillator, using a procedure very similar to that which we have so far described. The main difference is that the nonlinearity involved would be expansive (as encountered, for instance, in a current feedback operational amplifier), rather than the usual OTA compressive function.

which gives

$$A_y = \frac{2}{\sqrt{1 - e^{-\epsilon T} \left(1 + \frac{4}{y_0^2}\right)}}, \quad (177)$$

where y_0 depends on initial conditions. The approximate solution to the van der Pol equation is thus

$$y(T) = \frac{2 \cos T}{\sqrt{1 - e^{-\epsilon T} \left(1 + \frac{4}{y_0^2}\right)}}. \quad (178)$$

Note that, as $T \rightarrow \infty$, the solution approaches a sinusoid of amplitude 2. Further, this approach is roughly at a rate of $e^{-\epsilon T}$. The oscillator's start-up time is thus proportional to $1/\epsilon$.

Applying higher-order perturbation analysis [20] reveals that, at steady state, the solution to (170) is

$$\begin{aligned} y(T) = & 2 \cos(T) + 3\epsilon/4 \sin(T) - \epsilon^2/8 \cos(T) + \\ & -\epsilon/4 \sin(3T) + 3\epsilon^2/16 \cos(3T) + \\ & -5\epsilon^2/96 \cos(5T) + O(\epsilon^3). \end{aligned} \quad (179)$$

We would ideally want an oscillator that has no higher-order harmonics. The square-root of the ratio of harmonic power to fundamental frequency power is a measure of this nonideality, and is referred to as total harmonic distortion (THD). From (179), we derive the following expression for THD

$$\begin{aligned} \text{THD \%} &= \frac{\epsilon}{8} \sqrt{\frac{1 + 349\epsilon/576}{1 + \epsilon^2/64 + \epsilon^4/256}} \cdot 100 \\ &\approx 12.5\epsilon + 3.8\epsilon^2. \end{aligned} \quad (180)$$

According to (168), ϵ depends on how much bigger g_n is than $|a+d|$. It is effectively a measure of the strength of the nonlinear OTA relative to the linear ones. That THD increases with ϵ matches the intuition that the oscillator's nonlinearity be 'weak', or 'soft'.

6.5 OTA-C oscillator analysis and design considerations

So far, the treatment has been mostly theoretical. In this and the following sections, we address the implications that the design framework has for a practical oscillator implementation.

6.5.1 Frequency of oscillation

From (178), the system oscillates at a rate of one cycle per 2π units of T . Recalling $T = \tau\sqrt{ad - bc}$, and $\tau = tG/C_1$, this corresponds to an oscillation frequency of

$$w_o = G\sqrt{ad - bc}/C_1 \text{ rads}^{-1}. \quad (181)$$

The quantity G is some representative transconductance gain of the linear SOS of (153) (*e.g.* $G = \max(G_{11-22})$). If we maintain the relative gains of the amplifiers — that is, a, b, c, d are kept constant — then increasing G will cause a linear increase in the frequency of oscillation.

6.5.2 Amplitude of oscillation

According to (178), the circuit oscillates at an amplitude of 2 units of the y quantity. In terms of the v_2 variable, the amplitude of oscillation is (see (169))

$$\text{amp}(v_2) = 2m_{\text{gh}}. \quad (182)$$

From (164), v_2 is the derivative of x_2 with respect to τ . Using this fact, and replacing x_2 and τ with their expressions in V_2 and t , respectively, we find the voltage amplitude of oscillation to be

$$\text{amp}(V_2) = \frac{2m_{\text{gh}}V_c}{\sqrt{ad - bc}}. \quad (183)$$

Recall that m_{gh} is defined as

$$H'(m_{\text{gh}}) = -(a + d)/(cg_h). \quad (184)$$

Using the definition of ϵ , we can write

$$H'(m_{\text{gh}}) = \frac{-(a+d)}{\epsilon\sqrt{ad-bc} - (a+d)}. \quad (185)$$

The amplitude of oscillation is thus

$$\text{amp}(V_2) = \frac{2V_c}{\sqrt{ad-bc}} (H')^{-1} \left(\frac{-(a+d)}{\epsilon\sqrt{ad-bc} - (a+d)} \right). \quad (186)$$

For small ϵ , the oscillation amplitude equation can be simplified to

$$\text{amp}(V_2) \approx \frac{V_c}{\sqrt{n}} \frac{2\sqrt{\epsilon}}{\sqrt{3\sqrt{ad-bc}(\epsilon\sqrt{ad-bc} - (a+d))}}, \quad (187)$$

where n is the Taylor series cubic term of $H(y)$. The equation above reveals that the oscillation amplitude with respect to V_c/\sqrt{n} is solely determined by ϵ and the topological parameters a, b, c, d . It does not depend on the specific OTA, as long as the dominant nonlinearity is cubic, nor whether it is biased above or below threshold. However, the specific values of V_c and ϵ may change with OTA bias region and with OTA topology. Similar observations can be made for OTAs whose nonlinear function $H(y)$ is not dominantly cubic.

6.5.3 Inputs to the nonlinear OTA

We have shown that the input to the nonlinear OTA must be $cx_1 + dx_2$. Figure 30 depicts a generic circuit for generating the inputs in question. Notice that in the circuit diagram, the argument to the nonlinear OTA is $v_3 = x_1 + x_2d/c$, instead of $v_2 = cx_1 + dx_2$. Defining $v_3 = v_2/c$, (166) becomes

$$\ddot{v}_3 - (a+d + cg_{\text{h}}H'(cv_3))\dot{v}_3 + (ad-bc)v_3 = 0. \quad (188)$$

It is then straightforward to show that the circuit of Fig. 30 meets all of the established conditions for oscillator design, and that all of the previous results still hold, with the slight correction $\text{amp}(v_3) = \text{amp}(v_2)/c$.

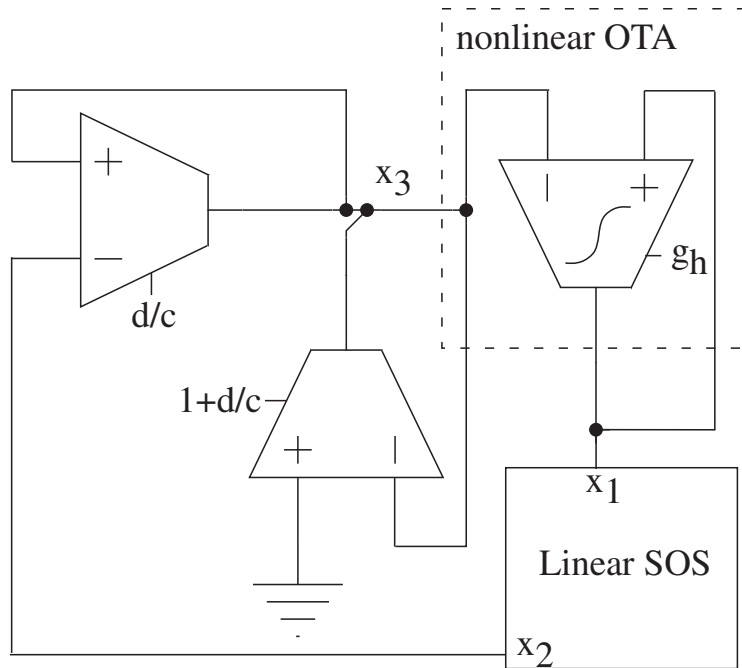


Figure 30. Inputs to the nonlinear OTA.

6.6 An illustrative example

In this section, we will apply the oscillator synthesis procedure to the Lyon/Mead SOS [14] depicted in Fig. 31. The oscillator designer's choice of SOS topology should normally depend on such considerations as noise and distortion, as addressed by Koziel *et al.* [33]. This particular SOS structure is chosen less for any technical merits of the resulting oscillator than for the sheer arbitrariness of it. The major claim in this chapter is that *any* stable SOS can be converted into a controllable, well-behaved sinusoidal oscillator. It would not be useful to support this claim with, say, the circuit of Fig. 29, since it is a lossy resonator, whose conversion to a stable oscillator might seem intuitive almost to the point of being trivial. The Lyon/Mead SOS, however, has traditionally been viewed not as a sinusoidal oscillator, but for decades as a simple filter model of the cochlea by the neuromorphic community. Hence, it is probably unlikely to be a contrived demonstration of the synthesis procedure.

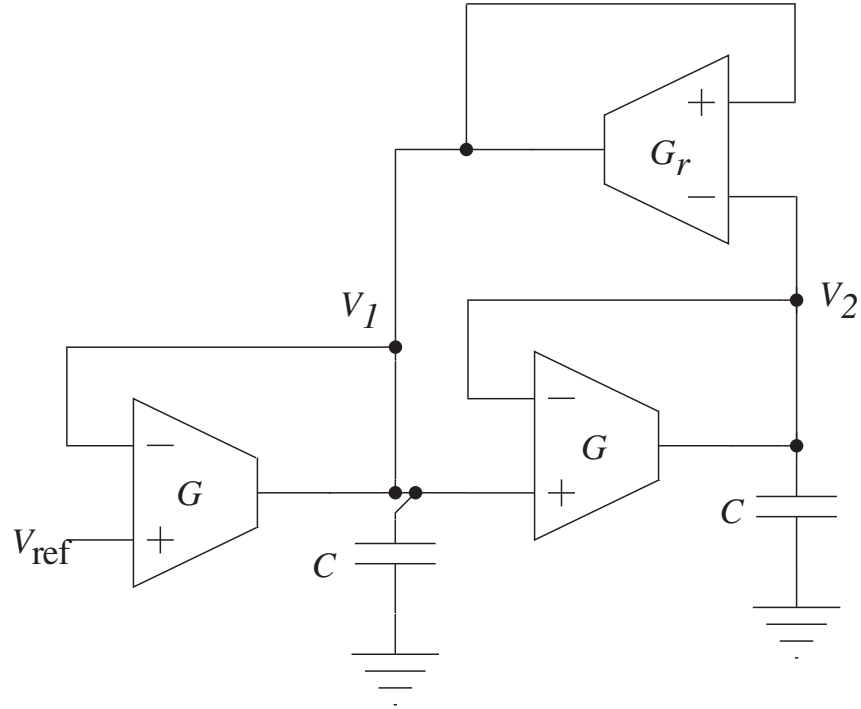


Figure 31. The SOS introduced by Lyon and Mead [14] is normally operated as a low-pass filter. We can apply the synthesis methodology to convert it into an autonomous oscillator with independently-controllable amplitude and frequency of oscillation.

6.6.1 Placement of the nonlinear OTA

Applying KCL to nodes V_1 and V_2 of Fig. 31, we get the following set of differential equations

$$C \begin{bmatrix} \dot{V}_1 \\ \dot{V}_2 \end{bmatrix} = \begin{bmatrix} G_r - G & -G_r \\ G & -G \end{bmatrix} \begin{bmatrix} V_1 \\ V_2 \end{bmatrix}, \quad (189)$$

where the node voltages are all referenced to V_{ref} , and each OTA is assumed to be linear. We make the following definitions

$$\begin{aligned} x_1 &= V_1/V_c; & x_2 &= V_2/V_c; \\ \tau &= t \cdot G/C; & r &= G_r/G, \end{aligned} \quad (190)$$

to get the following dimensionless state-space expression

$$\begin{bmatrix} \dot{x}_1 \\ \dot{x}_2 \end{bmatrix} = \underbrace{\begin{bmatrix} r-1 & -r \\ 1 & -1 \end{bmatrix}}_{\mathbf{A}} \begin{bmatrix} x_1 \\ x_2 \end{bmatrix}. \quad (191)$$

The transconductance matrix \mathbf{A} is Hurwitz for $r < 2$, meaning that OTA nonlinearity can convert the SOS of Fig. 31 into an oscillator. From the synthesis procedure, we determine that the nonlinear OTA should have a differential input of $x_1 - x_2$, with its output current sourced onto node x_1 . From (174) and (191), the small-signal gain of the nonlinear OTA should be

$$g = 2 + \epsilon - r, \quad (192)$$

which, in dimensionalized form, is

$$G_h = (2 + \epsilon)G - G_r. \quad (193)$$

When the nonlinear OTA is added to the original Lyon/Mead SOS, we obtain the circuit shown in Fig. 32(a). It should start to oscillate once G_h is larger than $2G - G_r$.

6.6.2 OTA consolidation

Notice from Fig. 32(a) that the nonlinear OTA shares its inputs and output with the G_r OTA. The linear term of the nonlinear OTA renders OTA G_r redundant. We can eliminate this OTA, which implies $G_r = r = 0$. The small-signal gain of the nonlinear OTA is now

$$G_h = (2 + \epsilon)G. \quad (194)$$

Figure 32(b) shows the consolidated circuit, which comprises two linear OTAs and a nonlinear one.

6.6.3 Circuit implementation

The linear OTAs in Fig. 32(b) were each implemented as the variable gain OTA of Fig. 33, originally introduced by DeWeerth *et al.* [34]. The attenuation stage is

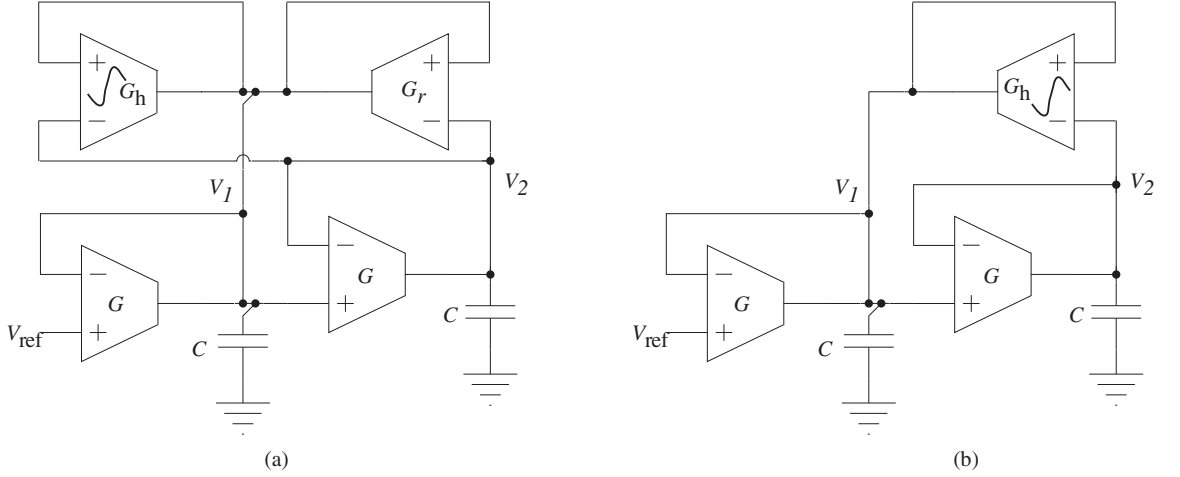


Figure 32. SOS conversion to an oscillator. (a) OTA-C circuit that results from direct application of synthesis methodology. (b) OTA-C circuit after consolidation. The G_h and G_r OTAs are merged into one, since they share the same input and output nodes.

highlighted with a dashed box, where the input voltage is attenuated by the ratio of the transconductance gains of the nMOS differential pair to that of their diode-connected pMOS loads. The nMOS differential pair operates in strong inversion, while the pMOS loads are sized to operate in subthreshold. This gives an attenuation factor of [34]

$$\alpha = \frac{U_T}{\kappa} \sqrt{\frac{2\beta_\alpha}{I_\alpha}}, \quad (195)$$

where β_α is a constant that depends on the physical dimensions of the nMOS transistors in the attenuation stage, and $I_\alpha \approx 5\mu\text{A}$ is the bias current through this stage.

The nonlinear OTA was implemented as a current-mirror nine-transistor OTA, that is, the circuit shown in Fig. 33, minus the attenuation stage. The attenuation factor for the nonlinear OTA is effectively fixed at $\alpha = 1$.

The on-chip capacitors were fabricated as poly-poly capacitors with $C = 912.5\text{fF}$. The parasitic input capacitance of the attenuators (on the order of 1pF) add to these poly-poly capacitors, making the total effective capacitance hard to predict precisely. A correction term must therefore be factored into the frequency-of-oscillation equation.

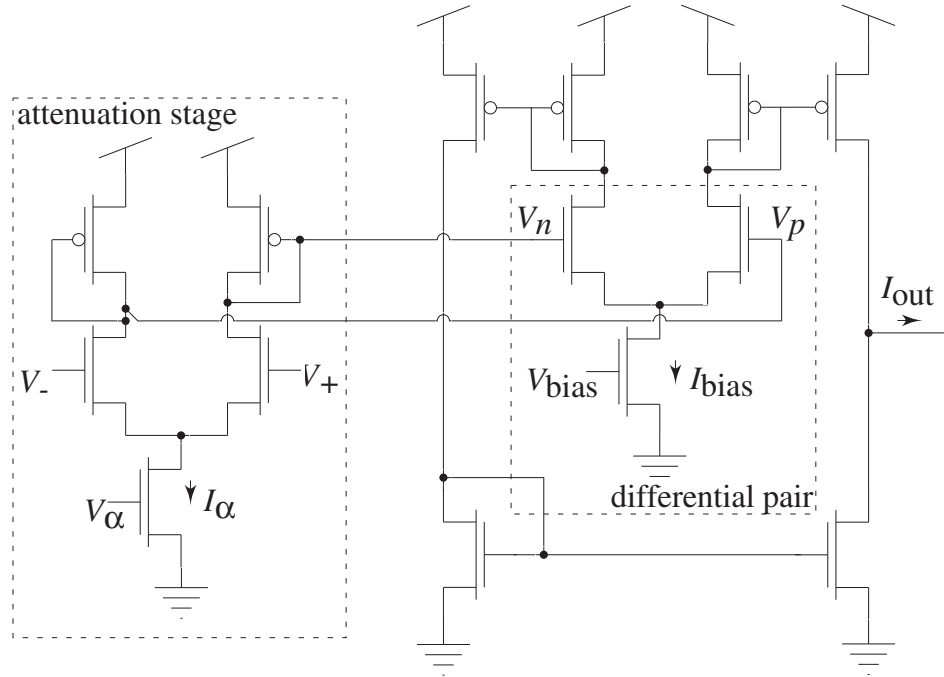


Figure 33. The variable linear range OTA. The attenuation stage of the OTA consists of an above-threshold differential pair that is loaded by subthreshold diode-connected transistors. The disparate gains of the above- and subthreshold transistors result in voltage attenuation between V_+ , V_- and V_p , V_n . The level of attenuation is controlled by the bias current, I_α . The output of the attenuation stage is fed to a simple nine-transistor OTA. Transistor dimensions, attenuation stage: nMOS $W/L = 3\mu\text{m}/100\mu\text{m}$; pMOS $W/L = 100\mu\text{m}/3\mu\text{m}$. Current mirror OTA: nMOS $W/L = 20\mu\text{m}/3\mu\text{m}$; pMOS $W/L = 40\mu\text{m}/3\mu\text{m}$.

6.6.4 Experimental results

We fabricated the OTA-C circuit of Fig. 32(b) in a $0.5\mu\text{m}$ process available from MOSIS. The die photo is shown in Fig. 34. We had control of the bias currents through the bias transistors' gate voltages. The nodes V_1 and V_2 were accessible via on-chip buffers. The OTAs ran on a single-ended supply of 3.3V and had a bandwidth of a few hundred kHz.

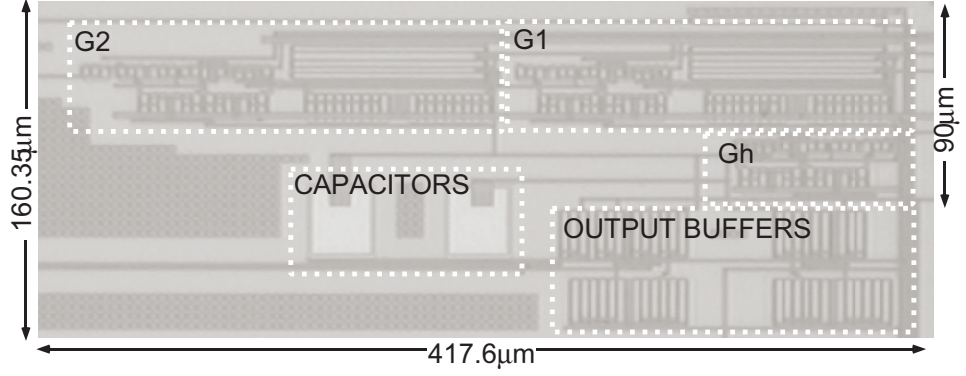


Figure 34. Oscillator die micrograph. The labeled portions correspond to the circuit components in Fig. 32(b). Total area, including output buffers, is $160.35\mu\text{m} \times 417.60\mu\text{m}$.

For subthreshold operation, the transconductance gains were defined as

$$G = I_{\text{avg}} \cdot \frac{\alpha\kappa}{2U_T}, \quad (196)$$

$$G_h = \underbrace{\alpha I_{\text{avg}}(2 + \epsilon)}_{I_h} \cdot \frac{\kappa}{2U_T}, \quad (197)$$

where I_{avg} and I_h are the bias currents of the linear and nonlinear OTAs, respectively.

According to (181), the frequency of oscillation should be equal to

$$f = \frac{\alpha\kappa I_{\text{avg}}}{4\pi C U_T} \text{ (Hz)}. \quad (198)$$

Figure 35 is a plot of (198), superimposed on measurement results. Given the uncertainty of the exact value of C , the values $\alpha = 0.1$ and $\kappa = 0.67$ were chosen to fit the data. The figure depicts a linear tuning range of 2.2kHz to 100kHz. The prototype OTAs suffered from low bandwidth, relative to oscillating frequency. So, to keep amplitude constant across the frequency range, the ratio I_h/I_{avg} was manually varied from 0.44 to 0.37 to offset parasitic effects [24]. The power consumption varies over this tuning range from $0.19\mu\text{W}$ to $6.27\mu\text{W}$. If we opt for above-threshold operation, we can push the frequency of oscillation into the low 200kHz range.

Equation (183) predicts that the amplitude of oscillation is $V_{\text{amp}} = 4m_{\text{gh}}V_cV_{\text{pp}}$. We defined m_{gh} as the solution to $H'(m_{\text{gh}}) = 2/(g_h)$. For nonlinear OTAs operated

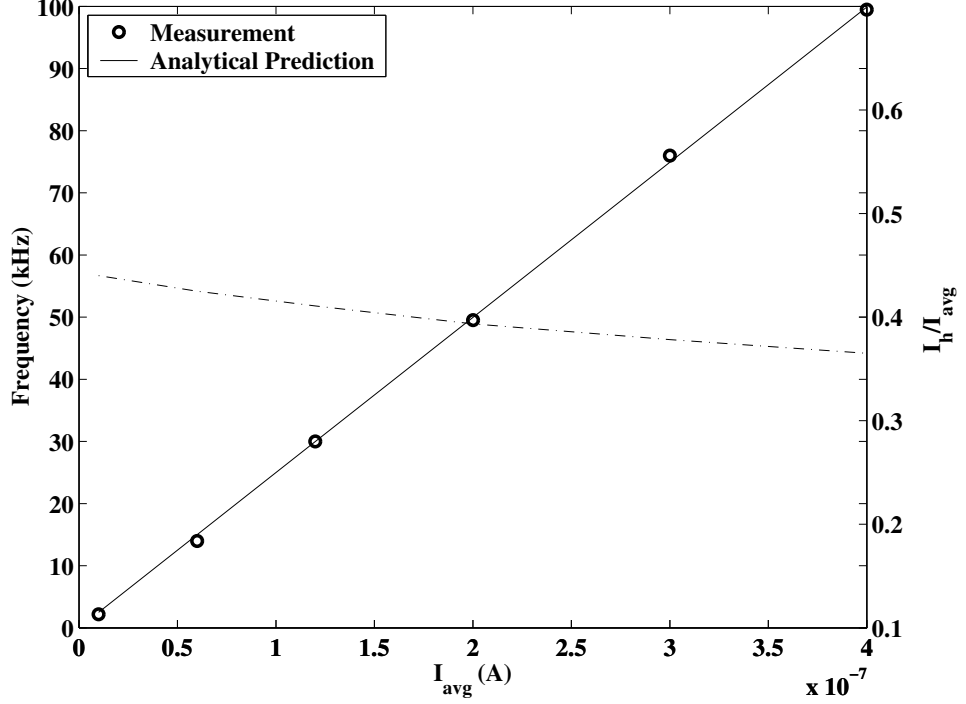


Figure 35. Linear frequency control with current I_{avg} , at 100mV_{pp} oscillation amplitude. Increasing the current increases each transconductance gain, G , proportionally, causing a linear increase in the oscillation frequency. The dashed line (y-axis on the right) is a plot of the ratio of I_h/I_{avg} across this range of frequencies. Ideally, this ratio should be fixed for a constant amplitude of oscillation. However, we manually changed the ratio across frequencies to offset parasitic capacitances in the OTAs.

in the subthreshold region, $H(\cdot) = \tanh(\cdot)$. Hence, m_{gh} is found to be

$$\begin{aligned}
 m_{\text{gh}} &= \tanh^{-1} \left(\sqrt{(g_h - 2)/(g_h)} \right) \\
 &= \tanh^{-1} \left(\sqrt{\frac{\epsilon}{\epsilon + 2}} \right), \tag{199}
 \end{aligned}$$

and the (subthreshold) amplitude of oscillation is

$$V_{\text{amp}} = 8 \frac{U_{\text{T}}}{\kappa} \tanh^{-1} \left(\sqrt{\frac{\epsilon}{\epsilon + 2}} \right) (V_{\text{pp}}). \tag{200}$$

I took experimental measurements of oscillation amplitude versus ϵ , and compared my results to the analytical expression of (200). Figure 36 shows this comparison.

We showed in Section 6.4 that the oscillator's total harmonic distortion depends on ϵ as

$$\text{THD \%} \approx 12.5\epsilon + 3.8\epsilon^2.$$

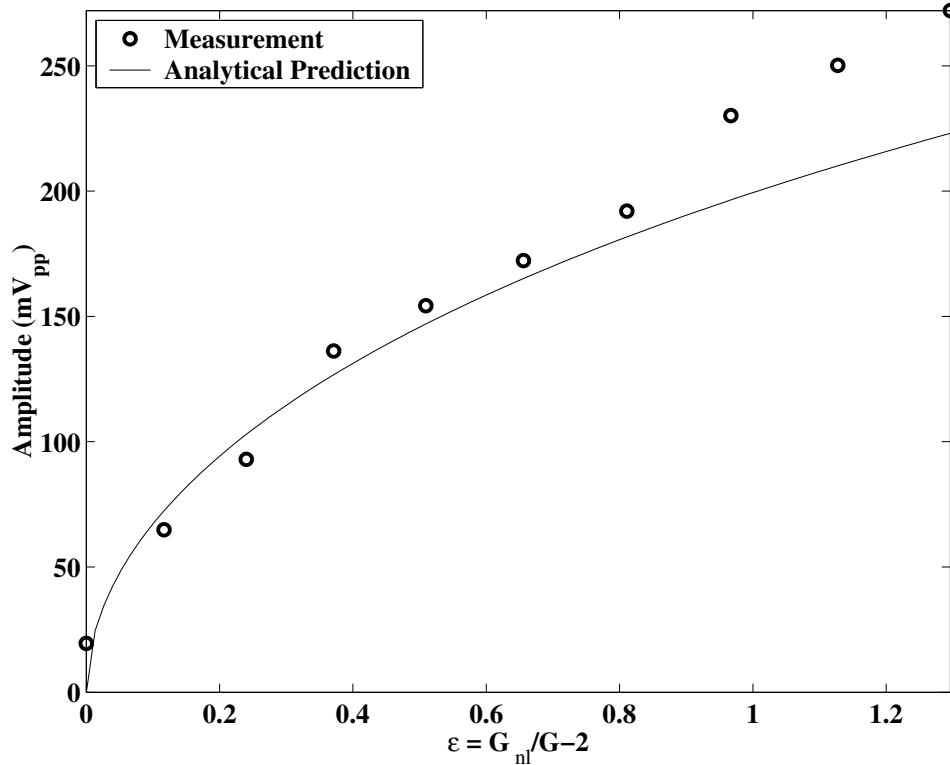


Figure 36. Amplitude control with transconductance G_h , at 100kHz oscillation frequency. The transconductance G_h is directly proportional to ϵ . From (200), the amplitude of oscillation is roughly proportional to $\sqrt{\epsilon}$.

Experimental results (see Fig. 37) show a similar trend to that given by the THD equation. Comparing Figs. 36 and 37, observe that the analytical predictions based on the van der Pol model begin to diverge from measured data as ϵ becomes too large for the synthesized nonlinear resistor to be validly approximated as a simple cubic. Also, fairly high amounts of THD are experienced for relatively small oscillation amplitudes. We can achieve higher oscillation amplitudes with less THD if we operate the OTAs above threshold.

Figure 38 shows a typical measured output power spectrum for when the oscillator is operated above threshold. Here, $I_{avg} = 10\mu A$ and $\epsilon \approx 0.03$. The resulting oscillation is at 146kHz with a 90mV_{pp} amplitude and a THD of only 0.47%. (Compare this to the subthreshold case, where an oscillation amplitude of 90mV would cause a THD of approximately 3%.)

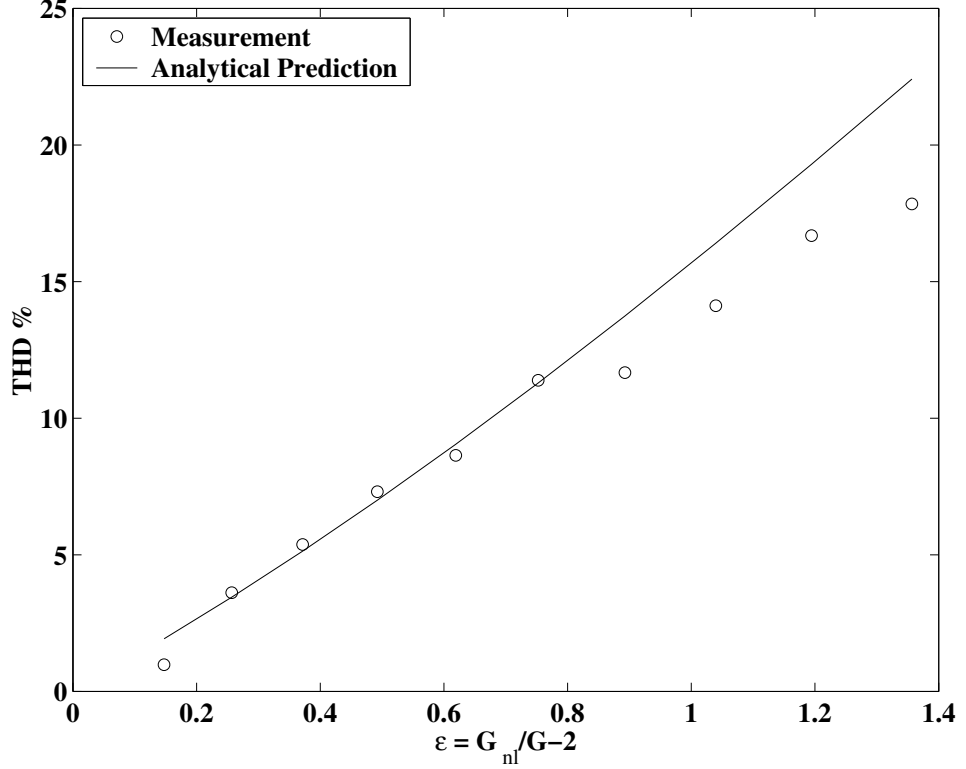


Figure 37. Total harmonic distortion (THD) exhibits a linear dependence on transconductance gain G_{nl} , as predicted by (180). These THD measurements are for an oscillation frequency of 20kHz, and include harmonics up to the 10th.

The unexpected feature of Fig. 38 is that the power spectrum reveals a second harmonic, despite the theoretical solution, (179), having no even-order harmonics. The second harmonic is caused by input offset in the OTA differential pair. Input offset refers to the non-zero differential input voltage at which an OTA has an output current of 0A. Consider the differential pair of Fig. 33, and say it has an offset of V_{off} . Then the output current of the OTA can be written as

$$I_{\text{out}} = F(V_p - V_n - V_{\text{off}}), \quad (201)$$

where $F(\cdot)$ is some function such that $F(0) = 0$, and V_p, V_n are the differential-pair input voltages. In terms of the OTA inputs, V_+ and V_- , we write (201) as

$$\begin{aligned} I_{\text{out}} &= F(\alpha(V_+ - V_-) - V_{\text{off}}), \\ &= F(\alpha(V_+ - V_- - V_{\text{off}}/\alpha)), \end{aligned} \quad (202)$$

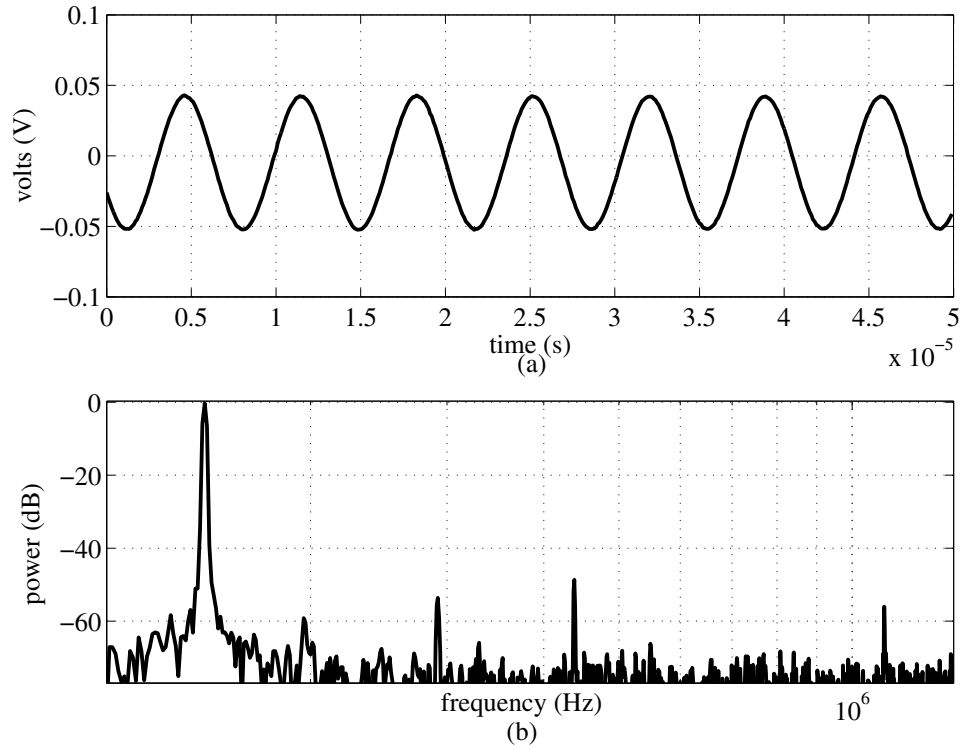


Figure 38. Oscillator output for 90mV_{pp} at 146kHz . (a) Timeseries. (b) Power spectrum. The even-order harmonics are due to input offset in the linear OTAs. THD calculated up to the 10^{th} harmonic is 0.47% . Phase noise is $-66\text{dBc}/\text{Hz}$ at a 10kHz offset.

which shows that the intrinsic offset of the differential pair has been magnified by $1/\alpha$. The effect of this magnification is so detrimental that the second harmonic has a magnitude of -55dBc . Because the distortion analysis ignored this effect, the THD equation is not all that accurate. Still, the experimental results in Fig. 37 are reasonably close to the predicted values.

The power spectrum of an ideal sinusoid should have a delta function at its oscillation frequency. As Fig. 38 shows, a physically-derived sinusoid displays some spreading in the power spectrum, resulting in ‘skirts’ around the oscillation frequency. This nonideality is normally quantified as phase noise [35]. For the operating point depicted in Fig. 38, the phase noise is $-66\text{dBc}/\text{Hz}$ at a 10kHz offset. Earlier work has provided analytical expressions for the expected phase noise of a van der Pol oscillator [36].

6.7 Low distortion sinusoidal oscillators

Although we focused on input attenuation as a form of OTA linearization, there are many other schemes that deign to linearize an OTA without an explicit attenuation stage [28, 37]. As we previously showed, one reason to do this is to avoid the input offset amplification that an attenuation stage creates. So, linear OTAs used in actual oscillators might very well not have attenuation stages at all. This fact does not make the results any less valid; all that the analysis assumes is the availability of linear OTAs and of one sigmoidally-nonlinear OTA.

For a van der Pol oscillator, the oscillation amplitude with respect to the characteristic voltage V_c is uniquely determined by ϵ , the specific implementation of $H(y)$, and the relationships among the SOS topological parameters a, b, c, d . On the other hand, THD depends only on ϵ , and not on V_c or on the SOS topology. Consequently, the only way to increase amplitude while keeping THD (*i.e.* ϵ) constant is to find a better SOS topology, to increase the value of V_c , or to change the implementation of $H(y)$. As the SOS topology may have been optimized according to some other criterion such as low noise, we will assume that it is fixed. So, the two options left for increasing oscillation amplitude are to increase V_c (for our example OTAs, this can be done by increasing the bias current when in above threshold) or to change the analytical form of $H(y)$ using, for example, bump linearization [37].

The sigmoidal function $H(y)$ of a perfectly-bump-linearized OTA is not cubic, but is rather a dominantly-fifth-order nonlinearity. An oscillator built with such an OTA, or any other OTA with a non-cubic dominant nonlinearity, would not be a van der Pol oscillator. However, it would still fall under the general description of (140) and the methods for its analysis are identical to that of the van der Pol oscillator.

Linear, undistorted sinusoidal oscillation is obtainable from a system that has a center for an equilibrium point. The problem is that the amplitude of oscillation in

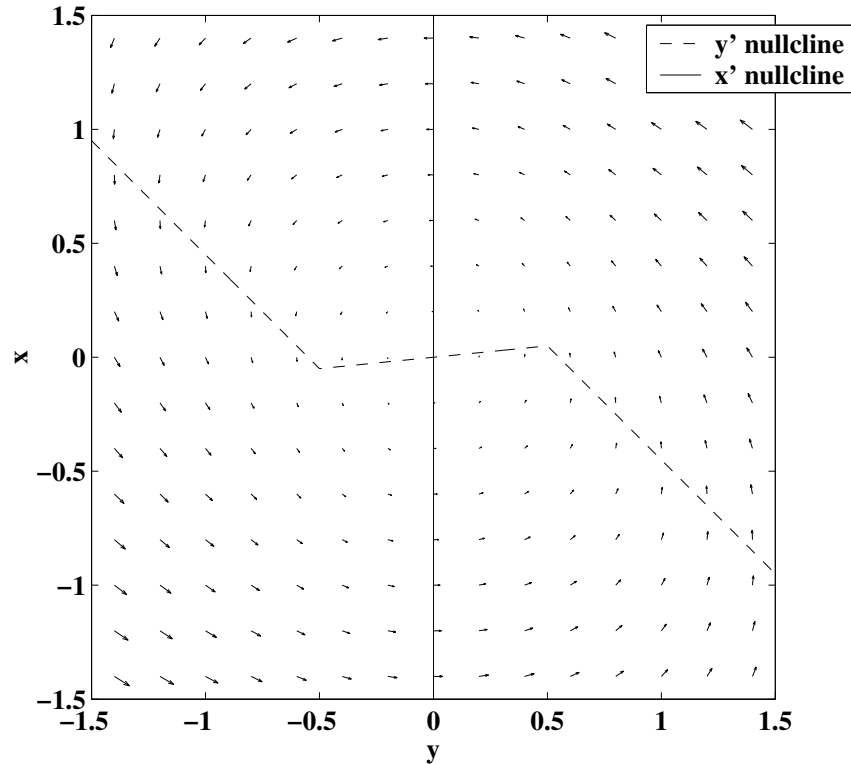


Figure 39. Phase plane portrait for the low distortion oscillator given by (203).

such a systems depends not on control parameters but on initial conditions. In addition, it is practically impossible to build a physical linear system whose equilibrium point is a center.

Instead of attempting to build a system with a center equilibrium point, we can build one that is a perturbation of such a system. Specifically, we can build a system that has a small but finite amount of damping. To ensure that the oscillations are sustained, the damping must be negative. That is, the equilibrium point is an unstable spiral.

A purely-linear system with negative damping oscillates with an exponentially-increasing amplitude. We can limit the growth of the oscillation by using an amplitude-dependent damping term that becomes positive after a given threshold amplitude. Such a damping term is used in the system whose phase plane is depicted in Fig. 39.

The system depicted is given by the following set of differential equations

$$\begin{aligned}\frac{dy}{dt} &= (a+1) \left(\frac{|y+b| - |y-b|}{2} \right) - y/Q - x \\ \frac{dx}{dt} &= y,\end{aligned}\tag{203}$$

where a , b and $Q > 0$ are control parameters. a controls the slope of the \dot{y} nullcline around the origin, while $1/Q$ is the slope of the nullcline away from the origin. The parameter b determines the break point of the piecewise-linear nonlinearity.

The oscillatory motion approaches a limit cycle in some region R via the Poincaré-Bendixon Theorem. We restate this Theorem's criteria, namely that [17]

- (1) R is a closed, bounded subset of the plane;
- (2) $\dot{\mathbf{x}} = f(\mathbf{x})$ is a continuously differentiable vector field on an open set containing R ;
- (3) R does not contain any equilibrium points; and
- (4) There exists a trajectory C that is confined in R .

To satisfy (1) and (4), we need to create a “trapping region”. Since the damping is negative at the origin, we can define the inner boundary of R to be a small ball around the origin. The outer boundary of R is simply one that is chosen large enough that the damping on it is positive. We know that the damping becomes positive for large enough y , by considering the RHS of (203) for $y \gg b$. Equation (203) becomes

$$\begin{aligned}\frac{dy}{dt} &\approx -y/Q - x \\ \frac{dx}{dt} &= y,\end{aligned}\tag{204}$$

which corresponds to the damped system $\ddot{y} + \dot{y}/Q + y = 0$ for large y .

Thus, all trajectories on the boundary of R are pointing into R . It is therefore a trapping region. Further, the only equilibrium point of the system, the origin, is not in R , meeting condition (3). Claiming the usual assumptions of smoothness, there therefore exists a limit cycle in R . Notice that, with the indicated choice of damping

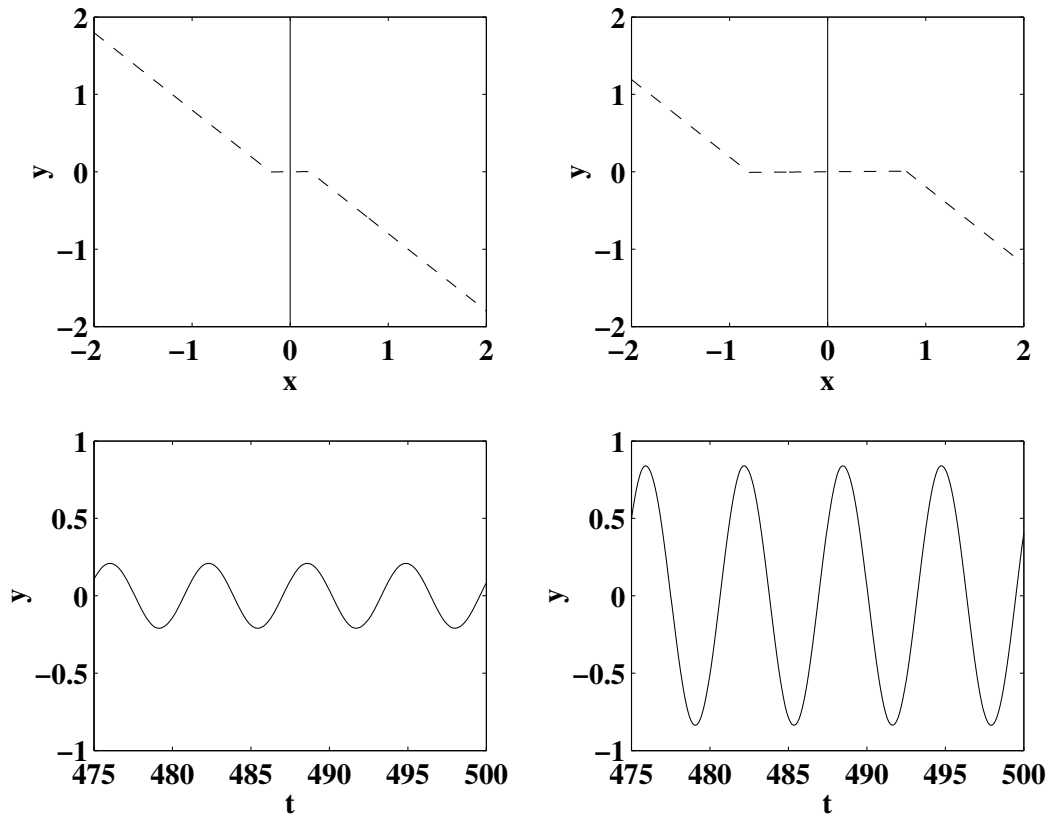


Figure 40. Amplitude control of low distortion oscillator. The phase plane portrait for the system given by (203) is depicted. The amplitude is increased by changing the break points of the pwl curve. The increase in amplitude is not accompanied by any increase in distortion.

term, the system also satisfies the conditions of Liénard equation. Thus, we have the stronger result that the limit cycle exists and is unique.

What introduces distortion to the oscillation? Recall that, for zero distortion, the equilibrium point would have to be a center. Hence, the amount by which the region around the origin is a perturbation off a center determines the amount of distortion. For the case of the nonlinear function of (203), the pertinent perturbation parameter is a . Maintaining this parameter at a small value ensures low distortion oscillation. The amplitude of oscillation is determined by the breakpoints of the nonlinear function. If we vary the location of the breakpoints (*i.e.* the value of b) while keeping the value of a low, then the amplitude of oscillation will be varied with no effect on the level of

distortion. Figure 40 shows that increasing the oscillation amplitude via b does not introduce distortion.

In the van der Pol oscillator implementation described earlier, the nonlinear function was given by (see (135) and (136))

$$I_{\text{out}}(V_z) = G_{\text{mL}} \left(V_z - (1 + \epsilon)V_c H \left(\frac{V_z}{V_c} \right) \right). \quad (205)$$

Assuming $H(\cdot)$ is a tanh function, the dimensionless nonlinear function can be written as $(y - (1 + \epsilon) \tanh(y))$. The perturbation from a center is ϵ and the location of the breakpoints — more properly, the maxima — is given by $\tanh^{-1} \left(\pm \sqrt{\epsilon/(1 + \epsilon)} \right)$. This dependence of both the amplitude and the perturbation on ϵ means that it is impossible to increase the oscillation amplitude without degrading the distortion performance.

If, instead of $(y - (1 + \epsilon) \tanh(y))$, we used $((1 + b_r)y - (1 + b_r + \epsilon) \tanh(y))$, then the perturbation from the center is ϵ while the maxima are located at $\tanh^{-1} \left(\pm \sqrt{\epsilon/(1 + b_r)} \right)$. Therefore, we can control the amplitude of oscillation independent of the amount of perturbation from a center, meaning that the distortion performance will not be degraded.

6.7.1 Low distortion oscillator implementation

In order to convert an SOS into an oscillator, we can follow the previously-described OTA-C oscillator synthesis methodology until (165). This time, though, we convert (165) into the Liénard equation by adding $g_h H(v_2) + g_{br} v_2$ to the v_1 dynamics. Notice that we are now adding two OTAs — one linear and the other nonlinear — to the original system. After adding these OTAs, the SOS originally described by (165) can be written as

$$\ddot{v}_2 - (a + d + cg_{br} + cg_h H'(v_2)) \dot{v}_2 + (ad - bc) v_2 = 0, \quad (206)$$

which is approximately

$$\ddot{v}_2 - (a + d + cg_{br} + cg_h) \left(1 - v_2^2/m_{\text{gh}}^2 \right) \dot{v}_2 + (ad - bc) v_2 = 0, \quad (207)$$

where m_{gh} is now defined as $H'(m_{\text{gh}}) = -(a + d + cg_{br})/(cg_{\text{h}})$.

Rescaling time as $T = \sqrt{ad - bc} \cdot \tau$ as before, and defining

$$\epsilon = (a + d + c(g_{\text{h}} + g_{br}))(ad - bc)^{-\frac{1}{2}}, \quad (208)$$

$$y = v_2/m_{\text{gh}}, \quad (209)$$

we get

$$\frac{d^2y}{dT^2} - \epsilon(1 - y^2) \frac{dy}{dT} + y = 0, \quad (210)$$

Again, we require

$$ad - bc > 0 \quad (211)$$

$$a + d < 0. \quad (212)$$

The upshot of adding $g_{\text{h}}H(v_2) + g_{br}v_2$, versus $g_{\text{h}}H(v_2)$, to the v_1 dynamics is that ϵ depends on the *average* of g_{br} and g_{h} , while the amplitude of y , via the expression $y = v_2/m_{\text{gh}}$, depends on the *ratio* of g_{br} and g_{h} (modulo $a + d$). Thus, the addition of an extra linear OTA allows for the independent control of ϵ and oscillation amplitude.

CHAPTER 7

A BANDPASS FILTER WITH INHERENT GAIN ADAPTATION FOR HEARING APPLICATIONS

The majority of hearing impairment is due to sensorineural loss, which is damage to, or loss of, hair cells in the cochlea. This condition is characterized by a reduction of perceivable dynamic range (*e.g.* in recruitment of loudness). The goal of hearing compensation in this case, be it with a hearing aid or with a cochlear implant, is to compress the normal dynamic range of hearing to compensate for the lost ability of the cochlea to adapt to the signal level [38–40].

There are a variety of compression schemes that are in common use in hearing aids. For a comparative review, see [41]. In a typical analog hearing aid, signal compression is applied uniformly on the entire audio bandwidth. However, since the patient’s loss of dynamic range is normally frequency dependent [42], it is more beneficial to employ multichannel compression. Available in DSP-based hearing aids, multichannel compression allows individual frequency bands to be tuned for specific dynamic ranges [43]. The disadvantage of this approach is the size, power and monetary cost of the digital processor.

We will favor the form of multichannel compression that is depicted in Fig. 41, but in a low-cost *analog* aid [44]. Conceptually, the hearing compensation scheme consists of two multiple-channel filters in cascade, H_n and H_d . The filter H_n mimics the normal functioning of the cochlea. The H_d filter is designed and tuned so as to provide the inverse function of the damaged cochlea. The signal $x(t)$ is thus manipulated such that the wearer perceives the original input, $s(t)$ as it would have been processed by a healthy cochlea [45]. Sound processing schemes such as this, which attempt to capture the mechanics of a biological cochlea, are probably more efficient [46] and more robust to environmental noise [47] than other algorithms.

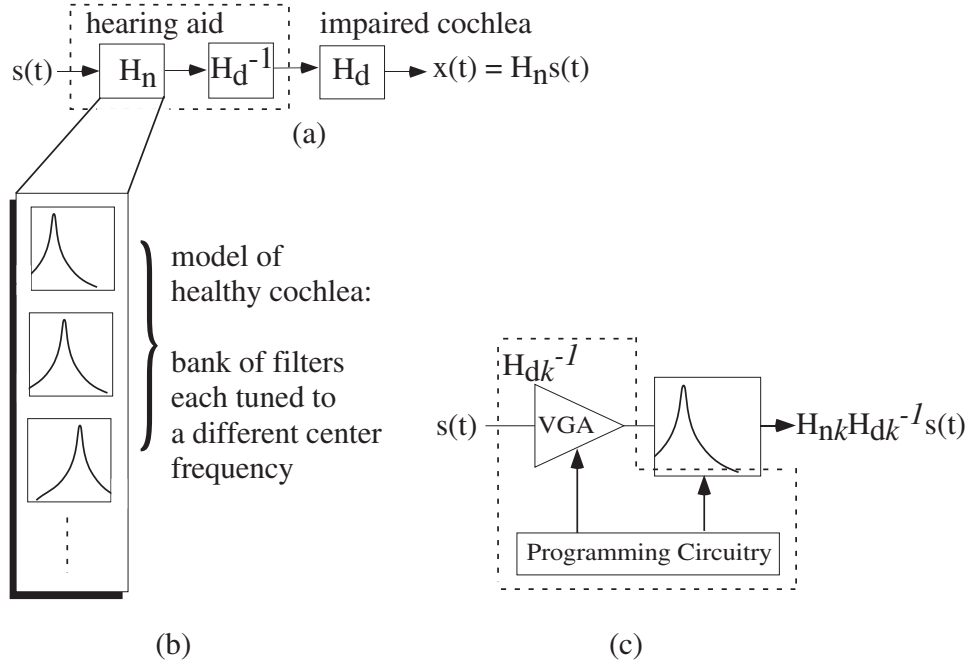


Figure 41. Multichannel compression hearing aid. (a) The damaged cochlea is modeled as a filter H_d and the healthy cochlea is modeled as a filter H_n . The hearing aid is formed from the cascade of H_n and the inverse of H_d . (b) The H_n block is a bank of nonlinear bandpass filters that performs a frequency analysis of the input signal. (c) In practice, the H_d filter reduces to parameter control of each channel in the H_n filter. For the k 'th channel in H_n , there is a corresponding set of parameters that constitute H_{dk} . VGA stands for variable gain amplifier, which is optional, but if present, can be used to set the knee point of the compression in terms of input amplitude (the compression scheme that we present here is akin to output automatic gain control [41, 48], which defines the knee point in terms of output amplitude).

Figure 41(b) shows that each channel of H_n contains a bandpass filter. The H_d portion of the hearing aid reduces to parameter settings for the bank of bandpass filters (see Fig. 41(c)). This chapter focuses on a suitable bandpass filter, which mimics pertinent local functionality of the cochlea's basilar membrane. The main challenge of the design is to keep power and area costs low enough for the filter to be of practical use in a portable hearing device. We will describe a nonlinear analog circuit approach that meets this challenge.

7.1 Implications for speech perception

Compression in hearing aids can be the source of significant distortion or artifacts. For this reason, recent research [49] suggests that the best way to use compression is

as an automatic gain control (AGC) that adapts slowly except as required to suppress sudden loud noises.¹ Most likely, this is because the gain functions that are typically used are decaying exponentials that can cause noticeable harmonic distortion. These functions are usually not memoryless and they may induce phase changes in the envelope that blur the temporal characteristics of the envelope. However, the operation of the proposed circuit is somewhat different, so following is a brief analysis of the signal characteristics in the context of hearing compensation.

We represent an acoustic signal as a sum of band-limited signals indexed by k ; each subband representation is further decomposed into a product of an envelope (which carries the instantaneous loudness information) and a rapidly-oscillating signal (or carrier) of nearly constant power. This signal representation can be applied to auditory analysis by making the signal subbands roughly equal in bandwidth to the critical bands in the ear [45, 50]. In particular, the acoustic signal, $s(t)$, is written as

$$s(t) = \sum_k e_k(t)v_k(t) \quad (213)$$

where $v_k(t)$ is a higher-frequency band-limited signal or vibration with nearly constant power; and $e_k(t)$ represents the envelope variation over time. With this representation, the loudness of the signal perceived in any particular critical band of the ear is primarily controlled by operating only on the envelope in that band.

The envelope has a well-defined bandwidth that is roughly the same as the bandwidth, f_{BW} , of $v_k(t)$. In particular, the gain is a monotonic function of the envelope and is incorporated into the bandpass filter operation so the time constant for each band is approximately $1/f_{BW}$. The fact that the gain function is monotonic has the following implications (see also Fig. 42):

1. The envelope at the output of the filters, $\hat{e}_k(t)$ has the same general shape as $e_k(t)$ with only a change in dynamic range;

¹For such a system, the perceived distortion is minimal because the slow adaptation is not very perceptible while the fast attack may be masked by the sound that caused it.

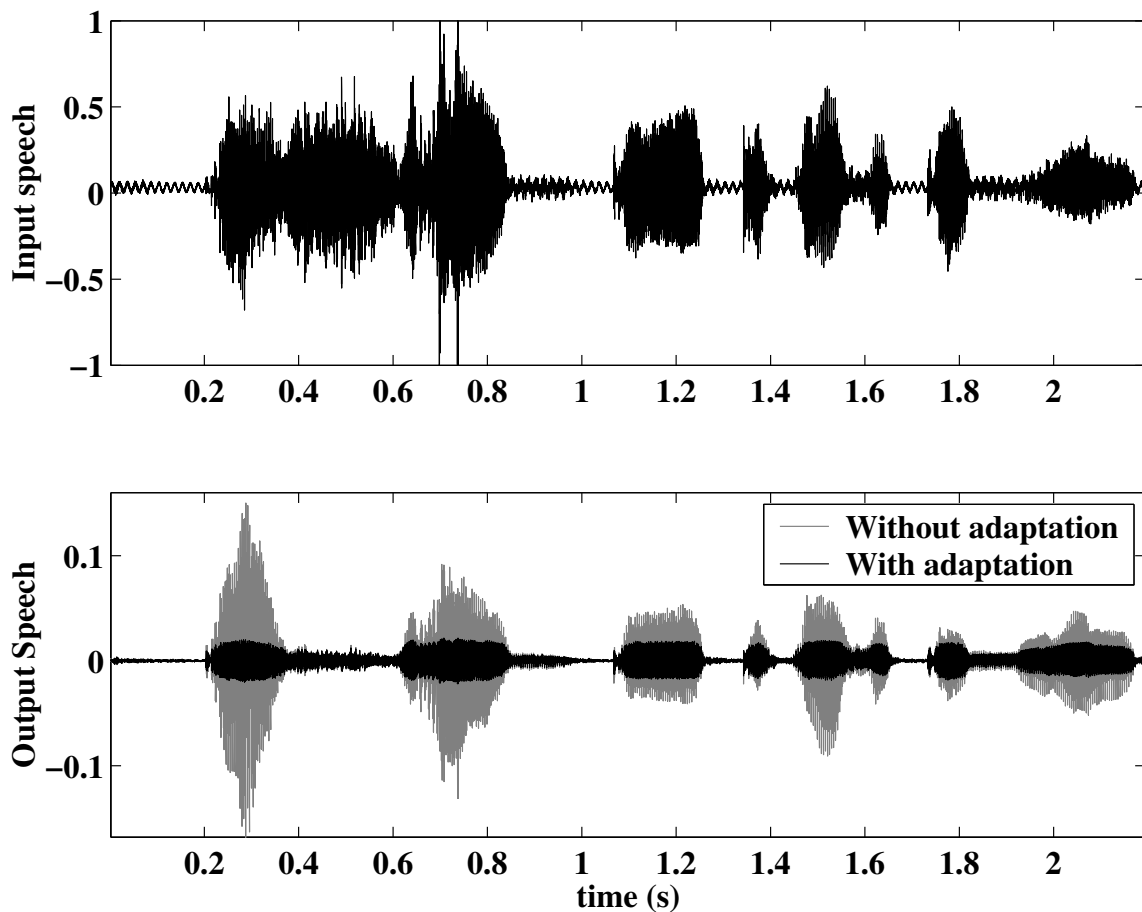


Figure 42. Simulation results for a single band of speech processing. The upper panel is the original input speech. The lower panel is the processed speech for a single band. The black area is speech compressed with the scheme that we will describe shortly. After compression, the general shape of the signal's envelope is maintained, but with a reduction in dynamic range.

2. the output signal is in phase with the input signal—that is, the phase of $\hat{s}_k(t)$ is the same as that of $s_k(t)$ and if they were overlaid they would line up, the only difference being in the amplitude; and
3. temporal cues are preserved because of items 1 & 2 and because $v_k(t)$ is preserved.

Note, while the gain applied to the envelope does not smear or destroy temporal cues they may be slightly diminished as their dynamic range is diminished. This is to be expected since the audible dynamic range of the listener is diminished. However, this has been shown to provide an improvement in speech reception, especially in noise [51, 52]. Note that the healthy cochlea too adapts its critical-frequency gain at a rate that is on the order of one period of the input signal [53].

Finally, care must be taken so that the high-Q bandpass filters do not ring too long and cause temporal smearing. This is not an issue for moderate Q values. For example, a filter with a center frequency of 1kHz and $Q = 5$ yields 1.6 msec of ringing when measured to the 3dB point and after 4 msec, the ringing has attenuated by over 20dB. Thus, the ringing is much shorter than even a short speech phoneme, meaning that it is perceptually insignificant. However, we would like to have Qs that are high enough to reflect the cochlea’s sharp frequency-selectivity [54]. The solution is to create high-order filters that exhibit sharp frequency selectivity without excessive ringing. While we will focus on a second-order filter, we can readily achieve higher orders simply by cascading multiple filters per channel.

7.2 Filter description and architecture

The cochlea can be modeled as a bank of filters that performs a frequency analysis on input signals. The frequency response of a particular basilar membrane site is shown in Fig. 43. For small-amplitude inputs, each filter has a narrow passband around a resonant frequency. As the input signal energy in a particular bandwidth increases,

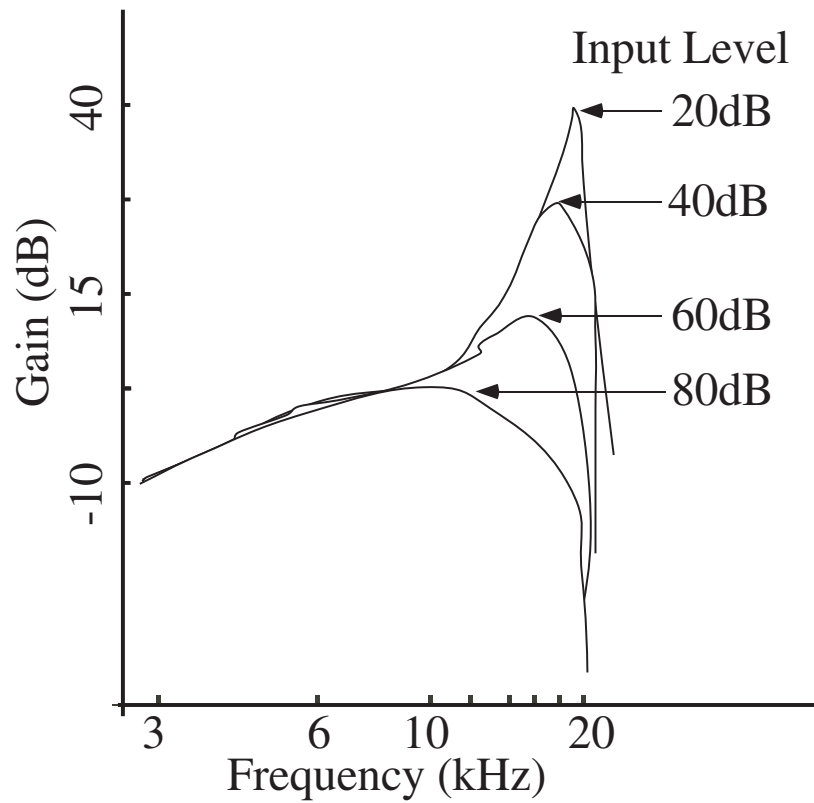


Figure 43. Basilar membrane site measurements at four sound pressure levels, adapted from [54]. The gain is calculated as the ratio between basilar membrane displacement and sound pressure level.

the passband of the corresponding filter widens and its center frequency gain reduces. In effect, each filter exhibits a band-limited nonlinear response around its resonant frequency [55]. It is through this nonlinearity that the healthy cochlea is able to compress a wide input dynamic range into a much smaller internal one.

7.2.1 Design approach I: Linearizing about the equilibrium point

We will implement the cochlear's gain compression as a second-order bandpass filter with an amplitude-dependent quality (Q) factor. Figure 44 show the desired frequency response and step response of such a filter to various levels of input amplitude.

Recall that the response of

$$\dot{\mathbf{x}} = F(\mathbf{x}, u), \quad (214)$$

to a step input of size A_{in} is defined as the solution to

$$\dot{\mathbf{x}} = F(\mathbf{x}, A_{\text{in}}). \quad (215)$$

From Fig. 44, the response to a small-amplitudes step input is underdamped, while the response to a large-amplitude step is overdamped. We can elicit such behavior from (214) by choosing a system whose equilibrium point type changes from spiral (underdamped) for small-amplitude steps to nodal (overdamped) for large-amplitude steps. Following is a description of the design procedure.

Assume (214) is a second-order system, and that it is nonlinear only in x_1 and the input u . Specifically, define (214) as

$$\begin{bmatrix} \dot{x}_1 \\ \dot{x}_2 \end{bmatrix} = \begin{bmatrix} f(x_1, u) - x_2 \\ x_1 \end{bmatrix}, \quad (216)$$

Keeping the x_2 terms linear ensures that, for moderate values of quality factor, the center frequency of the filter remains fixed, regardless of input amplitude. Equation (216) has the following response to a step input of amplitude A_{in}

$$\begin{bmatrix} \dot{x}_1 \\ \dot{x}_2 \end{bmatrix} = \begin{bmatrix} f(x_1, A_{\text{in}}) - x_2 \\ x_1 \end{bmatrix}. \quad (217)$$

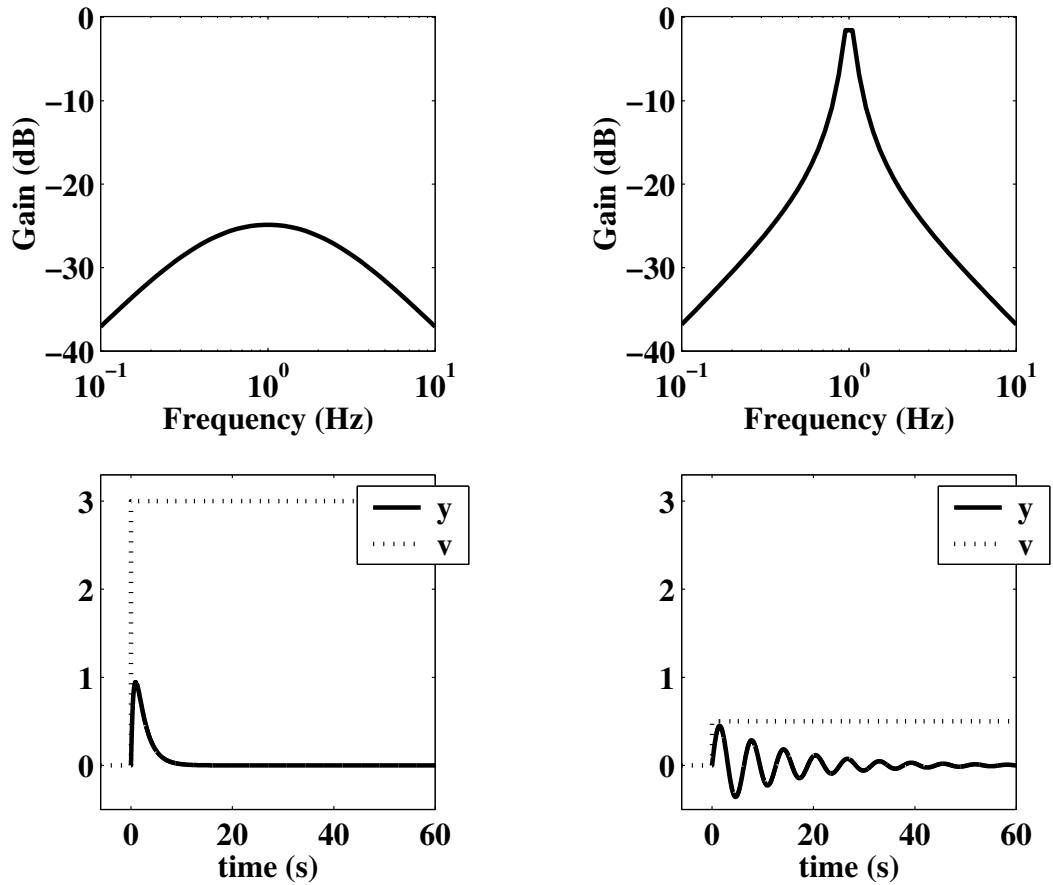


Figure 44. Desired frequency response and step response of nonlinear filter. The panels on the top row illustrate the desired frequency response of the filter. For an input amplitude of 3 units, the top left panel shows a frequency response with a flat pass band. An input amplitude of 0.1 — ostensibly a “small” amplitude for the purpose of illustration — elicits the frequency response of the top right panel, which has sharp Q-peaking. The panels in the bottom row illustrate the desired step response of the filter. For an input amplitude of 3 units, the bottom left panel shows a damped step response. An input amplitude of 0.1 elicits the step response of the bottom right panel, which shows an underdamped, ringing response.

Assuming $f(x_1, A_{\text{in}})$ is a single-valued function of x_1 , (217) has a unique equilibrium point, given as

$$(x_1^*, x_2^*) = (0, f(0, A_{\text{in}})). \quad (218)$$

The linearization of (217) is

$$\begin{bmatrix} \dot{x}_1 \\ \dot{x}_2 \end{bmatrix} = \begin{bmatrix} \partial f(x_1, A_{\text{in}})/\partial x_1 & -1 \\ 1 & 0 \end{bmatrix} \begin{bmatrix} x_1 \\ x_2 \end{bmatrix}. \quad (219)$$

Evaluating the Jacobian at (x_1^*, x_2^*) , we find that the determinant is $\Delta = 1$ and the trace is $\tau = \partial f(x_1, A_{\text{in}})/\partial x_1|_{x_1=0}$. Applying the techniques from Chapter 3, we note that the equilibrium point is a stable spiral if

$$-2 < \left. \frac{\partial f(x_1, A_{\text{in}})}{\partial x_1} \right|_{x_1=0} < 0, \quad (220)$$

and a stable node if

$$\left. \frac{\partial f(x_1, A_{\text{in}})}{\partial x_1} \right|_{x_1=0} < -2. \quad (221)$$

In order to elicit the adaptive Q behavior, the task now is to find a nonlinear function $f(\cdot)$ such that

$$-2 < \left. \frac{\partial f(x_1, A_{\text{in}})}{\partial x_1} \right|_{x_1=0} < 0, \quad A_{\text{in}} < A_{\text{th}} \quad (222)$$

and

$$\left. \frac{\partial f(x_1, A_{\text{in}})}{\partial x_1} \right|_{x_1=0} < -2, \quad A_{\text{in}} \geq A_{\text{th}}, \quad (223)$$

where A_{th} is some appropriately-defined threshold amplitude. Note that $\partial f(x_1, A_{\text{in}})/\partial x_1|_{x_1=0}$ corresponds to the quality factor (Q).

To simplify the problem, consider a nonlinear function of the form

$$f(x_1, u) = g(x_1 + u). \quad (224)$$

Then, we can write

$$\left. \frac{\partial f(x_1, A_{\text{in}})}{\partial x_1} \right|_{x_1=0} = \left. \frac{dg(y)}{dy} \right|_{z=(x_1^*+A_{\text{in}})} = \left. \frac{dg(y)}{dy} \right|_{y=A_{\text{in}}},$$

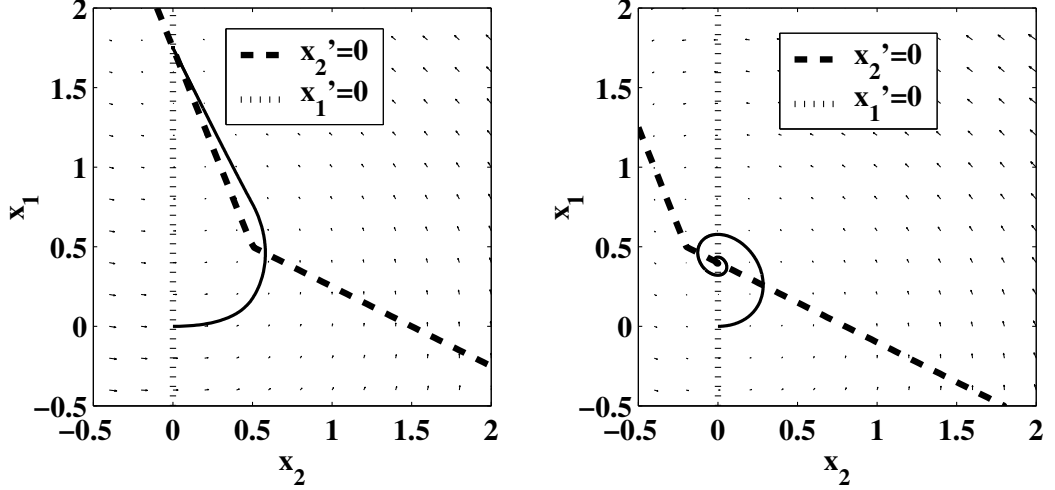


Figure 45. Phase plane portrait for potential cochlear model. The phase portraits depicted are for the step response of the system of (216) with $f(x_1, u)$ given by $g(x_1 + u)$, where $g(x_1 + u)$ is the nonlinear function of (227) for $m = -2.5$ and $A_{th} = 1$. The panel on the left is the phase portrait for the step response when the input step is at an amplitude of 1.5, while the panel on the right is for an input step of 0.8.

and Equations (222) and (223) become

$$-2 < \left. \frac{dg(y)}{dy} \right|_{y=A_{in}} < 0, \quad A_{in} < A_{th}, \quad (225)$$

and

$$\left. \frac{dg(y)}{dy} \right|_{y=A_{in}} < -2, \quad A_{in} \geq A_{th}. \quad (226)$$

The piecewise-linear function

$$g(y) = my + |y + A_{th}| - |y - A_{th}|, \quad (227)$$

is a simple example that satisfies (225) and (226), as long as $-4 < m < -2$.

Figure 45 depicts the phase portrait of (217), with $f(x_1, A_{in}) = g(x_1 + A_{in})$ given by the pwl function of (227) for $m = -2.5$ and different values of A_{in} . When $A_{in} < A_{th}$, the nullclines intersect at the shallow portion of $g(x_1 + A_{in})$. That is, $-2 < dg/dy|_{y=A_{in}} < 0$ and the equilibrium point is a spiral. For $A_{in} \geq A_{th}$, the $x_1 = 0$ nullcline shifts such that the equilibrium point occurs at the steep portion of $g(x_1 + A_{in})$. That is, $dg/dy|_{y=A_{in}} < -2$, and the equilibrium point is now a node. The same information of Fig. 45 is depicted in Fig. 46 as a time domain plot.

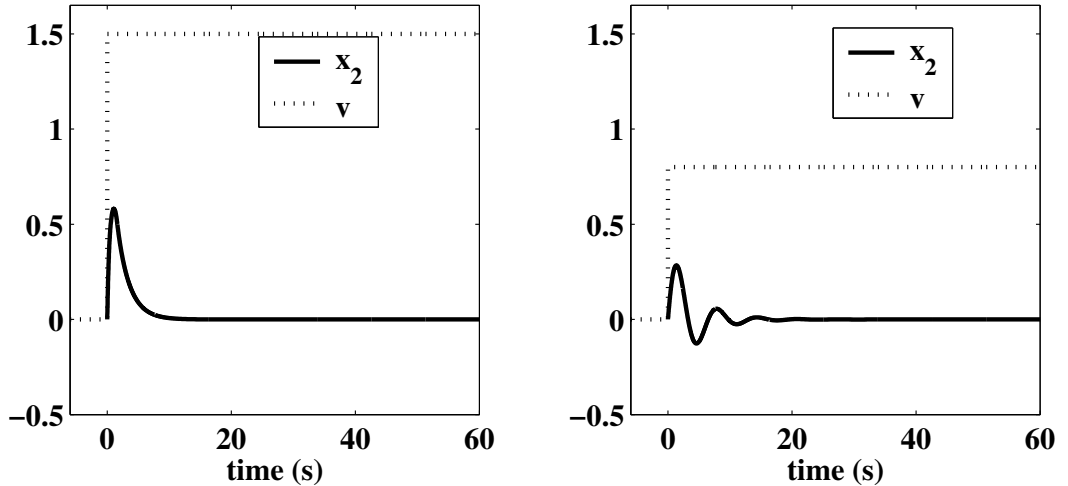


Figure 46. Step response for potential cochlear model, with pwl nonlinearity. The step responses depicted are for the system of (216) with $f(x_1, u)$ given by $g(x_1 + u)$, where $g(x_1 + u)$ is the nonlinear function of (227) for $m = -2.5$. The panel on the left is the step response when the input step is at an amplitude of 1.5, while the panel on the right is for an input step of 0.8.

Were the nonlinear function to be actually implemented as a piecewise linear function, the filter would suffer unwanted distortion from the discontinuous derivative. In addition, it would not exhibit the continuously-varying amount of Q-adaptation that is desired in the hearing aid. For these reasons, we replace the piecewise linear function with a smoother function that also meets the conditions of (227). These conditions merely define a nonlinear function with an increasing gradient. So, any expansive nonlinearity will do. For instance,

$$g(y) = my + 2 \tanh(y) \quad (228)$$

is a suitable function. With this particular choice of $g(y)$ the filter equation is

$$\begin{bmatrix} \dot{x}_1 \\ \dot{x}_2 \end{bmatrix} = \begin{bmatrix} 2 \tanh(x_1 + u) - m(x_1 + u) - x_2 \\ x_1 \end{bmatrix}. \quad (229)$$

Figure 47 shows the dependence of the filter's step response to input amplitude. The quality factor does indeed appear to reduce with increasing input amplitude, as desired. We run into trouble when we consider the frequency response of this

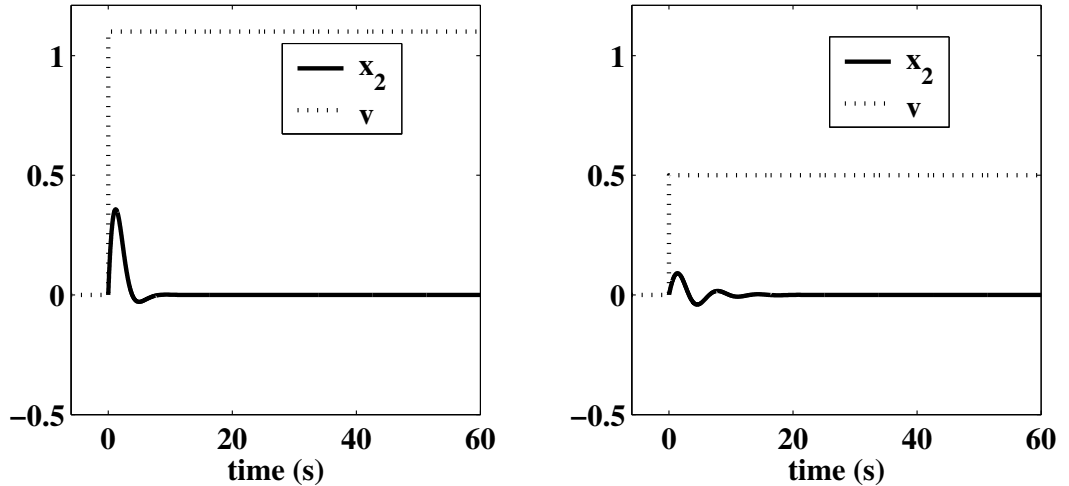


Figure 47. Step response for potential cochlear model, with continuously-differentiable nonlinearity. The step responses depicted are for the system of (216) with $f(x_1, u)$ given by $g(x_1 + u)$, where $g(x_1 + u)$ is the nonlinear function of (228) for $m = -2.1$. The panel on the left is the step response when the input step is at an amplitude of 1.1, while the panel on the right is for an input step of 0.5.

filter, shown in Fig. 48. First of all even though the quality factor reduces with input amplitude, the gain remains fairly constant. Also, the output is significantly distorted. These two effects are due to including the input u in the nonlinearity. Recall that the original problem (see Fig. 44) called only for the quality factor to be nonlinear. The current design involves both a nonlinear quality factor and a nonlinear gain. In the next section, we will describe a different approach that avoids this unwanted nonlinearity.

7.2.2 Design approach II: transition layer problem

Given the results of the previous section, we will now consider implementing a filter where the only argument to the nonlinear function is the x_1 state variable, as such

$$\begin{bmatrix} \dot{x}_1 \\ \dot{x}_2 \end{bmatrix} = \begin{bmatrix} f(x_1) - x_2 + u \\ x_1 \end{bmatrix}. \quad (230)$$

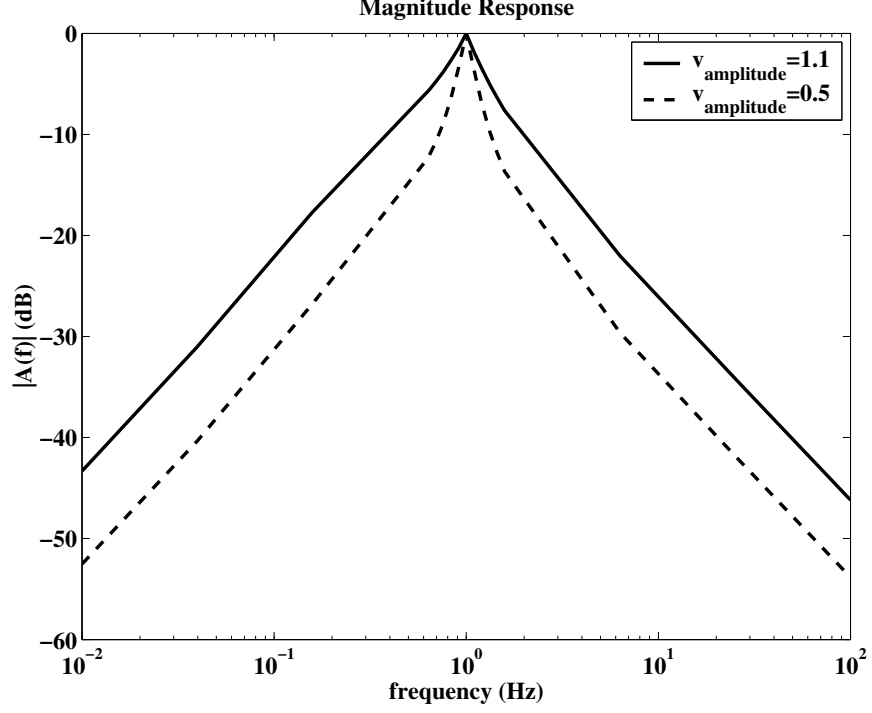


Figure 48. Frequency response for potential cochlear model, with continuously-differentiable nonlinearity. The frequency responses depicted are for the system of (216) with $f(x_1, u)$ given by $g(x_1 + u)$, where $g(x_1 + u)$ is the nonlinear function of (228) for $m = -2.1$. The input amplitudes are 1.1 and 0.5.

The response of this filter to a step of amplitude A_{in} is

$$\begin{bmatrix} \dot{x}_1 \\ \dot{x}_2 \end{bmatrix} = \begin{bmatrix} f(x_1) - x_2 + A_{\text{in}} \\ x_1 \end{bmatrix}. \quad (231)$$

Notice from the linearization

$$\begin{bmatrix} \dot{x}_1 \\ \dot{x}_2 \end{bmatrix} = \begin{bmatrix} \partial f(x_1)/\partial x_1 & -1 \\ 1 & 0 \end{bmatrix} \begin{bmatrix} x_1 \\ x_2 \end{bmatrix}, \quad (232)$$

that the type of equilibrium point is independent of input amplitude. As such, we cannot apply the idea of changing equilibrium point type that we used in the previous design approach.

Instead, we proceed by observing the effect of different input step sizes on the

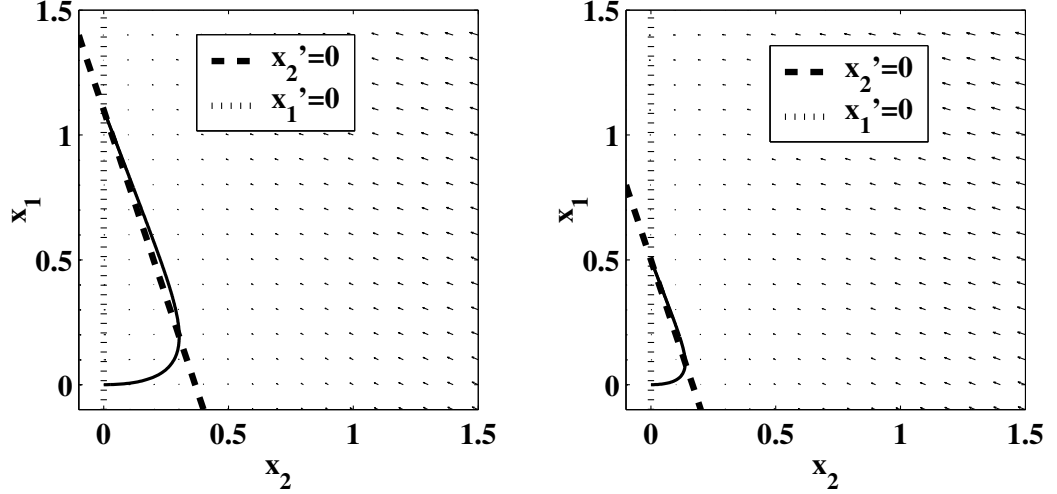


Figure 49. Phase portrait for for step response of system of (233). The input step amplitude for the plot on the left is 1.1, while that of the one on the right is 0.5. The equilibrium point, identified as the intersection of the nullclines, shifts farther and farther away from the origin for larger and larger step input amplitude sizes.

phase plane. Consider the step response of the following linear filter

$$\begin{bmatrix} \dot{x}_1 \\ \dot{x}_2 \end{bmatrix} = \begin{bmatrix} -3x_1 - x_2 + u \\ x_1 \end{bmatrix}, \quad (233)$$

with initial conditions $x_1(0) = x_2(0) = 0$. As the phase plane plots of Fig. 49 show, the larger the input step amplitude A_{in} , the farther the equilibrium point is from the initial conditions. We can therefore create a nonlinear filter whose local behavior varies with distance from the equilibrium point.

Essentially, this design approach is an inversion of the normal transition layer problem. That is, we will define the inner and outer layer solutions and then find a system to which these solutions correspond.

We will refer to the region that is in the vicinity of the equilibrium point as the inner layer. The region that is far from the equilibrium point is the outer layer. A large amplitude input step places the system in the outer layer, where we desire a damped response. On the other hand, a small amplitude input step places the system in the inner layer, where we desire an underdamped response. To formalize this

idea, consider the nonlinear filter step response, (231), under the change of variable $z_2 = x_2 - A_{\text{in}}$. It becomes

$$\begin{bmatrix} \dot{x}_1 \\ \dot{z}_2 \end{bmatrix} = \begin{bmatrix} f(x_1) - z_2 \\ x_1 \end{bmatrix}, \quad (234)$$

with initial conditions $x_1 = x_1^*$, $z_2 = x_2^* - A_{\text{in}}$. Thus, the effect of a step input of amplitude A_{in} is to shift the initial condition by A_{in} . Thus, a large input step places the system far from the origin and effectively in the outer layer. A small input step keeps the system close to the origin and in the inner layer.

In the outer layer, we would like $f(x_1)$ to be such that the system is damped. At the origin, and in the inner layer, $f(x_1)$ should be such that the system is underdamped. These constraints are enumerated as

- 1) $f(x_1, \epsilon)|_{\epsilon=0} = \frac{x_1}{Q_u}$,

- 2) in the ‘‘small amplitude’’ layer, $\lim_{\epsilon \rightarrow 0} f(x_1, \epsilon) = \frac{x_1}{Q_u}$,

- 3) in the ‘‘large amplitude’’ layer, $\lim_{\epsilon \rightarrow 0} f(x_1, \epsilon) = \frac{x_1}{Q_d}$,

- 4) in order for (3) to occur while $f(x_1)$ still satisfies (1) and (2), the thickness of the ‘‘small amplitude’’ layer must follow $\lim_{\epsilon \rightarrow 0} d(\epsilon) = 0$.

The parameters Q_u and Q_d represent underdamped and damped values, respectively, of the filter’s quality factor.

A function that satisfies $\lim_{\epsilon \rightarrow 0} f(x_1, \epsilon) = x_1/Q_u$ is $f(x_1, \epsilon) = x_1/Q_u$. A function that satisfies $\lim_{\epsilon \rightarrow 0} f(x_1, \epsilon) = x_1/Q_d$ is $f(x_1, \epsilon) = x_1/Q_d$. So, we have

$$f(x_1, \epsilon) \approx \frac{x_1}{Q_u}, \quad |x_1| < d(\epsilon)/2 \quad (235)$$

$$\approx \frac{x_1}{Q_d}, \quad |x_1| \geq d(\epsilon)/2, \quad (236)$$

where we are assuming that $f(x_1, \epsilon)$ is even symmetric.

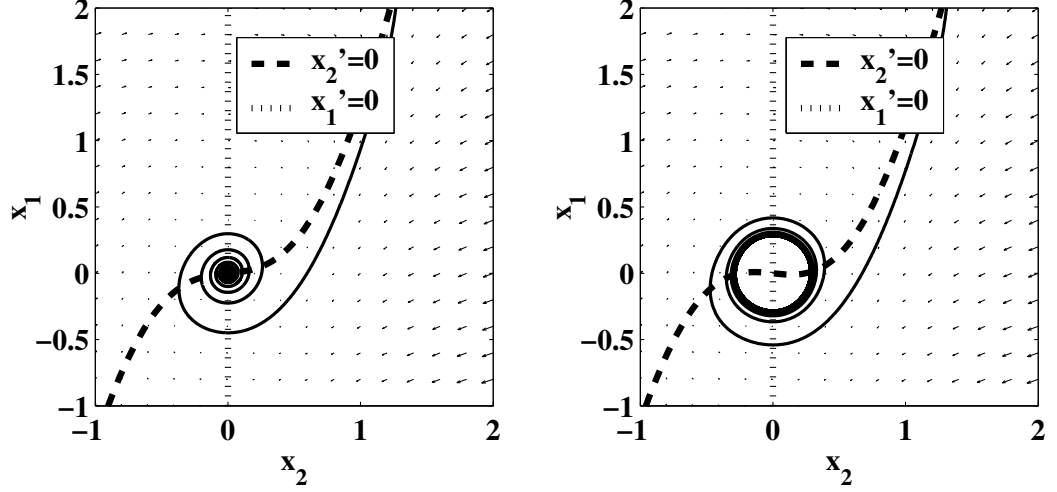


Figure 50. Supercritical Hopf bifurcation in nonlinear bandpass filter. The phase plane portraits shown are for the step response of the system of (230) with $f(x_1)$ given by (238). The parameter values are $\epsilon = 1$, $Q_d = 0.2$ and (a) $Q_u = 10$ and (b) $Q_u = -10$.

For simplicity, say $d(\epsilon) = 2\epsilon$. Then, if we join the inner layer and the outer layer with a piecewise-linear curve we end up with a function $f(x_1, \epsilon)$ given by the equation

$$f(x_1, \epsilon) = -\frac{x_1}{Q_d} + \left(\frac{1}{2Q_d} - \frac{1}{2Q_u} \right) (|\epsilon + x_1| - |\epsilon - x_1|). \quad (237)$$

Similar to the other design approach, we will replace this pwl function with a smoother one, namely

$$f(x_1, \epsilon) = -\frac{x_1}{Q_d} + \epsilon \left(\frac{1}{Q_d} - \frac{1}{Q_u} \right) \tanh \left(\frac{x_1}{\epsilon} \right). \quad (238)$$

7.2.2.1 Instability due to bifurcation

The nonlinear function of (238) can be implemented using one linear OTA in parallel with a nonlinear one, to give

$$I(V_1) = -G_d \cdot V_1 + G_{ud} \cdot V_c \tanh \left(\frac{V_1}{V_c} \right), \quad (239)$$

where the nonlinear OTA is assumed to be based on a subthreshold differential pair (see Chapter 6). The voltage V_c is a characteristic voltage, as defined in Chapter 6.

Also, the OTA transconductance gains are related to Q_d and Q_u via

$$\frac{1}{Q_d} \sim G_d \quad (240)$$

$$\frac{1}{Q_u} \sim G_{ud} - G_d. \quad (241)$$

The problem we run into is due to $1/Q_u$ depending on the difference of OTA transconductance gains. Ideally, we want $1/Q_u$ to be positive. However, poorly-matched components may result in this being a negative value. As it turns out, the system of (230), with $f(x_1)$ defined as (238), will undergo a supercritical Hopf bifurcation as Q_u passes through 0. Figure 50 shows the phase plane plots of the system for $1/Q_u = 0.1$ and $1/Q_u = -0.1$. As shown, for $1/Q_u = -0.1$, the equilibrium point is now unstable and the system now displays an attracting limit cycle.

Proper circuit design will avoid the problem of potential instability. However, this difficulty can be completely eliminated if, instead of (238), the pwl curve of (237) is approximated by a simple expansive transconductance function. The rest of the chapter will develop along the lines of implementing the nonlinear function as such.

7.2.3 Description of implemented filter

The bandpass filter that will be described is an operational transconductance amplifier-capacitor (OTA-C) circuit that exhibits Q-peaking for small signals. An OTA-C circuit is normally operated within the linear range of all of the OTAs. In this case, we will deliberately employ nonlinearity in one of the amplifiers in order to evoke the cochlea's compressive behavior. The transconductance gain² of the nonlinear amplifier increases with input amplitude. The filter is designed so that its damping coefficient is directly controlled by the nonlinear amplifier's transconductance gain. As such, the amount of Q-peaking reduces with increasing input amplitude.

²We define a transconductance function as one whose arguments are in units of Volts, and that is itself in units of Amperes. By contrast, a *transconductance gain*, with units of Ampere/Volts, is the derivative of the transconductance function with respect to input voltage. Further, the *small-signal transconductance gain* is the constant term of the transconductance gain.

The bandpass filter is based on the circuit of Fig. 51. It has a first-order roll off at a center frequency of

$$w_0 = \sqrt{\frac{G_H G_L}{C_L(C_1 + C_w)}}, \quad (242)$$

while the quality-factor is nominally

$$Q = \sqrt{\frac{C_L G_H}{(C_1 + C_w) G_L} \left(\frac{1}{1 + G_N/G_L} \right)}, \quad (243)$$

and the center frequency gain is

$$A_{w_0} = C_1/(C_1 + C_w). \quad (244)$$

C_1 , C_w , C_L are drawn capacitances and G_H , G_L , G_N are transconductance gains.

The OTAs labelled G_H and G_L are linear, meaning that they have a constant transconductance gain. The amplifier labeled G_N , on the other hand, has a level-dependent transconductance gain, which is of the general form

$$G_N = f(\tilde{V}_{\text{out}}), \quad (245)$$

where \tilde{V}_{out} is the energy of V_{out} , and $f(\cdot)$ is a symmetric monotonically-increasing function. Substituting (245) into (243), we see that the quality factor is not constant, but is dependent on \tilde{V}_{out} . Specifically, Q decreases with increasing levels of \tilde{V}_{out} . The simplest form of $f(\cdot)$ is a quadratic function of V_{out} , which would represent the instantaneous energy of the output voltage. The non-constant transconductance gain is

$$G_N = N(1 + \alpha(V_{\text{out}})^2/U_T^2), \quad (246)$$

where N is some programable constant, U_T is the thermal voltage, and α is a coefficient to be determined.

7.3 Amplifier implementations

This subsection presents a description of the circuit implementation of the various amplifiers used in the OTA-C bandpass filter.

input common-mode voltage may push either of the differential-pair transistors or the tail transistor out of saturation. We deal with all three sources of distortion by employing capacitive attenuation at the differential-pair inputs, as shown in Fig. 52.

The OTA input is attenuated by a factor of $M + 1$ before being applied to the differential pair. A large value of M ensures that the differential-pair input will never vary enough to alter the transconductance gain significantly.

The input nodes of the differential pair have no DC path to ground, meaning that, under normal operating conditions, any charge stored on them is nonvolatile. However, we can use the high-field phenomena of hot-electron injection and Fowler-Nordheim tunneling to change the amount of charge that is stored on these nodes [58]. In particular, we can modify the amount of stored charge so as to compensate for the amplifier's offset. Consider an input offset of V_{offset} and a difference in charge on the differential-pair input nodes of Q_{offset} , as shown in Fig. 52. We set the difference in charge to satisfy

$$Q_{\text{offset}} = V_{\text{offset}} C_{\text{in}} (M + 1), \quad (247)$$

which effectively removes the offset.

From Fig. 52, the common-mode input voltage, V'_{cm} of the differential pair is

$$V'_{\text{cm}} = \frac{Q}{C_{\text{in}}(M + 1)} + \frac{V_{\text{cm}}}{M + 1}. \quad (248)$$

We adjust the value of Q to ensure that the differential-pair and tail transistors are always in saturation.

Employing injection and tunneling the way we do precludes the need for a high-impedance-based biasing scheme, which would actually increase distortion at the low frequencies [59]. As we will see in the experimental results section, precise control of the floating-node charges results in a significant lowering of distortion.

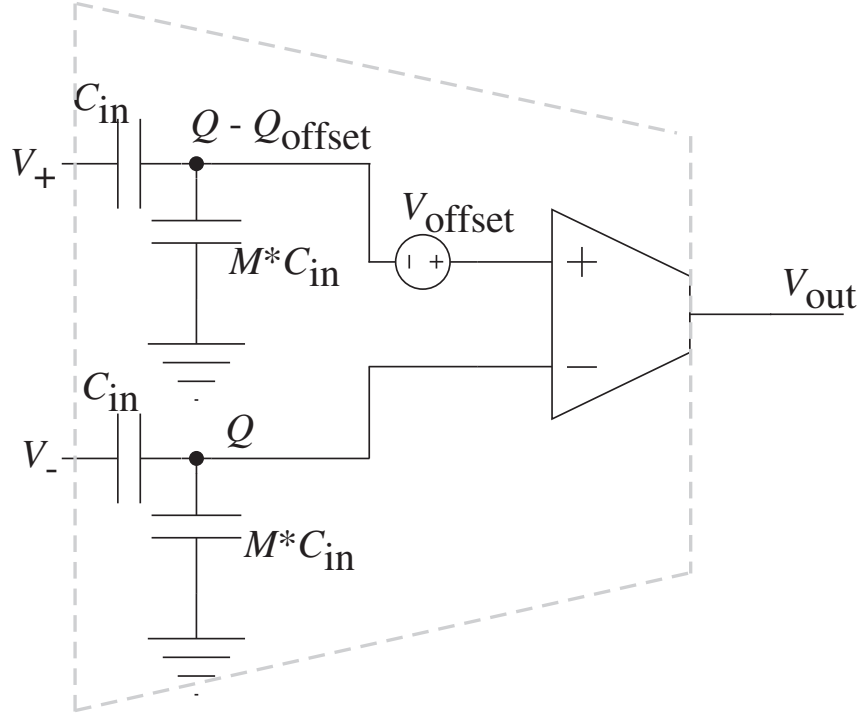


Figure 52. Highly linear OTA. The inputs to a simple OTA are attenuated via capacitive division. Injection and tunnelling (through tunnelling capacitors, not shown) are used to precisely control the amount of charge on the floating nodes.

7.3.2 Nonlinear amplifier

The gain of (246) is provided by an amplifier with the following nonlinear transfer function

$$I_{GN} = N(V_{\text{out}} + \alpha(V_{\text{out}})^3/3U_T^2), \quad (249)$$

which we implemented with the circuit shown in Fig. 53(a). For the purpose of analysis, we will assume that the transistors in this circuit are operated in subthreshold. The circuit's behavior is similar for above-threshold operation, but its analysis would require a more complex transistor model that is valid in all regions of operation. So, assuming that the bias voltages V_n and V_p ensure subthreshold operation, the nMOS and pMOS drain currents are, respectively,

$$I_n = I_1 e^{\kappa_n V_n / U_T} e^{-V_{\text{out}} / U_T} \quad (250)$$

$$I_p = I_2 e^{-\kappa_p V_p / U_T} e^{V_{\text{out}} / U_T}, \quad (251)$$

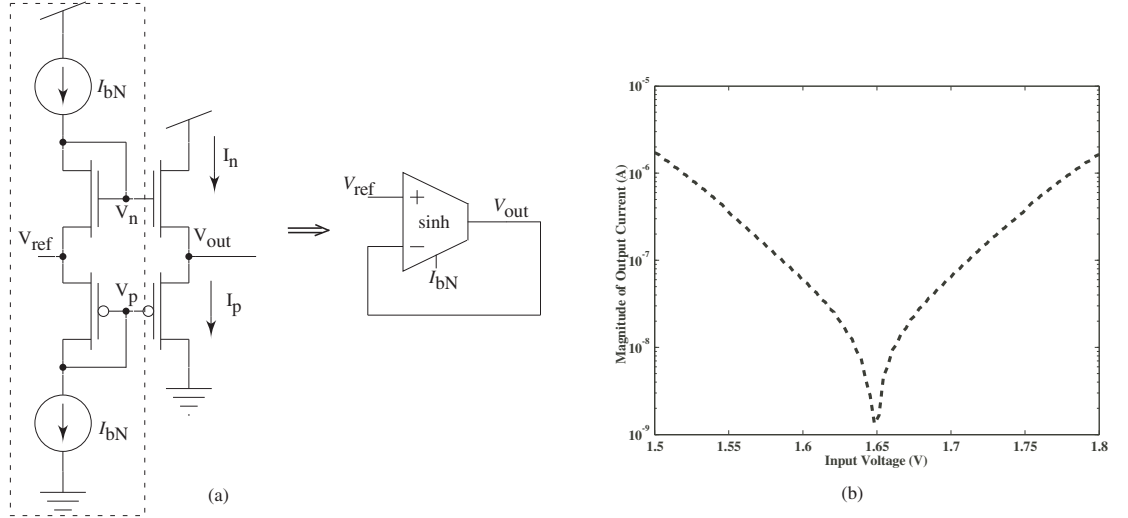


Figure 53. Nonlinear amplifier. (a) Circuit implementation. V_n and V_p are fixed voltages that are set by the bias circuitry shown in the dashed box. The output node is V_{out} . The output current is $I_n - I_p$. **(b) Experimental current-voltage curve.** When the V_{out} voltage is swept, the magnitude of the output current displays a logarithmic trend for large values of $V_{out} - V_{ref}$, which is characteristic of the sinh function.

where $I_{1,2}$ are pre-exponential current terms that depend largely on device dimensions and doping concentrations, and $\kappa_{n,p}$ are the body-effect coefficients.

Defining V_{ref} and I_{bN} as

$$V_{ref} = (U_T \log(I_1/I_2) + (\kappa_n V_n + \kappa_p V_p)) / 2 \quad (252)$$

$$I_{bN} = 2\sqrt{I_1 I_2} e^{(\kappa_n V_n - \kappa_p V_p) / U_T}, \quad (253)$$

we can write the output as

$$\begin{aligned} I_n - I_p &= I_{bN} (e^{(V_{ref} - V_{out}) / U_T} - e^{(V_{out} - V_{ref}) / U_T}) / 2 \\ &= -I_{bN} \sinh((V_{out} - V_{ref}) / U_T), \\ &\approx \frac{-I_{bN}}{U_T} ((V_{out} - V_{ref}) + (V_{out} - V_{ref})^3 / 6U_T^2), \end{aligned} \quad (254)$$

which is equivalent to (249) if we associate $-I_{bN}/U_T$ with N , set $\alpha = 1/2$ and define V_{ref} as the reference voltage. Notice that (254) resembles the transfer function of a transconductance amplifier with inputs V_{out} , V_{ref} and a bias current of I_{bN} . We

therefore model the nonlinear transconductor as an amplifier in negative feedback, as shown in Figs. 51 and 53(a).

7.4 Circuit analysis

Since the filter involves an explicit nonlinearity, the classical small-signal paradigm is inadequate for performing any rigorous analysis. Instead, we employ tools from nonlinear dynamical systems theory to understand its behavior.

7.4.1 Quality factor adaptation

Applying KCL to both nodes of Fig. 51, we write

$$\begin{aligned} C_L \frac{dV_{\text{out}}}{dt} &= G_L(V_x - V_{\text{out}}) - I_{\text{bN}} \sinh\left(\frac{V_{\text{out}}}{U_T}\right) \\ (C_1 + C_w) \frac{dV_x}{dt} &= -G_H V_{\text{out}} + C_1 \frac{dV_{\text{in}}}{dt}, \end{aligned} \quad (255)$$

where we have assumed subthreshold operation of the nonlinear conductance and all of the voltages are referenced to V_{ref} . As a single second-order equation, (255) can be written as

$$\begin{aligned} \frac{C_L C_T}{G_H G_L} \frac{d^2 V_{\text{out}}}{dt^2} &= -V_{\text{out}} - \frac{C_1}{G_H} \frac{dV_{\text{in}}}{dt} - \\ &\quad \frac{C_T}{G_H} \frac{dV_{\text{out}}}{dt} \left(1 + \frac{I_{\text{bN}}}{U_T G_L} \cosh\left(\frac{V_{\text{out}}}{U_T}\right) \right), \end{aligned} \quad (256)$$

where $C_T = C_1 + C_w$. The corresponding dimensionless form of (256) is

$$\ddot{y} = -H_1 L_1 y - L_1 \dot{y} (1 + c \cdot \cosh(y)) + L_1 \dot{u}, \quad (257)$$

where the variables x , y and u are related to the voltages V_x , V_{out} and V_{in} , respectively. H_1 and L_1 are proportional to G_H and G_L respectively, while c is equal to $I_{\text{bN}}/(U_T G_L)$. Note that c is the ratio of the small-signal transconductance gains of the G_N and G_L amplifiers.

To further simplify the analysis, we normalize (257) by setting its natural frequency, $\sqrt{H_1 L_1}$, to one. Then, we study the filter's response to a pure-tone input of unit frequency. Equation (257) is now

$$\ddot{y} + y = -L_1 (\dot{y} (1 + c \cdot \cosh(y)) + F \cos(\tau)), \quad (258)$$

where the input amplitude is F .

Notice that the nominal value of Q — that is, without the effect of the nonlinearity — is equal to $1/L_1$. To enhance the sensitivity and frequency selectivity bandpass filter, it normally has a Q of 5 to 10. Accordingly L_1 is a small, perturbation parameter and (258) is simply a resonator of unit frequency (LHS) that is perturbed by some nonlinear damping and a forcing function (RHS).

Using Lindstedt's method for perturbation analysis [20], the solution to (258) is

$$y = A \cos(\tau) + O(L_1), \quad (259)$$

where A , the amplitude of the fundamental frequency, is given by the following implicit function

$$A \left(1 + c \left(1 + \frac{A^2}{8} + \frac{A^4}{192} + \frac{A^6}{9216} \right) \right) - F = 0, \quad (260)$$

and $O(L_1)$ are higher harmonics. For values of $A < 2\sqrt{2/c}$, the filter's center-frequency gain is approximately $1/(1+c)$. However, as the output signal amplitude increases, the center-frequency gain reduces. The dimensionless quantity y is normalized as V/U_T . So, with a value of $U_T = 25\text{mV}$, $A = 2\sqrt{2/c}$ physically corresponds to an output voltage amplitude of $50\sqrt{2/c}$ mV. It is important to note that c is a ratio of transconductances. In VLSI circuits, physical ratios match much better than do absolute values, meaning that the compression characteristics of the filter ought to vary minimally across different chips. Figure 54 shows plots of (260) for various values of $c = I_{\text{bN}}/(U_T G_L)$. Higher values of c cause the knee to occur at lower values of output voltage.

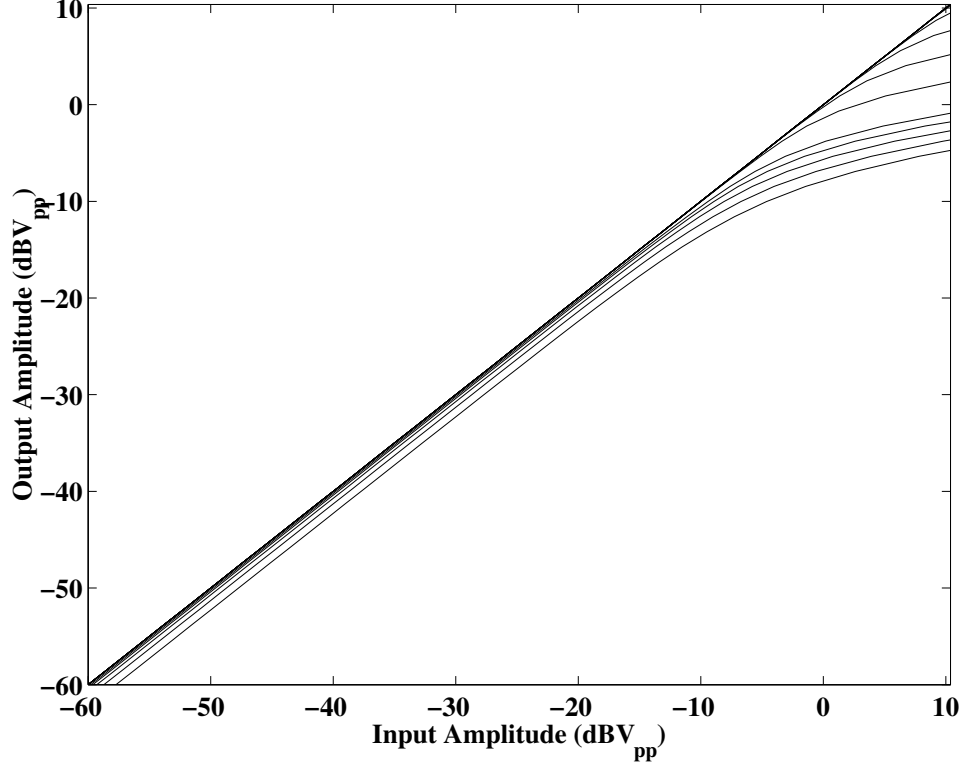


Figure 54. Theoretical knee control. Larger values of $c = I_{bN}/(U_T G_L)$ elicit lower knee values. The four curves with the most compression shown are for $c = 0.046, 0.086, 0.16$ and 0.3 .

7.4.2 Harmonic distortion

The sinh nonlinearity allows the filter's quality factor to adaptively reduce with increasing output amplitude, as desired. Unfortunately, the nonlinearity also introduces harmonic distortion, which is embodied in the $O(L_1)$ term of (259).

We arrive at an estimate of the distortion by solving (258) using higher order perturbation methods. The approximate total harmonic distortion (THD) is

$$\text{THD}(\%) = cL_1 \frac{A^2}{64} \left(1 + \frac{A^2}{16} + \frac{A^4}{640} \right) \cdot 100. \quad (261)$$

As (261) suggests, we can reduce the amount of distortion, independently of the amount of compression, by reducing the value of L_1 . Recall that the filter's nominal quality factor is $1/L_1$. So, reducing distortion by keeping L_1 small is not at odds with the desire to achieve high sensitivity and frequency selectivity. The fact that the distortion is reducible without affecting the amount of compression is crucial to

distinguishing this filter's adaptive behavior from the effects of unwanted, so-called instantaneous nonlinearity in other circuits.

7.4.3 Noise

The filter's distortion characteristics determine its largest permissible input. In this section, we analyze its noise performance, so as to define the smallest useful signal. We model noise in the filter by placing a noise source at the input of each of the otherwise noise-free amplifiers, as shown in Fig. 55. The total noise output power is

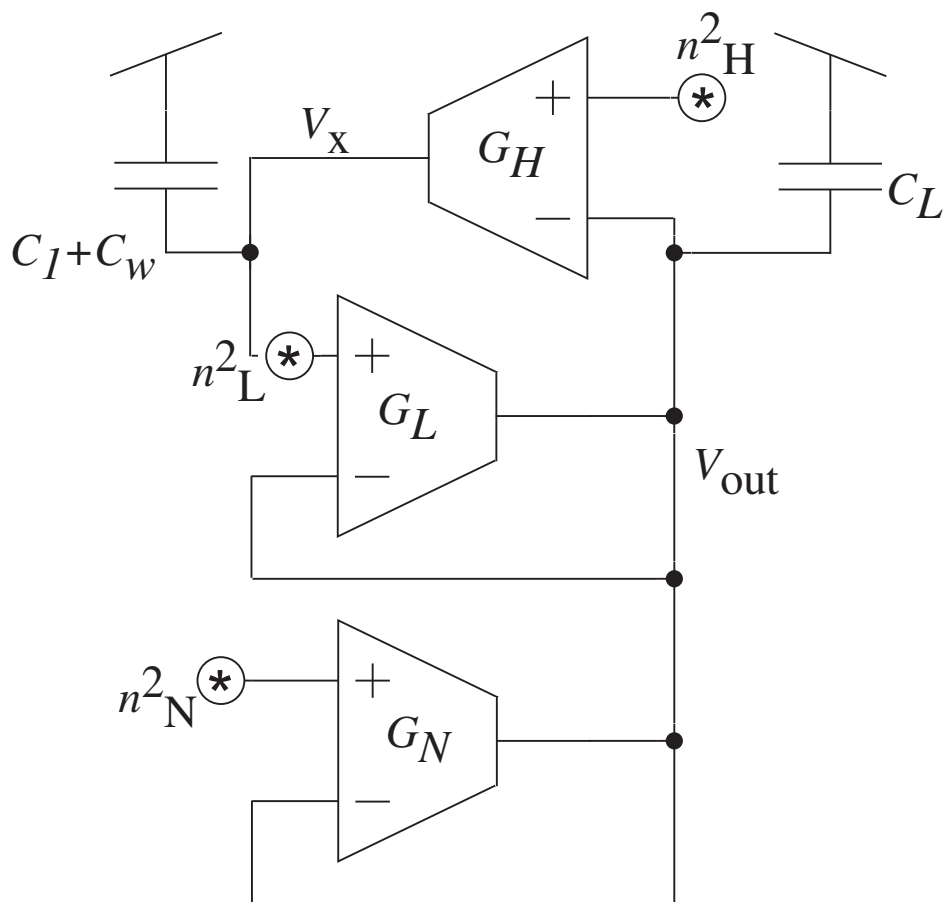


Figure 55. Schematic for analyzing noise in filter. The noise contribution of each amplifier is calculated and referred to its input.

given as

$$\begin{aligned}
\bar{n}_{\text{out}}^2 &= \int_0^\infty \frac{n_{\text{H}}^2}{\left(1 - \omega^2 \frac{C_{\text{L}}C_{\text{T}}}{G_{\text{H}}G_{\text{L}}}\right)^2 + \omega^2 \frac{C_{\text{T}}^2}{G_{\text{H}}^2}} d\omega \\
&+ \int_0^\infty \frac{n_{\text{L}}^2 \omega^2 \frac{C_{\text{T}}^2}{G_{\text{H}}^2}}{\left(1 - \omega^2 \frac{C_{\text{L}}C_{\text{T}}}{G_{\text{H}}G_{\text{L}}}\right)^2 + \omega^2 \frac{C_{\text{T}}^2}{G_{\text{H}}^2}} d\omega \\
&+ \int_0^\infty \frac{n_{\text{N}}^2 \omega^2 \frac{C_{\text{T}}^2 G_{\text{N}}^2}{G_{\text{H}}^2 G_{\text{L}}^2}}{\left(1 - \omega^2 \frac{C_{\text{L}}C_{\text{T}}}{G_{\text{H}}G_{\text{L}}}\right)^2 + \omega^2 \frac{C_{\text{T}}^2}{G_{\text{H}}^2}} d\omega,
\end{aligned} \tag{262}$$

where $n_{\text{H,L,N}}^2$ are noise power densities and G_{N} has been assumed to be a constant that is much less than G_{L} . If the circuit's flicker noise is negligible compared to thermal noise, then $n_{\text{H,L,N}}^2$ are independent of frequency. In this case the integrals of (262) can be evaluated to give

$$\bar{n}_{\text{out}}^2 = n_{\text{H}}^2 \frac{\pi G_{\text{H}}}{2C_{\text{T}}} + n_{\text{L}}^2 \frac{\pi G_{\text{L}}}{2C_{\text{L}}} + n_{\text{N}}^2 \frac{\pi G_{\text{N}}^2}{2C_{\text{L}}G_{\text{L}}}. \tag{263}$$

For a given bias current, subthreshold transistors yield the highest possible transconductance. For this reason, we will assume that the OTAs are operated in the subthreshold regime. The input-referred thermal noise density of a subthreshold OTA is

$$n^2 = \frac{2KqU_{\text{T}}^2}{\kappa^2 I_{\text{b}}\pi}, \tag{264}$$

where K is the effective number of noise-contributing transistors, q is the charge of one electron and I_{b} is the amplifier's bias current [60]. K is approximately equal to 8 in the implemented OTA [56]. For an OTA with an input capacitive attenuation factor $(M + 1)$, the bias current must be multiplied by $(M + 1)$ to maintain the transconductance gain and bandwidth. Further, the noise density referred to the input of the capacitive divider is the original OTA input-referred noise density multiplied

by $(M + 1)^2$. So, the input-referred noise densities of G_H and G_L are

$$\begin{aligned} n_H^2 &= (M_H + 1)^2 \frac{2KqU_T^2}{\kappa^2(M_H + 1)I_{bH}\pi} \\ &= (M_H + 1) \frac{2KqU_T^2}{\kappa^2 I_{bH}\pi} \end{aligned} \quad (265)$$

$$n_L^2 = (M_L + 1) \frac{2KqU_T^2}{\kappa^2 I_{bL}\pi}, \quad (266)$$

where $(M_{H,L} + 1)$ are the capacitive attenuation factors of amplifiers G_H and G_L . The noise density of G_N is

$$n_N^2 = \frac{qU_T^2}{\kappa^2 I_{bN}2\pi}. \quad (267)$$

We are assuming in this analysis that all of the body-effect coefficients are equal to κ . Using the fact that $G_H = \kappa I_{bH}/2U_T$, $G_L = \kappa I_{bL}/2U_T$ and $G_N = \kappa I_{bN}/U_T$, we substitute (265), (266) and (267) into (263) to get

$$\begin{aligned} \bar{n}_{\text{out}}^2 &= \frac{KqU_T}{4\kappa C_T} \left(M_H + 1 + \frac{C_T}{C_L} \left(M_L + 1 + \frac{2I_{bN}}{KI_{bL}} \right) \right) \\ &\approx \frac{KqU_T}{4\kappa C_T} \left(M_H + 1 + \frac{C_T}{C_L} (M_L + 1) \right). \end{aligned} \quad (268)$$

From (244), the total input-referred noise at the center frequency is

$$\bar{n}_{\text{in}}^2 \approx \frac{C_T}{C_1} \frac{KqU_T}{4C_1\kappa} \left(M_H + 1 + \frac{C_T}{C_L} (M_L + 1) \right). \quad (269)$$

We can minimize the noise, and hence maximize the dynamic range, by ensuring $C_L \gg C_1 \gg C_w$. Such a tactic comes at the expense of a larger circuit area and increased power consumption. Figure 56 illustrates the tradeoffs involved.

7.4.4 Stability

Simple eigenvalue analysis reveals that the circuit described by (257), is a small-signal stable system. However, as previous hearing-application front ends have shown, it may be possible for the filter's nonlinearity to cause large-signal instability [14]. This concern is particularly relevant in this filter's case, given that it explicitly introduces and exploits a nonlinear function.

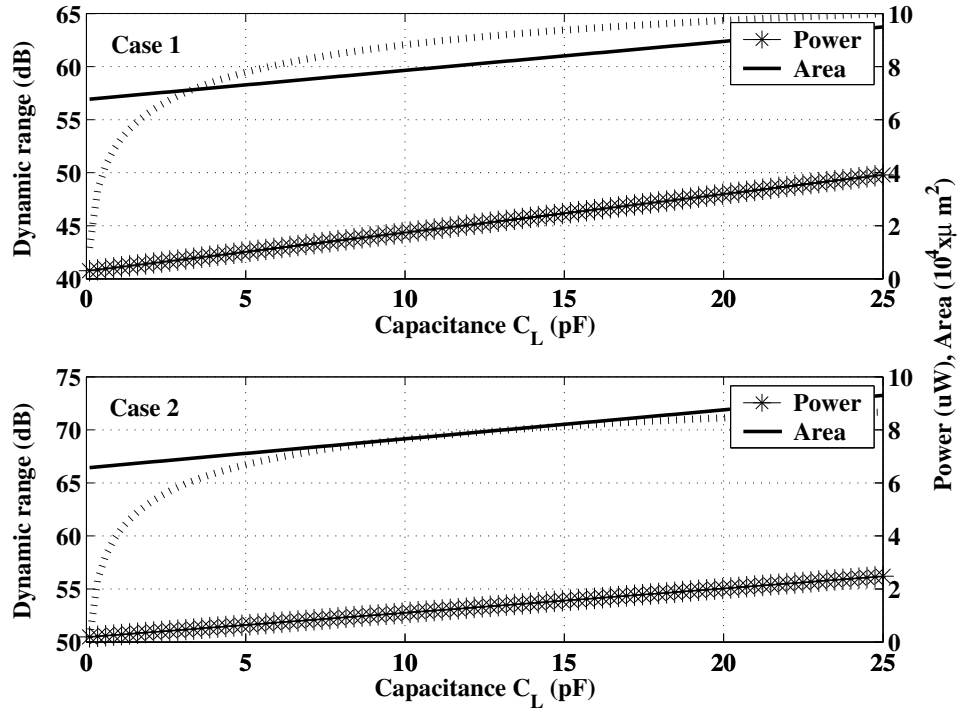


Figure 56. Tradeoff between dynamic range (dashed line, left horizontal axis), area (solid line, right axis) and power (asterisks, right axis) with C_L size. All three specifications — dynamic range, power and area — increase with increasing values of C_L , but the different design parameters of case 1 versus case 2 yield different performance specifications. Capacitor values for the upper panel (case 1) are $C_1 = 2\text{pF}$, $C_w = 2.9\text{pF}$, and $M_H = 10$, $M_L = 100$. In the lower panel (case 2), we set $C_1 = 3\text{pF}$, $C_w = 0.1\text{pF}$, keeping the other variables the same. Dynamic range is calculated using (269) and assuming a rail-to-rail linear range of 3.3V . Power consumption is calculated using (242) and (243) for $Q = 2$ at a center frequency of 1kHz .

A complete analysis of large-signal stability must regard all of the amplifiers in Fig. 51 as nonlinear; despite our best efforts as designers, G_H and G_L can never be perfectly linear. So, instead of the constant gains H_1 and L_1 , we represent the transconductances of G_H and G_L as H and L , respectively. H and L are nonlinear functions of their respective input voltages with the following properties. First of all, they are monotonically-increasing functions, which means that larger and larger inputs will elicit larger and larger outputs. Secondly, they pass through the origin, that is $H(0) = L(0) = 0$. In practice, H and L are sigmoidal functions as they are

formed from a differential pair. We write the filter's describing equations as

$$\begin{aligned}\frac{dy}{d\tau} &= L(x - y) - c \cdot L \sinh(y) \\ \frac{dx}{d\tau} &= -H(y) + \frac{du}{d\tau}.\end{aligned}\tag{270}$$

To prove large-signal stability in a dynamical system, it is sufficient to identify its equilibrium point, and to prove that the system always tends towards this point, regardless of initial conditions, and independent of any linearizing approximations. Setting all the time derivatives in (270) to zero, and from the property $H(0) = L(0) = 0$, we identify the origin as the system's unique equilibrium point³. Now, we define an energy-like function

$$V(y, e) = \int_0^y H(\chi) + \sinh(\chi) d\chi + \int_0^e L(\zeta) d\zeta,\tag{271}$$

where $e = x - y$.

From the monotonicity of H , L and \sinh , notice that the value of $V(y, e)$ is positive everywhere except at the origin, where it is equal to zero. Thus, the energy-like function is minimized at the origin. Further, the time derivative of $V(y, e)$ is negative everywhere but at the origin, where it is equal to zero. So, whenever it is not at the origin, the system possesses some positive amount of $V(y, e)$, which it dissipates over time. When $V(y, e) = 0$, the dissipation ceases, at which point the state variables are now at the origin. This argument shows, as would a more formal application of Lyapunov's Theorem [61], that the circuit is large-signal stable.

7.5 Circuit implementation and experimental results

We fabricated a prototype of the adaptive-Q bandpass filter in a $0.5\mu\text{m}$ process available from MOSIS, a die photo of which is shown in Fig. 57. The pMOS transistors of

³The property that $H(0) = L(0) = 0$ is simply for the convenience of defining the equilibrium point at the origin. The point $(x, y) = (0, 0)$ in state space corresponds to the physical voltages V_x and V_{out} being equal to V_{ref} , plus some offset. That is, the operating point of V_x is V_{ref} plus the offset of the G_H OTA, while the operating point of V_{out} is V_{ref} plus the sum of the offsets of G_H and G_L .

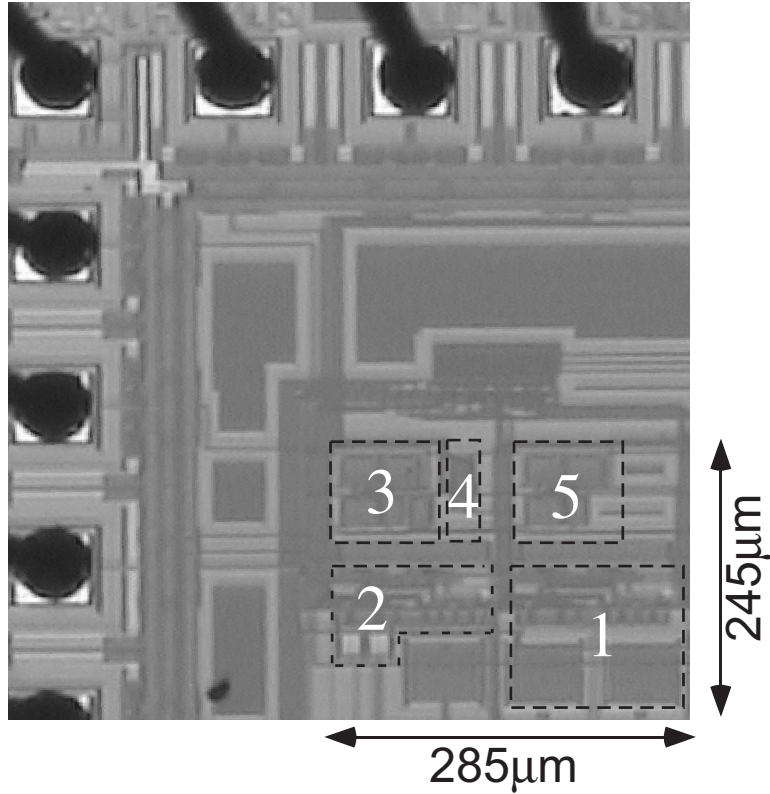


Figure 57. Die photograph of the bandpass filter. The portions labelled 1–5 are, respectively, the G_L amplifier, the G_H amplifier, the output buffer for the V_{out} node, the sinh transconductor, and the output buffer for the V_x node. The integrating capacitors C_w , C_L and C_1 are not labelled, but they are included in the $285 \times 245 \mu\text{m}^2$ area shown here.

amplifiers G_H and G_L were sized $30 \mu\text{m}/3 \mu\text{m}$ to allow for large subthreshold currents. The nMOS transistors in both amplifiers were sized at $15 \mu\text{m}/3 \mu\text{m}$. The nMOS and pMOS transistors of the G_N amplifier were sized at $3 \mu\text{m}/1.5 \mu\text{m}$ and $6 \mu\text{m}/1.5 \mu\text{m}$, respectively. The G_N transistors were sized relatively small to facilitate the tuning of small values of I_{bN} , which would correspond to small values of c (for testing purposes, V_n and V_p of Fig. 53(a) were not set by bias circuitry, but by an off-chip DAC). The drawn capacitor values were $C_1 = C_L = 2 \text{pF}$, $C_w = 2.9 \text{pF}$ ⁴. Since V_{out} is an attenuated version of the input and experiences compression at that, we chose $(M_H + 1) = 11$ for the capacitive divider ratio of G_H . The positive input of G_N is V_x , which has voltage

⁴Analysis shows that these are not the optimal values for a low-noise filter. For this prototype circuit, I was more concerned with demonstrating low-power, low-distortion gain adaptation than in optimizing for noise performance.

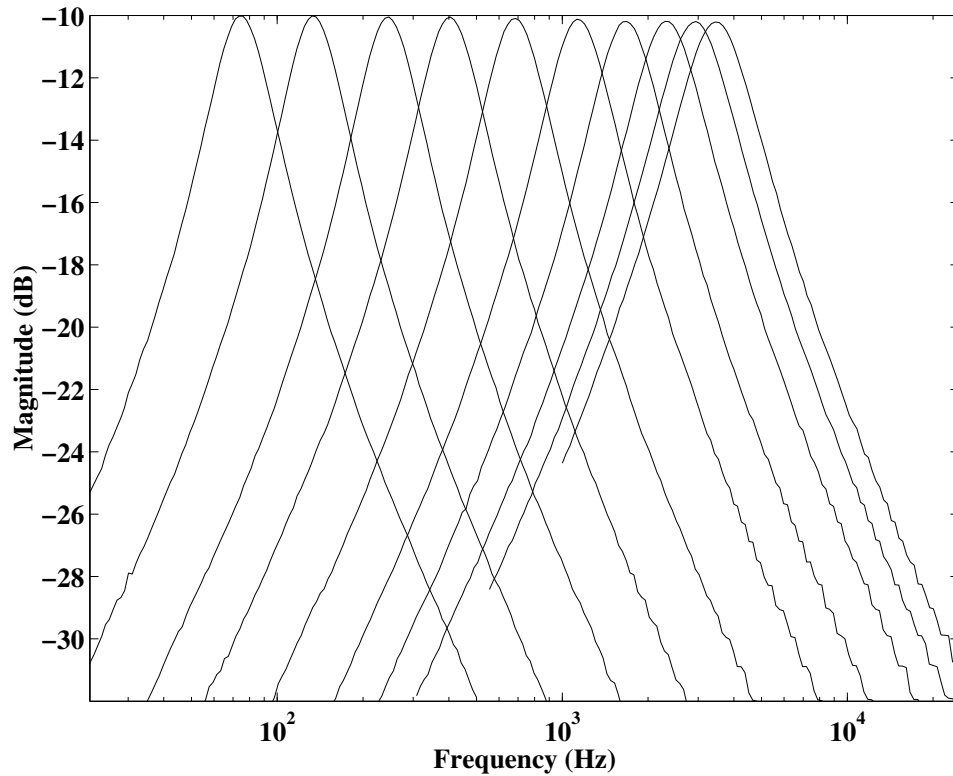


Figure 58. Center frequency control. The bandpass filter center frequency is directly proportional to the geometric mean of the gains G_L and G_H , and is tunable independent of the automatic gain control action.

excursions that can approach the power rails. The capacitive divider ratio for G_L was therefore chosen to be $(M_L + 1) = 101$. My design choices placed the prototype filter in the Case 1 of Fig. 56. With $C_L = 2\text{pF}$, the circuit area is 0.07mm^2 . The predicted dynamic range and power consumption are 55.8dB and $0.6\mu\text{W}$ (for $Q = 2$ at a 1kHz center frequency), respectively.

As the results of Fig. 58 show, the circuit behaves as a second-order bandpass filter as expected, and has a tunable center frequency across the audio range. When programmed to a center frequency of 1.18kHz and a Q of 2, the bandpass filter consumes $1.32\mu\text{W}$ of power, which is twice the amount predicted in Fig. 56. Power consumption is directly proportional to the filter's center frequency. For instance, if the filter were programmed to a center frequency of 11.8kHz , it would consume $13.2\mu\text{W}$.

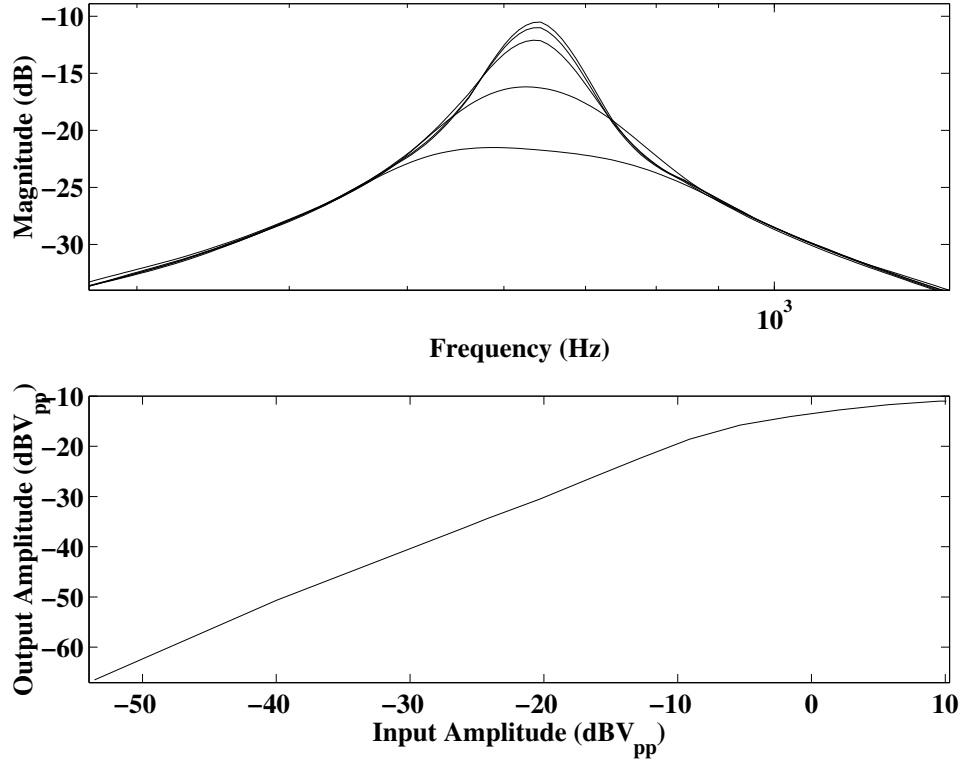


Figure 59. Quality factor adaptation. The upper panel depicts a reduction in Q from 8 to 2 with increasing input amplitudes. The transfer curves shown are for the following input amplitudes: $-5.2\text{dBV}_{\text{pp}}$, $-4.4\text{dBV}_{\text{pp}}$, $-2.3\text{dBV}_{\text{pp}}$, 4dBV_{pp} , $10.3\text{dBV}_{\text{pp}}$. The bottom panel shows the same information as a plot of output amplitude versus input amplitude at the filter's center frequency. The filter was programmed to a center frequency of 1.18kHz and $Q = 10$.

Experimental measurements confirm that the filter exhibits the adaptive behavior that we designed for. Figure 59 shows how the magnitude-frequency response of the filter changes with different input amplitudes. For input amplitudes less than 5.6mV_{pp} , the center-frequency gain is almost -10dB . The gain reduces progressively for larger input amplitudes and drops by over 10dB when the input amplitude exceeds $2V_{\text{pp}}$.

Figure 60 demonstrates experimental control of the threshold knee point. The various curves correspond to different values of I_{bN} , with fixed G_{L} . We set I_{bN} with the voltages V_{p} and V_{n} . For $V_{\text{p}} = 3.3\text{V}$ and $V_{\text{n}} = 0\text{V}$, I_{bN} is essentially zero, meaning that compression is turned off. For non-zero values of I_{bN} , compression is observed at different output amplitude knee points. It was difficult to achieve fine resolutions

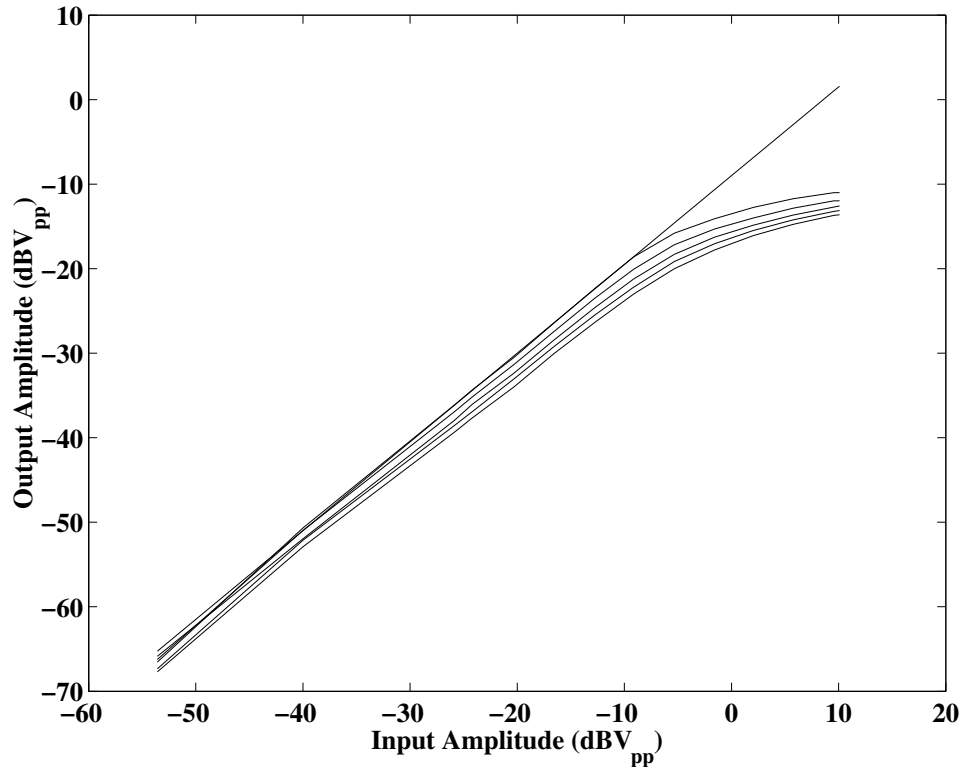


Figure 60. Threshold knee point control. The normalized input-output amplitude response, measured at the center frequency, shows that the gain exhibits compressive behavior past a certain output amplitude threshold. This threshold point can be adjusted by varying the transconductance gain of the sinh amplifier (effectively by varying its bias current).

for small values of I_{bN} , which is why the curves shown in Fig. 60 all have knee-points for output amplitudes close to -20dB .

Explicit use of nonlinearity raises the question of how much distortion the circuit will suffer. Figure 61 supports the claim that the amount of distortion is minimal. The sinh nonlinearity contributes most of the third harmonic, since the other two OTAs have been linearized via capacitive attenuation. However, there is a significant second harmonic in the left panel of Fig. 61, due to input offset in the G_H and G_L amplifiers. By adjusting the amount of charge stored on their differential-pair input gates, we were able to reduce the offset significantly. This improvement is shown in the right panel of Fig. 61, where the second harmonic has fallen from a maximum of 8% to less than 2%. At the maximum input amplitude, the THD for the improved case

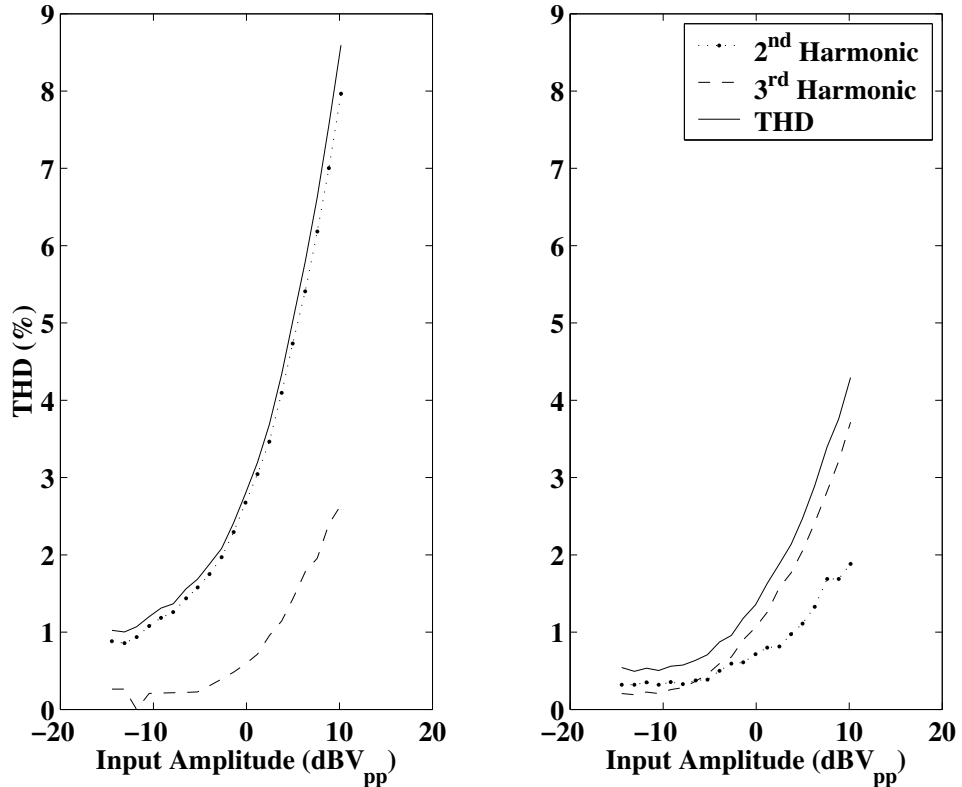


Figure 61. THD reduction with offset removal. The left panel shows the distortion numbers for when an equal amount of charge is placed (via injection and tunnelling) on the floating gates of each differential-pair in the filter. Transistor mismatch causes offset, which is observed as a large second harmonic. When the offset is compensated for with an uneven amount of charge, the second harmonic reduces, as shown in the right-hand panel. Offset removal should ordinarily not affect odd-order harmonics, and the slight increase in third harmonic content is due to measurement error.

is 4.3%. This THD figure falls within the acceptable range for cochlear implants [59]. Some subjective tests of hearing aids have suggested that wearers do not find THDs of 3 to 6% disagreeable [62].

The measured output noise power spectrum is shown in Fig. 62. The total integrated input-referred noise is $2.2\text{mV}_{\text{rms}}$, which gives an input dynamic range of 54.5dB, a close match to the theoretical value of Fig. 56.

Designers quantify the adaptation speed of conventional AGCs with the attack and release times [41]. Since the bandpass filter incorporates the AGC action, the time constant of the input signal is always well-defined. (It is roughly the reciprocal of the filter’s center frequency.) It therefore makes sense to employ adaptation speeds

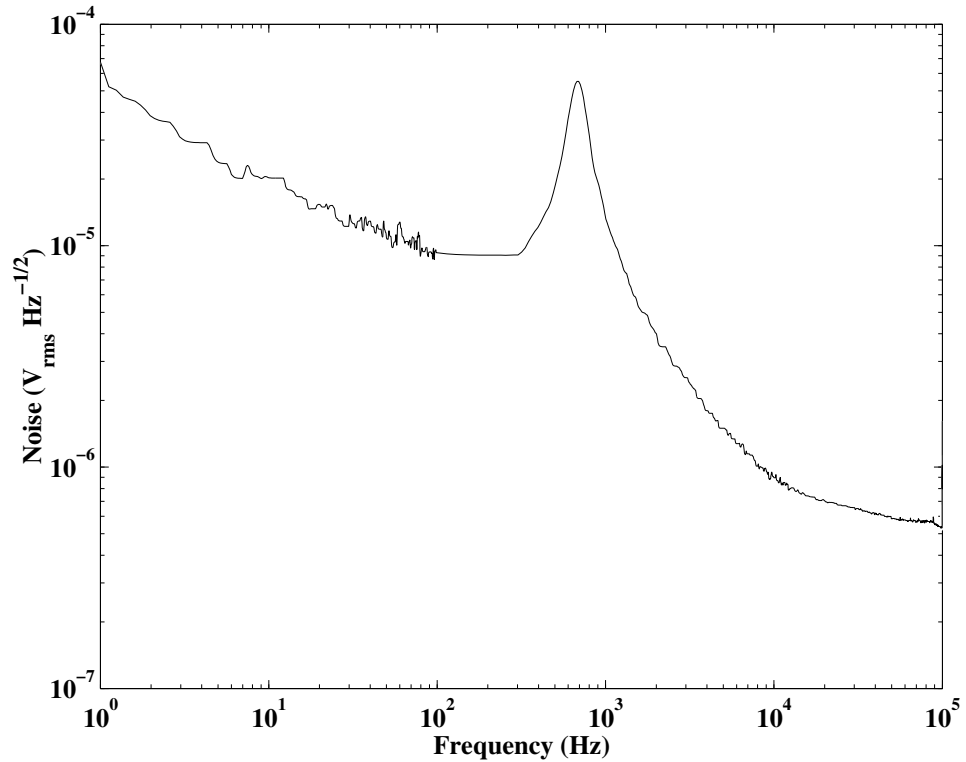


Figure 62. Measured noise power spectrum. The output noise has a bandpass profile (from G_L and G_N) summed with a lowpass profile (from G_H). The flicker noise corner frequency is 100Hz, which is just low enough for thermal noise to dominate.

that are on the same order of the expected input-signal time constant, as shown in Fig. 63. Also, noise-pumping is not a concern for the following reasons. First, the filter’s gain adapts smoothly with input amplitude. Secondly, the adaptation is largely restricted to a narrow band around the center frequency, which ensures that the gain applied to noise of a given level is always constant, and not influenced by other noise signals that are outside the bandwidth of interest.

7.6 Discussion of results

The experimental results of the prototype circuit conform to the theoretical claims. However, a practical hearing aid would require more particular specifications.

Consider designing a hearing aid for patients with mild to severe hearing loss. While this application requires compression of up to 40dB, the prototype circuit only

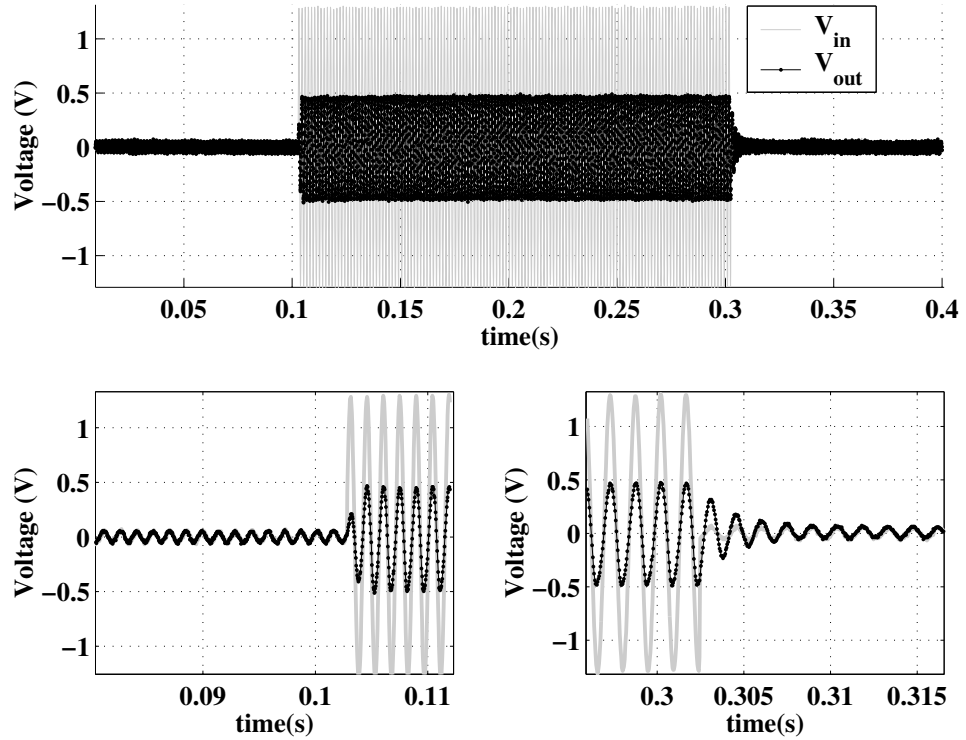


Figure 63. Filter response to input bursts. As the zoomed-in figures show, the attack and release time of the gain control scheme correspond to about one period of the input signal.

exhibits a maximum of 15dB. One solution is to cascade two filters per channel, in order to create a fourth-order bandpass filter, which would provide 30dB of compression. The cost of this approach is a doubling in area and power consumption. Also, the dynamic range of the filter is reduced by A_{w0} . We can get the remaining 10dB of compression from a wide-band automatic gain control. The hearing aid still offers multichannel compression, provided the patient experiences at least a 10dB hearing loss across all frequency bands.

Microphones deliver up to 80dB of output signal range [63]. So, even assuming that the signal is compressed by 10dB, the bandpass filter still has to support a 70dB dynamic range of input. The prototype circuit does not meet this specification but Fig. 56 suggests a design that would. If we chose $C_1 = 3\text{pF}$, $C_w = 0.1\text{pF}$ and $C_L = 10\text{pF}$, then, at the expense of power and area, the filter would achieve a 70dB dynamic range. Table 1 summarizes the novel filter's performance, in comparison to

Table 1. Comparison of filter performance to other work

	This work	[59]	[64]	[65]
Dynamic range (dB)	55	62	57	62
THD (%)	4.3	5	2	1.1
Power (μ W)	1.12	2	6	16
Compression (dB)	15	0	0	0

other filters that were designed for hearing instruments. The columns labeled The power consumption is normalized to that of a filter with a 1kHz center frequency.

CHAPTER 8

CONCLUSION

Analog circuit designers are concerned with much more than just the linear amplification of signals. Rectifiers, oscillators, phase-locked loops, modulators and automatic-gain control circuits are a few of the common analog components whose functions are unquestionably nonlinear. However, there is a surprisingly enduring notion that a linear-based design is appropriate for these and other analog circuits. For instance, unlike what is presented in this dissertation, sinusoidal oscillator design is often framed in terms of fulfilling Barkhausen's criteria [35]. This is not a very useful concept, as it demands a practical impossibility; that is, to design a linear system with purely imaginary poles. Whenever linear-systems thinking fails, the common reaction is to eschew design formalisms in favor of a heavily-experiential design approach. Unfortunately, the performance requirements of applications like autonomous systems, portable electronics, and implantable biomedical devices render such an ad hoc design approach very costly.

Not only are many classical analog circuits decidedly nonlinear, but the transistor, which is the elemental component of integrated circuits, is itself a highly nonlinear device. This fact can be used to great effect in scenarios such as biomedical and human-interface applications, where processing must be performed efficiently. The key to achieving efficient analog computation is to look beyond the customary linearized view of circuits in favor of a more genuine representation that allows rich, nonlinear processing to be efficiently and naturally implemented.

8.1 Main contributions

The overarching theme of this dissertation has been to present analog circuit analysis and design from a nonlinear dynamics perspective. Following is a list of the specific

contributions that have been made to this end.

8.1.1 Nonlinear dynamics in integrated circuits

An introduction to fundamental concepts of nonlinear dynamical systems theory, suitable for an integrated circuits audience, has been given.

The procedure of nondimensionalization was used to derive the state-space representation of circuits. In Chapter 2, the vector field was used to analyze nonlinear phenomena in one-dimensional circuits. The implications of different types of nonlinearities on a circuit's convergence to equilibrium were explored. The notion of bifurcation was introduced in the context of symmetric odd-order nonlinearities. For the OTA circuit, whose tanh function is a compressive nonlinearity, a supercritical pitchfork bifurcation is possible. For the output buffer, whose sinh function is an expansive nonlinearity, a subcritical pitchfork bifurcation is possible.

Bifurcation was revisited in Chapter 3, with emphasis given to Hopf bifurcations and their classification, using the Poincaré-Bendixon Theorem. In circuit design, bifurcation often occurs when a high-Q system loses stability. In such a scenario, there is most likely a pair of complex eigenvalues that are crossing the imaginary axis, which implies a Hopf bifurcation. The circuit that was used to illustrate the concepts in Chapter 3 is the SOS described in [14].

Regular perturbation was used in Chapter 4 to predict the amount of harmonic distortion that a circuit suffers due its nonlinear terms. The nonlinear dynamic bases of several well-known tenets of low-distortion circuit design were provided. For instance, the idea that operating well below a system's corner frequency reduces distortion is explained by the fact that the magnitudes of the first few harmonics peak around the corner frequency. In terms of choice of transistor operating region, above-threshold is preferable to subthreshold, because, even though a circuit's distortion terms are functionally identical in both cases, it turns out that, in the subthreshold case, the terms are systematically larger, which results in more distortion. Finally,

the regular perturbation analyses revealed why it is beneficial for a circuit to contain some form of negative feedback. The source follower and the unity-gain amplifier were used as illustrative examples in this chapter.

8.1.2 Design of OTA-C sinusoidal oscillators with OTA nonlinearity

A methodology for designing low-distortion sinusoidal oscillators that is based on OTA nonlinearity was presented in Chapter 6. The use of a “negative resistor”, whose transfer function was shown in Fig. 26, for building sinusoidal oscillators is well-documented in the literature. Nevertheless, various attempts have been made — some less successful than others — to exploit the natural saturating characteristics of an OTA in an oscillator. In Chapter 6, the notion of making use of the OTA’s sigmoidal nonlinearity was reconciled with that of the classical negative resistor. The primary insight is that the OTA nonlinearity should not be used directly for amplitude limiting, but that its saturating characteristic should rather be used in conjunction with a linearized OTA to implement the negative resistor, as shown in Fig. 27.

To provide the most amount of usability, a sinusoidal oscillator’s amplitude and frequency of oscillation must be controlled by some physical parameter in a predictable way. Also, harmonic distortion must be kept to a minimum. The characteristics of the oscillators that are derived from the design methodology of Chapter 6 were analyzed via perturbation methods. Using the results of the perturbation analysis, in conjunction with phase plane analysis, the design methodology was developed to yield oscillators whose harmonic distortion is kept to a minimum and is unaffected by changing the amplitude or the frequency of oscillation. An oscillator that meets such specifications is suitable for use in communication and instrumentation applications.

8.1.3 Design of a bandpass filter for auditory signal processing

In Chapter 7, the theory and design of a novel, nonlinear bandpass filter for use in auditory prostheses was developed, along with its circuit implementation. Like

other auditory processing front ends, including the human cochlea, the filter described is meant to provide frequency analysis and nonlinear gain compression of input signals. In Chapter 7, this processing functionality was framed in terms of step responses, as opposed to the more usual (for the auditory processing community, at least) magnitude-frequency responses. Performing step response analysis, coupled with phase plane analysis, the theoretical characteristics of the dynamical system that would yield the desired behavior were identified.

Perturbation methods were used to ascertain that the geometrically-derived dynamical system would exhibit the gain compression and bandpass filtering functions as desired. The amount of distortion suffered by the system was also calculated using perturbation methods. Bifurcation analysis revealed that certain circuit implementations might result in an unstable filter. The circuit implementation that was finally chosen is simple and area- and power efficient. In addition, a Lyapunov stability test proves that this circuit implementation can have only one globally-stable equilibrium.

Despite its being nonlinear, the filter presented in Chapter 7 is designed to avoid unwanted distortion. It is one of the most efficient implementations (in terms of area and power consumption) ever reported of the cochlea's compressive mechanism, and it is a practical component of an advanced auditory processor.

8.1.4 Studying integrated circuit dynamics on a reconfigurable platform

The efficacy of using a reconfigurable analog integrated circuit chip as a platform for studying nonlinear dynamics phenomena was demonstrated. The reconfigurable analog chip is invaluable as an educational tool both for circuit designers who want to understand nonlinear dynamics and for applied mathematicians who want a pliable physical manifestation of nonlinear dynamical equations.

REFERENCES

- [1] I. Akyildiz, W. Su, Y. Sankarasubramaniam, and E. Cayirci, “A survey on sensor networks,” *IEEE Communications Magazine*, vol. 40, no. 8, pp. 102–114, 2002.
- [2] J. Hart and K. Martinez, “Environmental sensor networks: a revolution in the earth system science?” *Earth-Science Reviews*, vol. 78, pp. 177–191, 2006.
- [3] K. V. Laerhoven, B. P. L. Lo, J. W. P. Ng, S. Thiemjarus, R. King, S. Kwan, H.-W. Gellersen, M. Sloman, O. Wells, P. Needham, N. Peters, A. Darzi, C. Toumazou, and G.-Z. Yang, “Medical healthcare monitoring with wearable and implantable sensors,” in *Proc. 3rd Int’l Workshop on Ubiquitous Computing for Pervasive Healthcare Applications, UbiHealth ’04*, Nottingham UK, Sept 2004.
- [4] M. J. M. Pelgrom, A. Duinmaijer, and A. Welbers, “Matching properties of mos transistors,” *IEEE J. Solid-State Circuits*, vol. 24, no. 5, pp. 1433–1439, 1989.
- [5] S. Kirolos, J. Laska, M. Wakin, M. Duarte, D. Baron, T. Ragheb, Y. Massoud, and R. Baraniuk, “Analog-to-information conversion via random demodulation,” in *Proc. IEEE Dallas/CAS Workshop on Design, Applications, Integration and Software*, Richardson TX, Oct 2006, pp. 71–74.
- [6] J. Cruz and L. Chua, “A cmos ic nonlinear resistor for chua’s circuit,” *TCASI: Fundamental Theory and Applications*, vol. 39, no. 12, pp. 985 – 995, 1992.
- [7] D. L. Grundy, “A computational approach to vlsi analog design,” *Analog Integrated Circuits and Signal Processing*, vol. 8, no. 1, pp. 53 – 60, 1994.
- [8] B. A. Minch, “Translinear analog signal processing: a modular approach to large-scale analog computation with multiple-input translinear elements,” in *Proc. ARVLSI, 20th Anniversary*, Atlanta, GA, March 1999, pp. 186–199.
- [9] C. M. Twigg and P. E. Hasler, “A large-scale reconfigurable analog signal processor (rasp) ic,” in *Proc. IEEE Custom Integrated Circuits Conference, CICC’06*, Sep 2006, pp. 5–8.
- [10] K. Odame, C. Twigg, A. Basu, and P. Hasler, “Studying nonlinear dynamical systems on a reconfigurable analog platform,” in *ISCAS ’07*, May 2007, pp. 445 – 448.
- [11] C. C. Enz, F. Krummenacher, and E. A. Vittoz, “An analytical mos transistor model in all regions of operation and dedicated to low-voltage and low-current applications,” *Analog Integrated Circuits and Signal Processing*, vol. 8, no. 1, pp. 83–114, 1995.

- [12] B. Lathi, *Modern Digital and Analog Communication Systems*. New York, NY: Oxford University Press, 1998.
- [13] J. Mulder, A. V. der Woerd, W. Serdijn, and A. V. Roermund, “An rms-dc converter based on the dynamic translinear principle,” *IEEE J. Solid-State Circuits*, vol. 32, no. 7, pp. 1146–1150, 1997.
- [14] R. Lyon and C. Mead, “An analog electronic cochlea,” *IEEE Trans. on Acoustics, Speech and Signal Proc.*, vol. 36, no. 7, pp. 1119–1134, 1988.
- [15] P. Allen and D. Holberg, *CMOS Analog Circuit Design*. New York, NY: Oxford University Press, 2002.
- [16] J. Guckenheimer and P. Holmes, *Nonlinear Oscillations, Dynamical Systems, and Bifurcations of Vector Fields*. New York, NY: Springer-Verlag, 1983.
- [17] S. H. Strogatz, *Nonlinear Dynamics and Chaos*. Cambridge, MA: Westview, 1994.
- [18] K. Odame and P. Hasler, “Exploiting ota nonlinearity in the design of a second order section oscillator,” in *Proc. RISP International Workshop on Nonlinear Circuits and Signal Processing, 2006*, Mar 2006, pp. 5–8.
- [19] A. Buonomo and A. L. Schiavo, “Perturbation analysis of nonlinear distortion in analog integrated circuits,” *TCASI: Fundamental Theory and Applications*, vol. 52, no. 8, pp. 1620–1631, 2005.
- [20] R. Rand, *Lecture Notes on Nonlinear Vibrations*. Ithaca, NY: The Internet-First University Press, 2003.
- [21] K. Odame and P. Hasler, “Harmonic distortion analysis via perturbation methods,” in *Proc. 51st Midwest Symposium on Circuits and Systems*, Knoxville, TN, August 2008.
- [22] A. Buonomo, C. D. Bello, and O. Greco, “A criterion of existence and uniqueness of the stable limit cycle in second-order oscillators,” *IEEE Trans. Circuits Syst.*, vol. CAS-30, no. 9, pp. 680–683, 1983.
- [23] A. Buonomo, C. D. Bello, and A. L. Shiavo, “On the analysis and design of second-order harmonic oscillators,” in *Proc. ISCAS’00*, vol. 1, May 2000, pp. 623–626.
- [24] A. Rodriguez-Vazquez, B. Linares-Barranco, J. Huertas, and E. Sanchez-Sinencio, “On the design of voltage-controlled sinusoidal oscillators using ota’s,” *IEEE Trans. Circuits Syst.*, vol. 37, no. 2, pp. 198–211, 1990.
- [25] B. Linares-Barranco, T. Serrano-Gotarredona, J. Ramos-Martos, J. Ceballos-Cceres, J. M. Mora, and A. Linares-Barranco, “A precise 90° quadrature ota-oscillator tunable in the 50-130 mhz range,” *TCASI: Fundamental Theory and Applications*, vol. 51, no. 4, pp. 649–663, 2004.

- [26] K. Odame and P. Hasler, “Theory and design of ota-c oscillators with native amplitude limiting,” *Accepted to TCASI: Fundamental Theory and Applications*, 2008.
- [27] J. A. D. Lima and P. R. Agostinho, “A low-voltage low sensitivity sinusoidal vco for dpll realizations,” in *Proc. ISCAS’04*, May 2004, pp. 789–792.
- [28] J. Galan, R. Carvajal, A. Torralba, F. Munoz, and J. Ramirez-Angulo, “A low-power low-voltage ota-c sinusoidal oscillator with a large tuning range,” *TCASI: Fundamental Theory and Applications*, vol. 52, no. 2, pp. 283–291, 2005.
- [29] T. Serrano-Gotarredona and B. Linares-Barranco, “7-decade tuning range cmos ota-c sinusoidal vco,” *Electronics Letters*, vol. 34, no. 17, pp. 1621–1622, 1998.
- [30] L. Perko, *Differential Equations and Dynamical Systems*. New York, NY: Springer, 2001.
- [31] B. V. der Pol, “On relaxation oscillations,” *Philos. Mag.*, vol. 27, pp. 978–992, 1926.
- [32] B. Linares-Barranco, A. Rodriguez-Vazquez, E. Sanchez-Sinencio, and J. Huer-tas, “On the generation design and tuning of ota-c high frequency sinusoidal oscillators,” *IEE Proceedings-Part G, Circuits Devices and Systems*, vol. 139, no. 5, pp. 557–568, 1992.
- [33] S. Koziel, R. Schaumann, and H. Xiao, “Analysis and optimization of noise in continuous-time ota-c filters,” *TCASI: Fundamental Theory and Applications*, vol. 52, no. 6, pp. 1086–1094, 2005.
- [34] S. DeWeerth, G. Patel, and M. Simoni, “Variable linear-range subthreshold ota,” *Electronics Letters*, vol. 33, no. 15, pp. 1309–1311, 1997.
- [35] B. Razavi, *RF Microelectronics*. Upper Saddle River, NJ: Prentice Hall, 1998.
- [36] B. Limketkai and R. Brodersen, “An equation-based method for phase noise analysis,” in *Proc. CICC’03*, Sept 2003, pp. 703–706.
- [37] R. Sarpeshkar, R. F. Lyon, and C. Mead, “A low-power wide-linear-range transconductance amplifier,” *Analog Integrated Circuits and Signal Processing*, vol. 13, pp. 123–151, 1997.
- [38] S. T. Neely and D. O. Kim, “A model for active elements in cochlear biomechan-ics,” *J. Acoust. Soc. Am.*, vol. 79, pp. 1472–1480, 1986.
- [39] D. S. Lum and L. D. Braida, “DSP implementation of a real-time hearing loss simulator based on dynamic expansion,” in *Modeling Sensorineural Hearing Loss*, W. Jesteadt, Ed. Mahwah, New Jersey: Lawrence Erlbaum Associates, 1997, ch. 7, pp. 113–130.

- [40] J. B. Allen, "Derecruitment by multiband compression in hearing aids," in *Modeling Sensorineural Hearing Loss*, W. Jesteadt, Ed. Mahwah, New Jersey: Lawrence Erlbaum Associates, 1997, ch. 6, pp. 99–112.
- [41] T. Fortune, "Amplifiers and circuit algorithms of contemporary hearing aids," in *Hearing aids: standards, options, and limitations*, M. Valente, Ed. New York, New York: Thieme Medical Publishers, 1996, ch. 4, pp. 157–209.
- [42] A. Engebretson, "Benefits of digital hearing aids," *IEEE Engineering in Medicine and Biology Magazine*, vol. 13, no. 2, pp. 238–248, 1994.
- [43] B. Edwards, "Signal processing techniques for a dsp hearing aid," in *Proc. IS-CAS'98*, vol. 6, Monterey, CA, May 1998, pp. 586–589.
- [44] K. Odame, D. Anderson, and P. Hasler, "A bandpass filter with inherent gain adaptation for hearing applications," *TCASI: Fundamental Theory and Applications*, vol. 55, no. 3, pp. 786–795, 2008.
- [45] D. M. Chabries, D. V. Anderson, T. G. Stockham, Jr., and R. W. Christiansen, "Application of a human auditory model to loudness perception and hearing compensation," in *Proc. ICASSP'95*, vol. 5, May 1995, pp. 3527–3530.
- [46] E. Fragniere, A. van Schaik, and E. Vittoz, "Design of an analogue vlsi model of an active cochlea," *Analog Integrated Circuits and Signal Processing*, vol. 13, no. 1, pp. 19–35, 1997.
- [47] B. Wilson, D. Lawson, J. Müller, R. Tyler, and J. Kiefer, "Cochlear implants: Some likely next steps," *Annu. Rev. Biomed. Eng.*, vol. 5, pp. 207–249, 2003.
- [48] W. Serdijn, A. van der Woerd, J. Davidse, and A. van Roermund, "A low-voltage low-power fully-integratable automatic gain control for hearing instruments," *IEEE J. Solid-State Circuits*, vol. 29, no. 8, pp. 943–946, 1994.
- [49] A. C. Neuman, M. H. Bakke, C. Mackersie, S. Hellman, and H. Levitt, "The effect of compression ratio and release time on the categorical rating of sound quality," *J. Acoust. Soc. Am.*, vol. 103, no. 5, Pt 1, pp. 2273–2281, May 1998.
- [50] D. V. Anderson, "Model based development of a hearing aid," Master's thesis, Brigham Young University, Provo, Utah, 1994.
- [51] D. V. Anderson, R. W. Harris, and D. M. Chabries, "Evaluation of a hearing compensation algorithm," in *Proc. ICASSP'95*, vol. 5, May 1995, pp. 3531–3533.
- [52] E. W. Yund and K. M. Buckles, "Multichannel compression hearing aids: Effect of number of channels on speech discrimination in noise," *J. Acoust. Soc. Am.*, vol. 97, no. 2, pp. 1206–23, Feb. 1995.
- [53] J. Zwislocki, Y. Szymko, and L. Hertig, "The cochlea is an automatic gain control system after all," in *Diversity in Auditory Mechanics*. World Scientific, Singapore, 1996.

- [54] B. Johnstone, R. Patuzzi, and G. Y. G.K., “Basilar membrane measurements and the travelling wave,” *Hearing Research*, vol. 22, pp. 147–153, 1986.
- [55] P. Dallos, “The active cochlea,” *J. Neuroscience*, vol. 12, no. 12, pp. 4575–4585, 1992.
- [56] R. Harrison and C. Charles, “A low-power low-noise cmos amplifier for neural recording applications,” *IEEE J. Solid-State Circuits*, vol. 38, no. 6, pp. 958–965, 2003.
- [57] B. Razavi, *Design of Analog CMOS Integrated Circuits*. New York, NY: McGrawHill, 2001.
- [58] P. Hasler, B. A. Minch, and C. Diorio, “Adaptive circuits using pfet floating-gate devices,” in *Proc. Advanced Research in VLSI’99*, Atlanta, GA, March 1999, pp. 215–229.
- [59] C. Salthouse and R. Sarpeshkar, “A practical micropower programmable band-pass filter for use in bionic ears,” *IEEE J. Solid-State Circuits*, vol. 38, no. 1, pp. 63–70, 2003.
- [60] R. Sarpeshkar, R. Lyon, and C. Mead, “A low-power wide-linear-range transconductance amplifier,” *Analog Integrated Circuits and Signal Processing*, vol. 13, no. 1–2, pp. 123–151, 1997.
- [61] H. Khalil, *Nonlinear Systems*. Upper Saddle River, NJ: Prentice-Hall, 2002.
- [62] J. Agnew, “Hearing instrument distortion: What does it mean for the listener?” *Hear Instrum.*, vol. 39, no. 10, pp. 11–16, 1988.
- [63] J. N. Jr. and K. Gabriel, “A fully-integrated cmos-mems audio microphone,” in *Proc. Int. Conf. Transducers, Solid-State Sensors, Actuators and Microsystems*, June 2003.
- [64] W. Serdijn, M. Broest, J. Mulder, A. V. D. Woerd, and A. V. Roermund, “A low-voltage ultra-low-power translinear integrator for audio filter applications,” *IEEE J. Solid-State Circuits*, vol. 32, no. 4, pp. 577–581, 1997.
- [65] L. Pylarinos and K. Phang, “Low-voltage programmable gm-c filter for hearing aids using dynamic gate biasing,” in *Proc. ISCAS’05*, May 2005.